

Water at α -Alumina: Energetics and Kinetics of Adsorbate Systems

Dissertation zur Erlangung des akademischen Grades
›doctor rerum naturalium‹ (Dr. rer. nat.)
in der Wissenschaftsdisziplin Theoretische Chemie

vorgelegt von
Sophia L. Heiden

an der
Mathematisch-Naturwissenschaftlichen Fakultät
der Universität Potsdam



Potsdam, 2018

This work has been done between January 2015 and **TODO: *xx*** 2018 in the workgroup of Prof. Dr. Peter Saalfrank at the Institute of Chemistry at the University of Potsdam.

Potsdam, **TODO: *xx*** 2018

Erstgutachter: Prof. Dr. Peter Saalfrank (Uni Potsdam)

Zweitgutachter: Prof. Dr. Beate Paulus (FU Berlin)

Drittgutachter: Prof. Dr. **TODO: *xy***

Preamble

The importance of surface science in our industrialized world is overwhelming. Most processes in industry are carried out with the help of (heterogeneous) catalysts [1–3] by speeding them up using a different reaction path. The advantage of heterogeneous over homogeneous catalysts is that these do not have to be separated from the reactants and the product after the process, which is often a costly step in the production of chemicals. It is therefore desirable to understand heterogeneous catalytic processes by learning more about the microscopic processes that take place on the surface of materials especially by computational methods. Metal oxide materials are commonly used catalysts as well as catalyst support materials, hence understanding their properties in contact with chemicals, like in this work water, is crucial. This water could be reactant, solute or also impurity in mentioned processes.

Apart from that, aluminum is contained in rocket fuels as a reduction agent so as a result alumina (Al_2O_3) particles are ejected into the atmosphere during the launch [4]. For one space shuttle the start can produce around 276,000 kg of alumina particles [5]. It can be measured that approximately one third of these particles can be deposited in the stratosphere [6] (in an altitude between 15 and 50 km above the surface of the earth). There these particles are accumulated and can react with water and other molecules [7, 8].

Also in geochemical sciences Al_2O_3 is a subject of a variety of studies since aluminum is the most abundant metal in the crust with 8.1% and the third most element therein [9, 10]. It can also be seen as a model systems for more complex aluminosilicates. Oxide rocks are omnipresent in the crust of the earth and henceforth are present in most geochemical processes since the times the earth's atmosphere was oxidizing in the early stages of the planetary evolution [11] which became even extensive with the rise of photosynthetic life forms [12–14] around 2.2 billion years ago [15].

Contents

| | |
|--|-----------|
| Preamble | 3 |
| 1. Theory und Methodology | 7 |
| 1.1. Density Functional Theory | 7 |
| 1.2. Periodic Boundary Conditions | 9 |
| 1.3. Plane Wave Basis, Atom Centered Basis and Peculiarities | 12 |
| 1.4. <i>Ab Initio</i> Molecular Dynamics | 13 |
| 1.5. Frequencies and Intensities | 15 |
| 1.6. Finding Transition States | 17 |
| 1.7. From Density Functionals to Hybrids and Perturbation Theory | 19 |
| 1.7.1. Hybrid Functionals | 19 |
| 1.7.2. Møller Plesset Peturbation Theory | 19 |
| 1.8. Computational Details and Used Programs | 21 |
| 2. Water on $\alpha\text{-Al}_2\text{O}_3(11\bar{2}0)$ | 23 |
| 2.1. Surface Model | 23 |
| 2.2. Structure Search | 26 |
| 2.3. Reactions and Microkinetic Model | 31 |
| 2.4. Vibrational Frequencies | 39 |
| 2.4.1. Normal Mode Analysis | 40 |
| 2.4.2. Born Effective Charges | 49 |
| 2.4.3. Velocity-Velocity Autocorrelation Function | 51 |
| 3. Water on $\alpha\text{-Al}_2\text{O}_3(0001)$ | 55 |
| 3.1. Surface Model and Static Calculations | 55 |
| 3.2. AIMD for MBS Process | 58 |
| 3.2.1. Beam Model | 59 |
| 3.2.2. Example Trajectories | 59 |
| 3.2.3. Microcanonical AIMD at clean surface | 63 |
| 3.2.4. Thermalized Surface | 65 |

Contents

| | |
|--|-----------|
| 3.2.5. Refined Surface Model | 66 |
| 3.2.6. Refined Beam Model | 69 |
| 3.3. Improvement of Reaction Rates | 73 |
| Summary | 83 |
| Appendix | 85 |
| A. Experimental Techniques | 85 |
| A.1. Vibrational Sum Frequency Generation | 85 |
| A.2. Thermal Desorption Spectroscopy | 86 |
| A.3. Molecular Beam Source vs. Pinhole Dosing | 86 |
| A.4. Low-Energy Electron Diffraction | 86 |
| B. Symmetric Slab Frequency | 87 |
| C. Distance Test for Water Molecule | 88 |
| D. Reaction Probabilities | 88 |
| D.1. Microcanonical AIMD at a Clean Surface at $T = 0$ | 89 |
| D.2. Refined Surface Models: Effects of Precoverage | 89 |
| D.3. Refined Beam Models: Clustering and Preexcitation | 91 |
| D.4. $(\text{D}_2\text{O})_2$ Cluster | 91 |
| References | 95 |

1. Theory und Methodology

In this chapter the basics of the applied theoretical methods shall be explained. Starting from the ideas of density functional theory, going over periodic boundary conditions, the specialties when dealing with atom centered bases to *ab initio* molecular dynamics. Proceeding with frequency calculations and intensities over transition state theory to more developed methods like hybrid functionals and perturbation theory. Most parts of this chapter are based on [16].

1.1. Density Functional Theory

For all molecular and periodic systems, theoretical descriptions are based on the calculation of the electronic structure. For this, it is reasonable to separate electronic and nucleic degrees of freedom as introduced by the Born-Oppenheimer approximation [17], which is legit due to the largely different masses of electrons and the nucleus. With this, the electronic Schrödinger equation for the time independent case with the electronic Hamiltonian \hat{H}_e , the electronic total wave function $\Psi_e(\underline{\mathbf{r}})$ and total energy E_e is

$$\hat{H}_e \Psi_e(\underline{\mathbf{r}}) = E_e \Psi_e(\underline{\mathbf{r}}). \quad (1.1)$$

The wave function $\Psi_e(\underline{\mathbf{r}})$ is a function of the coordinate vector $\underline{\mathbf{r}}$ and is $3N_e$ dimensional, with the number of electrons N_e . For larger systems, the solution of Equation (1.1) gets computationally demanding.

An alternative to the wave function based theory is density functional theory (DFT). It is based on the Hohenberg Kohn theorem, that connects the ground state electronic energy E_0 to the electron density $n(\underline{\mathbf{r}})$: There exists a one to one correspondence. If $\Psi(\underline{\mathbf{r}}^N)$ is a N-electron wavefunction, then the electron density can be expressed as

$$n(\underline{\mathbf{r}}) = N_{\text{norm}} \int \dots \int \Psi^*(\underline{\mathbf{r}}, \underline{\mathbf{r}}_2, \underline{\mathbf{r}}_3, \dots, \underline{\mathbf{r}}_N) \Psi(\underline{\mathbf{r}}, \underline{\mathbf{r}}_2, \underline{\mathbf{r}}_3, \dots, \underline{\mathbf{r}}_N) d\underline{\mathbf{r}}_2 \dots d\underline{\mathbf{r}}_N \quad (1.2)$$

with the normalization factor N_{norm} . The second Hohenberg Kohn theorem, also called the variational principle of DFT proves, that a test density $n'(\underline{\mathbf{r}})$ will give a higher or the same

1. Theory und Methodology

energy as the exact density:

$$E_0^{exact} \leq E_0^{HK}[n'(\underline{\mathbf{r}})]. \quad (1.3)$$

In this way, the energy can be determined iteratively with the self consistent field method (SCF) by taking a guess, solving the equation and then improve the guess accordingly.

The total energy $E[n]$ can be determined as:

$$E[n] = T[n] + V_{ext}[n] + V_{ee}[n] = \int n(\underline{\mathbf{r}}) v_{ext}(\underline{\mathbf{r}}) d\underline{\mathbf{r}} + T[n] + E_H[n] + E_{xc}[n] \quad (1.4)$$

with the kinetic energy $T[n]$, the potential energy $V[n]$ for the external potential ext and electron electron interaction ee , the external potential $v_{ext}(\underline{\mathbf{r}})$, the Hartree energy $E_H[n]$, corresponding to the classical Coulomb interaction and the exchange correlation energy $E_{xc}[n]$ for the non-classical exchange correlation interactions. A big advantage over wave function based methods is that only a three dimensional system has to be considered for three spatial coordinates $n(x, y, z)$, instead of $3N_e$ -dimensional system, with N_e being the number of electrons. The size of a system calculated with wave function methods increases exponentially with the number of electrons, while for density calculations, we always have three spatial coordinates, independent from the number of electrons. Problematic in this ansatz is, that the explicit form of the interacting kinetic energy $T[n]$ and the exchange correlation functional¹ $E_{xc}[n]$ are unknown.

Calculating all energy components from the pure density was not very successful, but Kohn and Sham presented their work in 1965 showing that the kinetic energy could be calculated from non-interacting auxiliary particles in a set of orbitals that is used for representing the electron density. A test system with non-interacting electrons that reflects the real systems electron density, is set and calculated. The use of orbitals makes it possible to use the same methods and algorithms previously known from wave function methods. With this the exchange-correlation functional is the only unknown functional, but it is only a small fraction of the total energy. Simple approximations to this functional still give reasonable results, as for example the local density approximation (LDA). Here the homogeneous electron gas is used as a model, assuming that the density would not change strongly if the density does not vary too much in the locality. Furthermore, notable improvement can be made considering the density and its first

¹ To make clear the difference between a function and a functional: in a function (*e.g.* $f(x)$), a number is produced by a set of variables, whereas in a functional ($F[f]$) gives a number from a function which depends on variables.

1.2. Periodic Boundary Conditions

derivative (generalized gradient approximation, GGA):

$$E_{xc} = E_{xc}[n(\underline{\mathbf{r}}), \nabla n(\underline{\mathbf{r}})] \quad (1.5)$$

TODO: *write a little about this? pros and cons of GGA?* and even better by adding second derivatives and mixing in Hartree-Fock exchange (hybrid functionals, like B3LYP and HSE06). A huge problem of DFT is, that it can not be systematically improved like wave function based methods and the weakness of not being able to reproduce important features like van der Waals interactions. To overcome the latter problem it is nowadays possible to add dispersion corrections, that account for van der Waals interactions, and are important, especially for the adsorbate-surface interaction and the adsorbate-adsorbate interaction. They describe pair interactions between atoms A and B in the form:

$$E_{disp}^{(2)} = \sum_A^{N_e} \sum_{B>A}^{N_e} s_6 \frac{C_6^{AB}}{R_{AB}^6} f_{damp}(R_{AB}), \quad (1.6)$$

with the number of atoms N_e , the scaling factor s_6 that is dependent on the functional, the averaged dispersion coefficient C_6 , the interatomic distance R_{AB} and a damping function $f_{damp}(R_{AB})$. This equation gives the D2-corrections $E_{disp}^{(2)}$. For the more advanced D3 method, $E_{disp}^{(2)}$ is altered by subtracting the term $E'_{disp}^{(2)} = E_{disp}^{(2)} - \sum_A^{N_e} \sum_{B>A}^{N_e} s_8 \frac{C_8^{AB}}{R_{AB}^8} f_{damp}(R_{AB})$ and in addition a three body term $E^{(3)}$ is added.

$$E_{disp}^{(3)} = \sum_A^{N_e} \sum_{B>A}^{N_e} \sum_{C>B>A}^{N_e} f_{damp}(\bar{R}_{ABC}) \frac{C_9^{AB} (3\cos\phi_a \cos\phi_b \cos\phi_c)}{(R_{AB} R_{BC} R_{AC})^3}. \quad (1.7)$$

Here, s_8 is a scaling factor, C_8^{AB} and C_9^{AB} are further averaged dispersion coefficients, ϕ_i are the angles of the corresponding triangle that is built by the three atoms A, B and C, and $C_9^{ABC} = \sqrt{C_6^{AB} C_6^{BC} C_6^{AC}}$.

1.2. Periodic Boundary Conditions

Surface systems can be simulated by either calculating clusters that were cut from the surface and represent an "important part" of the system or can be represented as the whole system with a periodic ansatz. These periodic systems can be described by a single unit cell and respective cell vectors, that are used to generate the infinite system by repeating the cell in each direction. This can be either done in 1D (polymers), 2D (surface systems) or 3D (bulk crystals). Also, surfaces can be described within the 3D model as a slab by three dimensional

1. Theory und Methodology

repetition of the unit cell. The only difference is that one has to define a vacuum gap between two slabs (unit or supercell model of a surface) in one direction perpendicular to the surface (*e.g.* here z, c). This gap has to be large enough to prevent unit cells from influencing each other in this direction and therefore lead to unphysical behaviour between the surface atoms and the lowest atoms of the neighboring slab above. Since it is (yet) not possible in VASP to mimic a 2D system, in the main part of this work this vacuum gap 3D model just mentioned was applied. Some programs, however, (here CRYSTAL was used) deliver the opportunity to calculate 2D systems, repeating the slab periodically only in x/y, a/b, respectively.

A disadvantage of this approach is, that a perfect surface is simulated, with absolutely no defect sites. If one was to model a defect, it is repeated periodically and leads to a defined defect site density in a regular pattern. There are embedding models available (*e. g.* [18]) dealing with this issue: the defect is only treated in one unit cell and for the others, the regular unit cell is applied. But before handling defects one has to understand the clean defect free surface properly.

The 3D unit cell can be described by the three basis vectors of the lattice, $\underline{\mathbf{a}}_1$, $\underline{\mathbf{a}}_2$ and $\underline{\mathbf{a}}_3$ and can be translated along these vectors to gain the infinite system. They span the space with defined length and angles. The unit cell with the atoms occupying different positions is called Bravais lattice, where 14 different form exist, *e.g.* hexagonal D_{6h}. The lattice can be described by the lattice vector $\underline{\mathbf{B}}$ with the lattice vectors $\underline{\mathbf{a}}_i$ and the integers n_i :

$$\underline{\mathbf{B}} = n_1 \underline{\mathbf{a}}_1 + n_2 \underline{\mathbf{a}}_2 + n_3 \underline{\mathbf{a}}_3 \quad (1.8)$$

Analogue to that, also a reciproce space exists (the so called $\underline{\mathbf{k}}$ -space) that can be described by the Fourier transform of the direct lattice and is defined analog to Equation (1.8) by the reciprocal lattice vector $\underline{\mathbf{G}}$ and a set of vectors $\underline{\mathbf{b}}_i$ and h, k, l being integers:

$$\underline{\mathbf{G}} = h \underline{\mathbf{b}}_1 + k \underline{\mathbf{b}}_2 + l \underline{\mathbf{b}}_3 \quad (1.9)$$

that span the lattice space. The dimension of the $\underline{\mathbf{b}}_i$ is m⁻¹. For sampling one uses a $\underline{\mathbf{k}}$ -point grid instead of a continuous model, where only important points within the reciproce cell have to be considered which lowers the computational costs drastically. Due to symmetry considerations only a reduced number of $\underline{\mathbf{k}}$ -points have to be evaluated (irreducible $\underline{\mathbf{k}}$ -points). For the reciproce space we have:

$$e^{i\underline{\mathbf{G}} \cdot \underline{\mathbf{B}}} = 1. \quad (1.10)$$

1.2. Periodic Boundary Conditions

Between the vectors of the direct and the reciprocal space there are fixed relations, the vectors $\underline{\mathbf{b}}_i$ can be derived from $\underline{\mathbf{a}}_i$, e.g. by writing

$$\underline{\mathbf{b}}_1 = 2\pi \frac{\underline{\mathbf{a}}_2 \times \underline{\mathbf{a}}_3}{\underline{\mathbf{a}}_1 \cdot (\underline{\mathbf{a}}_2 \times \underline{\mathbf{a}}_3)} \quad (1.11)$$

and so forth, analogously, and they are perpendicular to each other:

$$\underline{\mathbf{a}}_i \cdot \underline{\mathbf{b}}_j = 2\pi\delta_{ij}, \quad (1.12)$$

with δ_{ij} being the Kronecker delta ($\delta_{ij} = 1$ for $i = j$, else = 0).

The unit cell within the reciprocal space, what is called Wigner-Seitz cell in the real space, is also referred to as first Brillouin zone, whose center is the Γ -point ($h = k = l = 0$). It is a uniquely defined primitive cell in reciprocal space that contains all critical points of interest. The integers h , k , and l from Equation (1.9) are also called Miller indices, that can be used to describe the crystallographic planes (position of the surface in the coordinate system). They are determined by finding the point of intersection of the surface plane with the axes of the coordinate system, reduce, then take the reciprocal values and multiply with the least common multiple to gain three integers.

Within the hexagonal (and rhombohedral) lattice system, also the Miller-Bravais notation with four indices $[h, k, i, l]$ can be used. Here, i is redundant and can be defined by h and k : $i = -(h + k)$. For example, the (110) surface would be referred to as (11-(1+1)0)=(11 $\bar{2}0$), since the minus is expressed by the overbar. The advantage of this notation is, that one can identify symmetry-equivalent planes easily. To express a direction vector in the basis of the direct lattice vectors, the notation [uvw] is used. In general this vector is not perpendicular to the plane (uvw), only for cubic lattice this is the case.

To describe a periodic system with quantum mechanical methods, one has to introduce periodic boundary conditions. This includes that the periodicity of the nuclei is reflected by the periodicity of the effective potential v_{eff} , which has to be the same in all cells that are given by $\underline{\mathbf{B}}$:

$$v_{eff}(\underline{\mathbf{r}}) = v_{eff}(\underline{\mathbf{r}} + \underline{\mathbf{B}}). \quad (1.13)$$

According to the Bloch theorem the wave function $\phi(\underline{\mathbf{r}})$ value at equivalent positions in different cells are related to each other with a phase factor containing the reciprocal space vector $\underline{\mathbf{k}}$ and the lattice vector $\underline{\mathbf{B}}$:

$$\phi(\underline{\mathbf{r}} + \underline{\mathbf{B}}) = e^{i\underline{\mathbf{k}} \cdot \underline{\mathbf{B}}} \phi(\underline{\mathbf{r}}) \quad (1.14)$$

1. Theory und Methodology

In this equation the crystalline orbital ϕ for the n^{th} band can be understood as having one wave-like and one cell periodic part φ , also known as Bloch orbital:

$$\phi_{n,k}(\underline{\mathbf{r}}) = e^{i\underline{\mathbf{k}} \cdot \underline{\mathbf{r}}} \varphi_n(\underline{\mathbf{r}}). \quad (1.15)$$

Bloch orbitals can be expanded as a set of plane wave functions (χ^{PW}). Solutions are now dependent on the reciprocal space vector $\underline{\mathbf{k}}$ leading to a Roothaan-Hall expression:

$$\underline{\mathbf{F}}^k \underline{\mathbf{C}}^k = \underline{\mathbf{S}}^k \underline{\mathbf{C}}^k \underline{\varepsilon}^k \quad (1.16)$$

The solutions give a band (range of energies) and are a continuous function. For the total energy per unit cell one has to integrate over the $\underline{\mathbf{k}}$ -space. For non-metallic systems the integration can be done numerically using only a few points [19]. In analogy to molecular HOMO orbital, the energy of the highest filled band is called Fermi energy. The band gap, equivalent to HOMO-LUMO gap, is between the highest filled and the lowest empty band. In metallic systems, there is no bandgap, whereas in insulating systems the band gap is large ($> 4 \text{ eV}$ [20]).

As it was raised before, basis functions within a unit cell can be either delocalized in the form of plane waves or localized as a Gaussian basis set.

1.3. Plane Wave Basis, Atom Centered Basis and Peculiarities

In comparison plane waves (PW) and atom centered orbitals (ACO) have different advantages and disadvantages [21]. For solid state systems both the energy and the gradient converge faster with plane waves. Additionally, the calculation of atomic forces is simpler because only Hellmann-Feynmann forces have to be evaluated. The quality of the basis is simply dependent on the cutoff energy E_{cutoff} , the higher this energy is, the better is the basis. On the negative side, when norm-conserving pseudopotentials are applied more memory is needed. Treating all electrons is computationally expensive, so usually pseudopotentials are used, where core electrons are not treated explicitly but their presence is considered for indirectly. To treat this, the PAW [22,23] (projector augmented-wave method) is applied which gives explicit treatment of the core electrons so that the accuracy is greatly increased. The system is intrinsically defined in 3D, no matter if the system is a 1D (polymer), 2D (surface) or 3D system (bulk). It is computationally demanding to calculate exact (Fock) exchange, which makes the use of hybrid functionals so costly, although the precision of the results is considerably enhanced.

Whenever there are atom centered basis sets the orbitals of different atoms can overlap causing

1.4. *Ab Initio* Molecular Dynamics

electrons being considered multiple times, which stabilizes the system artificially. This subject is called basis set superposition error (BSSE) and only appears if atom centered bases are utilized. One can apply counterpoise corrections (CP) [24] to get rid of this source of error. This is done here by performing ghosted calculations with the system as a whole, the adsorbate alone, and the adsorbate with surface from ghost atoms. Then one applies a subtractive scheme to cancel out the effect of the orbital overlap. On the other hand one can use a huge basis set, that does not have this problem, but comes with a higher computational demand. In contrast to PW calculations the true dimensionality is obeyed due to the locality of the basis. Probably, the most powerful advantage of atom centered bases is that exact exchange and hybrid methods are available as standard methods.

1.4. *Ab Initio* Molecular Dynamics

Apart from solving stationary problems, *ab initio* molecular dynamics (AIMD) can deliver dynamical results for time dependent processes [16,25]. This is necessary for simulating transport/diffusion processes as well as spectral properties. For this, the classical Newton's equation of motion is solved:

$$-\frac{\partial V(\underline{\mathbf{R}})}{\partial \underline{\mathbf{R}}(t)} = M_A \frac{d^2 \underline{\mathbf{R}}_A(t)}{dt^2} \quad (1.17)$$

with the potential energy V that is a function of all nuclear coordinates $\underline{\mathbf{R}}$, the vector $\underline{\mathbf{R}}_A$ that contains all coordinates of atom A , the atomic mass M_A and the time t . This equation gives in principle $F = M_A \cdot a$, the force F acting on each atom in a classical ansatz with the velocity a . This is a good approximation for nuclei are usually sufficiently massive to be treated classically. Strictly speaking, this is not appropriate for hydrogen, since it is so lightweight, that quantum mechanical tunneling processes can not be excluded. For treating quantum effects like zero point energy and tunneling one would have to solve the nuclear Schrödinger equation.

In comparison to classical molecular dynamics, where predefined potentials or force fields based on either empirical data or further electron structure methods are used, *ab initio* MD calculates the potential and the respective (Hellmann-Feynman) forces “on-the-fly” at each time step. This has the advantage, that no further parameterization has to be done when changing atoms or molecular groups/surfaces etc. Also a change in electronic structure along the trajectory can be compensated without the necessity of another potential/force field to describe interatomic interactions, which is especially vital for dissociation processes.

As starting conditions, positions and momenta of the atoms have to be given. Between two time steps of the propagation there is a time span Δt . The time propagation can be done

1. Theory und Methodology

numerically with the Verlet algorithm [26], delivering the trajectory $\underline{\mathbf{R}}(t)$:

$$\underline{\mathbf{R}}_A(t + \Delta t) = \underline{\mathbf{R}}_A(t) + \underline{\mathbf{v}}_A(t) \cdot \Delta t + \frac{1}{2} \underline{\mathbf{a}}_A(t) \cdot \Delta t^2 + \dots \quad (1.18)$$

$$\underline{\mathbf{R}}_A(t - \Delta t) = \underline{\mathbf{R}}_A(t) - \underline{\mathbf{v}}_A(t) \cdot \Delta t + \frac{1}{2} \underline{\mathbf{a}}_A(t) \cdot \Delta t^2 \pm \dots \quad (1.19)$$

the previous and next time steps are approximated by a Taylor expansion with the velocity $\underline{\mathbf{v}}_A(t)$ of atom A (the derivative of the coordinates with respect to time t , $\frac{\partial \underline{\mathbf{R}}_A}{\partial t}$), the acceleration $\underline{\mathbf{a}}_A(t) = \frac{\partial^2 \underline{\mathbf{R}}_A}{\partial t^2}$. With equations (1.18) and (1.19) one can predict the positions at a later time step from the current and the previous positions and the acceleration:

$$\underline{\mathbf{R}}_A(t + \Delta t) = (2\underline{\mathbf{R}}_A(t) - \underline{\mathbf{R}}_A(t - \Delta t)) + \underline{\mathbf{a}}_A(t)(\Delta t)^2 + \dots \quad (1.20)$$

with the acceleration, that must be evaluated at each time step from the potential (gradient of the forces):

$$\underline{\mathbf{a}}_A(t) = -\frac{1}{M_A} \frac{dV}{d\underline{\mathbf{R}}_A}. \quad (1.21)$$

This allows for the time propagation that gives the trajectory.

The time step Δt is an important parameter, it has to be small enough to describe the fastest processes of interest, but not too small to achieve reasonable propagation times with respect to the computation time. Therefore it is typically around 10^{-15}s , for example a molecular vibration of 3000 cm^{-1} corresponds to $\approx 10^{14}\text{s}^{-1}$. On the other hand, a sufficiently long time has to be propagated to measure all chemically relevant processes, usually 10^{-9}s . The smaller the time step the more accurate the simulation gets, but with decreased time steps, one has to propagate longer to gain the same simulation time, which increases the computational time drastically. Additionally, it may be necessary to compute several trajectories instead of just a single one, for reasonable averaging.

The simulations are characterized by the following parameters: the total energy E , the temperature T , volume V , pressure p , the number of particles N and the chemical potential μ . Not all of these are independent, as an example either V or p can be constant. The corresponding ensemble is named after the fixed quantities, *e. g.* NVT (=canonical) and NVE (=micro-canonical).

In a microcanonical ensemble (NVE) the system is isolated (it can not exchange particles or energy with the surroundings) and the total energy E is fixed. Computationally, it can be implemented easily. In experiments usually not the energy but the temperature are controlled. In contrast to that in a canonical ensemble (NVT) the system is coupled / in thermal equilibrium with a heat bath, also referred to as thermostat. T (on average) is given by the temperature of

the thermostat. For this thermostat, several models are available, in this work the Nosé-Hoover thermostat [27–29] is used. The energy accounting of the heat bath is realized by a fictitious particle, that is propagated like real particles of the system and acts like a reservoir of energy for the heat bath. The total energy of the extended system is again a conserved quantity and therefore a control parameter.

1.5. Frequencies and Intensities

A characteristic of stationary points on the potential energy surface (PES) is, that the derivation with respect to all coordinates equals zero. For these points (minima and saddle points of first order) the eigenvalues and -vectors of the Hessian matrix $\underline{\underline{H}}$ are of interest. The elements of this Hessian are the derivation of the potential V with respect to coordinates:

$$H_{ij} = \left(\frac{\partial^2 V}{\partial Q_i \partial Q_j} \right)_{|Q_i=Q_j=0} = \left(\frac{1}{\sqrt{m_i m_j}} \frac{\partial^2 V}{\partial R_i \partial R_j} \right) \quad (1.22)$$

Here, Q_i are mass weighted coordinates $Q_i = \sqrt{m_i} R_i$, with the mass m_i and the displacement from the equilibrium position R_i . With this, the matrix problem for the Hessian $\underline{\underline{H}}$ has to be solved:

$$\underline{\underline{H}} \underline{\mathbf{A}}_i = \lambda_i \underline{\mathbf{A}}_i. \quad (1.23)$$

with the vectors of the normal modes $\underline{\mathbf{A}}_i$ and the eigenvalues λ_i being the squares of vibrational frequencies ω_i :

$$\omega_i = \sqrt{\lambda_i}. \quad (1.24)$$

All frequencies are delivered in the harmonic approximation. It can be distinguished between two physically relevant cases: all eigenvalues are positive ($\lambda_i \geq 0 \forall i$) so the structure is a minimum on the PES. This could be the educt and product of a reaction. The second relevant case is if there is only one negative eigenvalue, that gives according to equation 1.24 one imaginary frequency, respectively. This is in a mathematical sense a saddlepoint of first order and can be interpreted as a transition state. How to find these points is described in Section 1.6.

To calculate intensities of vibrational modes there are several methods available with three being presented in this work:

- I) The IR intensities for each normal mode are estimated from the derivative of the dipole moment with respect to the atomic positions, also known as dynamical dipole moment [30]. The dynamical dipole moment is evaluated by the dipole moment operator

1. Theory und Methodology

$\hat{\mu}$ between two states i and f , where $\hat{\mu}$ is a three component vector. The initial state i is the vibrational ground state and final state f is a vibrationally excited state. The eigenvector of the vibration is used here. It is called dynamical, because it does not describe a static dipole moment but a response of the system. With some symmetry and group theory considerations, one can decide for each vibration, whether it is IR active or not. The respective intensities are determined by $I \propto <i|\hat{\mu}|f>^2$. For this approach, only the dipole components perpendicular to the surface are taken into account. Only these can be measured in respective SFG spectra. These are not completely comparable to IR spectra but IR sensitivity is next to Raman activity one of the selection rules for SFG. Additionally the process is only visible for interfaces. Selection rules for SFG include IR and Raman activity as well as a system without inversion symmetry, which is usually the case for interfaces and surfaces.

- II) Another way to get intensities is by calculating Born effective charges [31], as it was done in the work of Grillo *et al.* [32]. These charges are calculated as the second derivative of the energy with respect to an applied electric field and to the amplitude of a vibrational distortion. This is available through DFPT [33, 34] (density functional perturbation theory), which is a linear response theory. One can calculate the intensity $I(\omega)$ [35, 36]:

$$I(\omega) = \sum_{\alpha=1}^3 \left| \sum_{l=1}^M \sum_{\beta=1}^3 Z_{\alpha\beta}^*(l) e_{\beta}(l) \right|^2. \quad (1.25)$$

Here, α and β are cartesian polarizations, $e_{\beta}(l)$ is the normalized vibrational eigenvector of the ω -th mode, l deciphers the different atoms of the system with the total number M and $Z_{\alpha\beta}^*$ is the Born effective charge tensor of the l -th atom.

From that, with the charges the dipole and also the intensities are available through $\mu = \text{charge} \times \text{distance}$, and again, $I \propto \mu^2$. Both methods are based on normal mode analyses and therefore give IR intensities.

While normal modes are a good approximation for high energy vibrations, for example OD stretch vibrations, it becomes worse for lattice vibrations, which are typically more delocalized.

- III) As a fundamentally different method, power spectra can be calculated from *ab initio* MD trajectories [37]. This is done by analyzing the velocity of the atoms along the trajectories, giving the vibrational spectrum via fast Fourier transformation of the velocity-velocity autocorrelation function:

$$VDOS(\omega) = \sum_{i=1}^N \int_0^{+\infty} < v_i(t) \cdot v_i(0) > e^{i\omega t} dt. \quad (1.26)$$

VDOS is the vibrational density of states as a function of the frequency ω , summing over all N atoms, Fourier transform of the velocity-velocity autocorrelation function $\langle v_i(t) \cdot v_i(0) \rangle$. v_i are the velocities at different times 0 and a later time t . The integration range is from 0 to ∞ (in practice this is just a huge number) due to symmetry considerations. The resulting spectra include implicitly anharmonic and quantum effects: No harmonic approximation for the potential energy surface and the modes are established and movement of the atoms are taken into account. Also, further anharmonic effects like mode coupling, overlapping of neighboring peaks and line broadening are included [38, 39]. The power spectrum contains peaks for each normal mode vector apart from selection rules for vibrational spectroscopy. The obtained intensities correspond to the oscillator amplitudes.

1.6. Finding Transition States

According to the Born-Oppenheimer approximation [17] nuclear and electronic degrees of freedom are separated. In this picture, stable systems are minima on the PES and chemical reactions can be understood as nuclei, moving on the PES along the reaction coordinate ξ . On the N-dimensional surface, the energetically most favorable reaction path is chosen. This is the one with the least energy necessary (minimum energy path, MEP, see Figure 1.1). The transition state (TS) is at the highest energy on this path. As mentioned before, it is a first-order saddle point, the energetically highest point along the reaction coordinate, but in along all other coordinates a minimum.

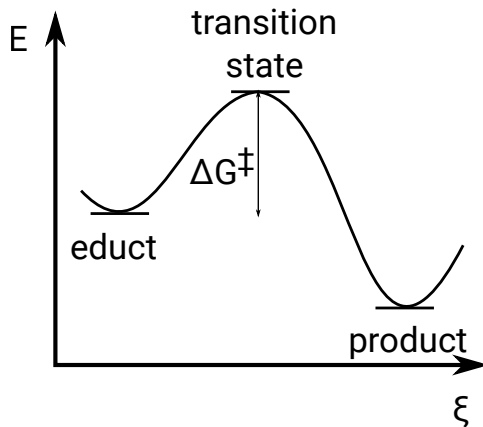


Figure 1.1.: Schematic view of a minimum energy path (MEP) for a thermal reaction. The free energy $\Delta G^\ddagger = \Delta G_{\text{TS}} - \Delta G_{\text{educt}}$ for the reaction is also plotted.

Transition state theory is a semi-classical theory: dynamics along the reaction coordinate ξ are

1. Theory und Methodology

treated classically, but perpendicular directions allow for quantization of vibrational and rotational energy. In thermodynamical equilibrium, all possible quantum states along the reaction coordinate are occupied with respect to their Boltzmann weight $e^{\Delta E/(k_B T)}$.

Assuming the reaction



where reactants A and B are in thermodynamical equilibrium with the transition state C^\ddagger and from this the reaction goes to the product D . The rate constant can be determined with Eyring theory:

$$k(T) = \kappa \frac{k_B T}{h} e^{\Delta G^\ddagger(T)/(k_B T)} \quad (1.28)$$

with the reaction rate constant $k(T)$, which is in fact not a constant but a function of temperature T , the transmission coefficient κ that will be explained shortly, Boltzmann's constant k_B , the difference of Gibb's free energy for the transition state and the educt $\Delta G^\ddagger = \Delta G_{\text{TS}} - \Delta G_{\text{educt}}$, give the reaction rate constant as a function of temperature and free energy barrier height. Note, that this equation is only valid for cases, where all reactants that reach the TS react to the product site, *i.e.* no re-crossing is employed, so the rate is in the classical picture the upper limit. For quantum effects, the rate can be increased due to tunneling, where reactants can overcome the barrier although they do not possess the sufficient amount of energy for the barrier. For this, the Eyring equation can be expanded with the transmission coefficient κ , that can be interpreted as a tunneling prefactor, for $\kappa > 1$ tunneling occurs and for $\kappa < 1$ non-classical reflection or re-crossing to the educt side.

For the barrier height one needs to find the free energies of the transition state and the educt. The educt geometry can simply be obtained by geometry optimization as a minimum on the PES. To find the transition state geometry and henceforth the energy we used Nudged Elastic Band calculations (NEB), with Climbing Image. The Reaction path is approximated as a series of associated images, which are connected via spring forces. These spring forces prevent the images from optimizing into the local minimum next to the transition state. First a regular NEB, then on top of this climbing image was done which gives better convergence. In this calculation the energetically highest image is "optimized" towards higher energies in the contrary direction of the gradient. For the point found by this scheme it must be checked whether this is a transition state via frequency analysis, since a TST of first order has to have one imaginary mode, that vibrates along the reaction path.

1.7. From Density Functionals to Hybrids and Perturbation Theory

1.7.1. Hybrid Functionals

In this work we also want to go beyond GGA (Generalized Gradient Approximation, here the PBE functional), because it is known from literature to underestimate reaction rates [40]. Since we are interested in reaction kinetics it therefore is desirable to use more sophisticated methods to improve the rates. The first approach applied here is using hybrid functionals, where a fraction of exact exchange is mixed into the potential. For this the exchange correlation functional is split up into two parts:

$$E_{xc}[n(\underline{\mathbf{r}})] = E_x[n(\underline{\mathbf{r}})] + E_c[n(\underline{\mathbf{r}})]. \quad (1.29)$$

The exchange part can be specified with a DFT part and HF with exact exchange:

$$E_x = aE_x^{HF} + (1 - a)E_x^{DFT}. \quad (1.30)$$

with the parameter a , that gives the amount of exact Hartree-Fock exchange. As an example, the functional B3LYP consists of 20% exact exchange [41].

$$E_{xc}^{B3LYP} = aE_{xc}^{LDA} + (1 - a)E_x^{HF} + bE_x^{B88} + cE_c^{LYP} + (1 - c)E_c^{LDA} \quad (1.31)$$

with $a = 0.80$, $b = 0.72$ and $c = 0.81$.

1.7.2. Møller Plesset Peturbation Theory

TODO: *difference of MP2 to local MP2?*

Another ansatz is using Local Møller Plesset Perturbation Theory [42–44] of 2nd order (LMP2) as implemented in crystal/crysccor [45, 46]. These calculations are way more computationally demanding but offer better results on a higher level of theory. It offers more precise treatment of the dynamical electron correlation than DFT. The electronical Hamiltonian (in the following section the subscript e is omitted) has already been solved exactly or approximately. The solution to the given problem is similar to the already known one. The reference system \hat{H}_0 is perturbed by an external potential \hat{V} :

$$\hat{H} = \hat{H}_0 + \lambda\hat{V}. \quad (1.32)$$

1. Theory und Methodology

\hat{H}_0 is the unperturbed Hamiltonian and λ a parameter, that determines the extent of the perturbation, but in general it is considered as “small”, compared to \hat{H}_0 . The perturbed Schrödinger equation is given by:

$$\hat{H}\Psi = E\Psi. \quad (1.33)$$

If $\lambda = 0$, then $E = E^{(0)}$, $\hat{H} = \hat{H}_0$ and $\Psi = \Psi^{(0)}$. For higher values of λ , the energy and the wave function change and can be written by expanding the ground state wave function Ψ_0 at $\lambda = 0$

$$\Psi_0 = \Psi_0^{(0)} + \lambda\Psi_0^{(1)} + \lambda^2\Psi_0^{(2)} + \dots, \quad (1.34)$$

the eigenvalues E_0 can be determined analogously as:

$$E_0 = E_0^{(0)} + \lambda E_0^{(1)} + \lambda^2 E_0^{(2)} + \dots \quad (1.35)$$

The superscript $E_0^{(n)}$ equals the correction of n-th level.

The unperturbed energy can be calculated with:

$$E^{(0)} = <\Psi^{(0)}|\hat{H}^{(0)}|\Psi^{(0)}> = \sum_{i=1}^N \varepsilon_i \quad (1.36)$$

and the energy of 1st order is:

$$E^{(1)} = <\Psi^{(0)}|\hat{V}|\Psi^{(0)}>. \quad (1.37)$$

$E^{(0)} + E^{(1)}$ equals the Hartree-Fock energy E_{HF} . For the energy of the second order, both occupied orbitals i, j and unoccupied orbitals k, l and their energy have to be considered:

$$E^{(2)} = \sum_i^{\text{occ.}} \sum_{j>i}^{\text{occ.}} \sum_k^{\text{unocc.}} \sum_{l>k}^{\text{unocc.}} \frac{(\langle ij|kl \rangle - \langle ij|lk \rangle)^2}{\varepsilon_i + \varepsilon_j - \varepsilon_k - \varepsilon_l} \quad (1.38)$$

The MP2-corrected total energy is composed of the HF energy and the second order energy:

$$E_{MP2} = E^{(0)} + E^{(1)} + E^{(2)} = E_{HF} + E^{(2)}. \quad (1.39)$$

The second order energy accounts for approximately 80 – 90% of correlation which makes it a highly feasible method that includes electron correlation. However, a main limitation of MP2 is if the wave function of the zeroth order is a good approximation to the real system and the perturbation is rather small. If the wave function describes the system poorly, the corrections have to be higher and eventually, convergence is slow. In this case perturbation theory might not be a good option to describe correlation.

1.8. Computational Details and Used Programs

The main part of this work has been done with the Vienna *ab initio* simulation package (VASP version 4 and 5.2) [47–51]

For all the VASP calculations for the (0001) surface the parameters from prior work in the Saalfrank workgroup was used, because these were converged carefully by Dr. Jonas Wirth [52–55]. Total energy convergence was achieved when energies between two SCF steps were smaller than 10^{-5} eV and structures were assumed minima if the change in forces between two structures was below 0.01 eV/Å. The energy cutoff was set to 400 eV. A vacuum gap of 26.4 Å was used. These parameters were adopted for the (11̄20) surface. Here, the vacuum gap ranged from 17 to 11 Å, depending on the slab size in c-direction.

The atom centered basis calculations with the programs crystal [45] (version 14) and the MP2 calculations with cryscor [46] were not used before for the calculation of alumina in our group before. The geometries from the VASP output were used as starting points and the usual convergence criteria of the programs were applied (with some exception when convergence was hard to achieve).

2. Water on $\alpha\text{-Al}_2\text{O}_3(11\bar{2}0)$

2.1. Surface Model

The structure of α -alumina has been well known for decades and was studied extensively (*e.g.* [56, 57]). It crystallizes in the hexagonal cell, that means $a = b \neq c$, with an angle of 60° between the cell vectors a and b .

To obtain the clean surface slab model of the $(11\bar{2}0)$ surface a 2×2 supercell was cut from the bulk. The corresponding cell vectors were adopted from the bulk structure and a vacuum gap in z direction (perpendicular to the surface) was introduced to avoid unphysical interaction between the slabs in z direction. In Figure 2.1(a) the $(11\bar{2}0)$ surface and the (0001) surface that is also studied later in this work can be seen. Figure 2.1(b) shows the top view and the cell

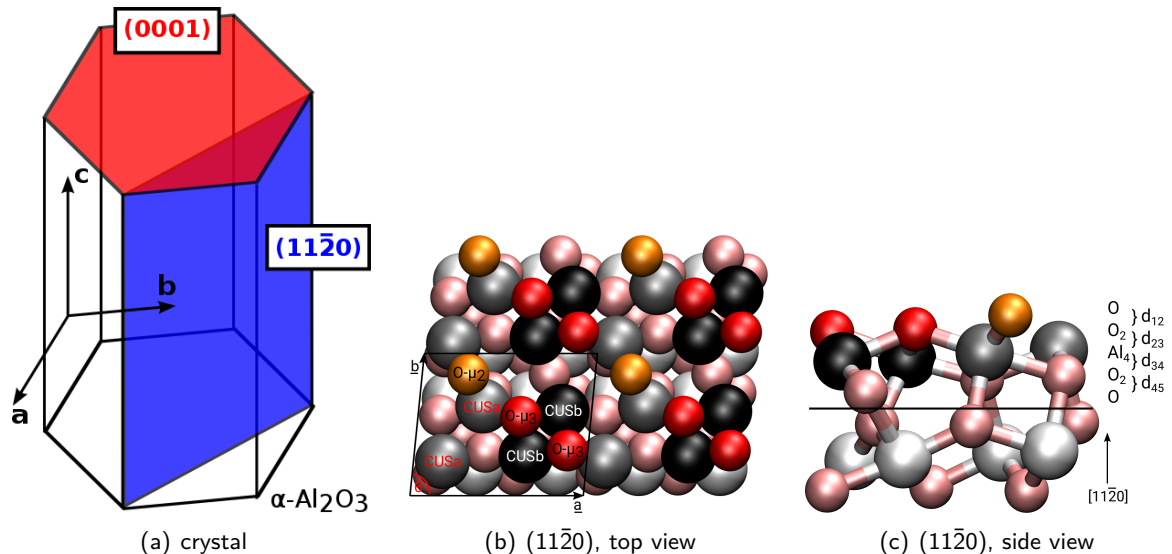


Figure 2.1.: The crystal cut of $\alpha\text{-Al}_2\text{O}_3$, (a) schematic view compared to the (0001) surface, (b) a top view of the geometry optimized 2×2 supercell with the nomenclature of the surface atoms. The two types of surface Al atoms (grey CUSa and black CUSb) as well as the twofold and threefold coordinated oxygen atoms (orange O- μ_2 and red O- μ_3). Subsurface atoms are indicated by pale colors. (c) gives the side view of the unit cell showing the distinctive atomic layers, again with the same color code as in (b).

2. Water on $\alpha\text{-Al}_2\text{O}_3(11\bar{2}0)$

vectors \underline{a} and \underline{b} of $(11\bar{2}0)$. They are not equal to those in the hexagonal cell for this particular surface cut, with $\underline{a} = 10.36\text{\AA}$, $\underline{b} = 14.16\text{\AA}$ and $\underline{c} = 20.5\text{\AA}$. The angle θ between \underline{a} and \underline{b} is 84.56° unlike the 60° since the $(11\bar{2}0)$ surface is tilted with respect to the top crystal plane. The nomenclature and color code of the surface Al and O atoms is also shown: The Alumina atoms have the same number of oxygen neighbor atoms but differ slightly in the arrangement of their neighbors and the distance in the relaxed structure, whereas the oxygen atoms in fact differ by the number of neighbors. In this work, the grey spheres denote the CUSa atoms, the black ones depict the CUSb. The twofold coordinated oxygen atoms ($\text{O}-\mu_2$) are shown in orange and the threefold coordinated ($\text{O}-\mu_3$) in red. Atoms of the underlying layers are illustrated in pale colors, light grey for alumina and pale red for oxygen.

The unit cell consists of five atomic layers in z direction ($\text{O}-\text{O}_2-\text{Al}_4-\text{O}_2-\text{O}$), see Figure 2.1(c)). The spacing between these layers in the relaxed structure and in the bulk crystal is slightly changed as given in Table 2.1. The uppermost layer distance increases while the deeper ones decrease their values. A major issue of the optimization apart from layer spacing is that

Table 2.1.: Distances between the top five layers (see also numbering in Figure 2.1(c)) for different optimized slab sizes and the unrelaxed bulk structure (right column). All values are given in \AA .

| distance | atomic layers | | | | bulk |
|----------|---------------|-------|-------|-------|-------|
| | 10 | 15 | 20 | 25 | |
| d_{12} | 0.232 | 0.234 | 0.247 | 0.245 | 0.193 |
| d_{23} | 0.642 | 0.649 | 0.638 | 0.639 | 0.741 |
| d_{34} | 0.656 | 0.655 | 0.671 | 0.672 | 0.741 |
| d_{45} | 0.198 | 0.205 | 0.209 | 0.213 | 0.191 |

the interatomic distances of surface Al species change: the CUSa–CUSa distance increased from 2.682 to 2.994\AA , the CUSa–CUSb distance increased from 2.833 to 2.876\AA whereas the CUSb–CUSb distance decreased from 2.682 to 2.499\AA .

The supercell model that is mostly used in this work has ten atomic layers, with the lowest five fixed to the bulk value to mimic the surface situation. For the calculations of the lattice vibrations up to 25 layers were considered (Figure 2.2). For each slab size the respective lowest five layers were kept fixed, see chapter 2.4.1. The spacing between the five top layers for each slab size is also displayed in Table 2.1.

\mathbf{k} -point tests were done for five different grid sizes from $1 \times 1 \times 1$ to $5 \times 5 \times 1$. In contrast to the even grid sizes, the odd ones contain the Γ -point and therefore are favorable. It can be deduced from Figure 2.3 that the $3 \times 3 \times 1$ grid is already converged with respect to the energy of the clean surface.

2.1. Surface Model

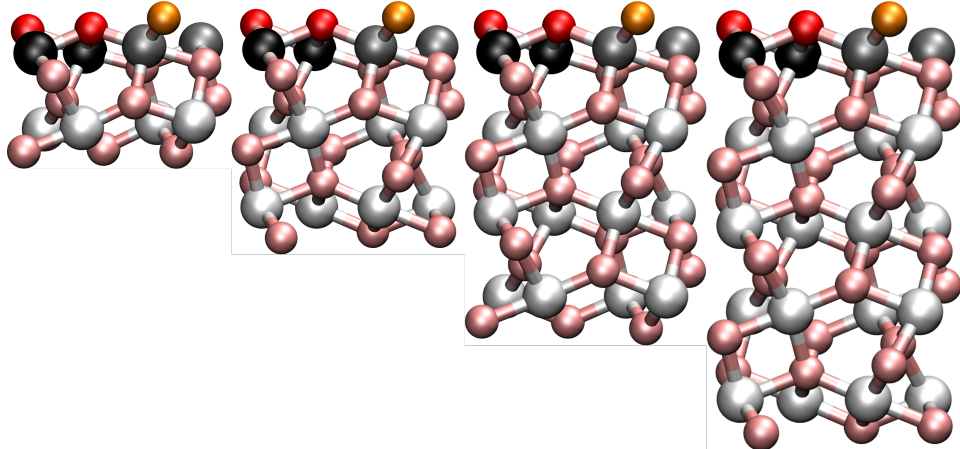


Figure 2.2.: Side view for the different cell sizes for 10, 15, 20 and 25 layers in z direction. Surface atoms are shown in the color code clarified before.

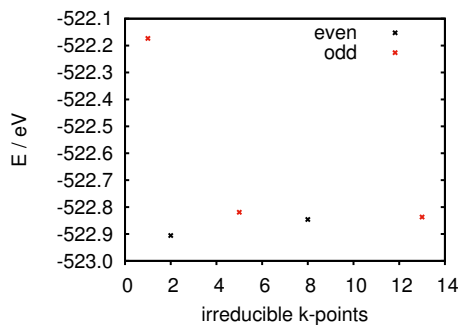


Figure 2.3.: Sampling of the \mathbf{k} -points, shown is the energy of the optimized supercell with respect to the number of irreducible \mathbf{k} -points. The even values correspond to the $2 \times 2 \times 1$ (2 irreducibles) and $4 \times 4 \times 1$ (8 irr.), whereas the odd, which contain the Γ -point, are described by $1 \times 1 \times 1$ (1 irr.), $3 \times 3 \times 1$ (5 irr.) and $5 \times 5 \times 1$ (13 irr.).

Starting from the 2×2 supercell approach of the clean surface there are 16 CUS Al-atoms (coordinatively unsaturated site). These have fewer bonds than the aluminum atoms in the bulk structure since the surface layer is depleted. These atoms are very interesting for adsorbate molecules/atoms, because these surface atoms are electron rich and can be addressed for adsorption. Theoretically, these 16 atoms could be covered with water to gain 1 mono layer (ML). Of these 16 CUS atoms eight are CUSA and eight CUSB. On top of CUSB, a water molecule/OH residue can adsorb, but on top of a CUSA the adsorbate roams to a bridging inter-CUSA position between two CUSA. Due to this the number of potential adsorbates is decreased to twelve forming 1ML.

2. Water on $\alpha\text{-Al}_2\text{O}_3(11\bar{2}0)$

2.2. Structure Search

To study water adsorption, first a low coverage regime was investigated: One water molecule per 2×2 supercell, which equals a coverage of 1/12. The procedure was the following: put molecular water at different positions on the surface and let it relax. By doing this one molecular minimum and several dissociated species including both CUS and oxygen types were found. This multitude of different surface atoms gives rise to a large variety of possible adsorption geometries for the next neighboring situation that even can be expanded when considering adsorbate structures with greater distance between the residues. Adsorption energies and Gibb's free energy of the resulting next neighbor species can be seen in Table 2.2. The nomenclature for the adsorption sites that is used in the following gives at first the type of Al site where the OH-residue ($/\text{OH}^-$) is adsorbed and at second place the oxygen type where the H($/\text{H}^+$) is adsorbed ($\text{OH-site}||\text{H-site}$). The term "inter" that is used in the following characterizes a position between two CUS atoms and leads to a bidentate adsorption pattern. The additional notation with ' denotes greater distances between the residues. There is also one metastable molecular species that appears to be more stable than the found molecular minimum considering adsorption energy, but it cannot be classified as a stable minimum since there is one imaginary mode displaying the movement of the proton towards the dissociated species. The adsorption energy is defined by Equation 2.1 as the energy of the adsorbed system compared to the energies of the clean surface and the isolated water molecule:

$$E_{\text{ads}} = E_{\text{ads. species}} - (E_{\text{free water molecule}} + E_{\text{surface}}). \quad (2.1)$$

Table 2.2.: For molecular and (singly) dissociated water on $\alpha\text{-Al}_2\text{O}_3(11\bar{2}0)$ adsorption energies E_{ads} and Gibb's free energy G_{ads} for different temperatures are given in eV. E_{ads} was calculated from Equation 2.1 and G_{ads} is defined analogously. These results were obtained with PBE+D2. The three most stable configurations are marked with bold letters.

| Adsorbed Species | | E_{ads} | $G_{\text{ads}, 130 \text{ K}}$ | $G_{\text{ads}, 300 \text{ K}}$ | $G_{\text{ads}, 400 \text{ K}}$ |
|------------------|---|------------------|---------------------------------|---------------------------------|---------------------------------|
| molecular | CUSb | -1.78 | -1.60 | -1.51 | -1.46 |
| | inter-CUSA O-μ_2 | -2.50 | -2.27 | -2.16 | -2.09 |
| | inter-CUSA O- μ_3 | -1.67 | -1.44 | -1.33 | -1.27 |
| | CUSb O-μ_2 | -2.28 | -2.12 | -2.03 | -1.97 |
| | CUSb O- μ_3 | -1.19 | -1.05 | -0.98 | -0.95 |
| | inter-CUSb O-μ_2 | -2.09 | -1.88 | -1.80 | -1.76 |
| | inter-CUSb O- μ_3 | -1.89 | -1.71 | -1.63 | -1.58 |

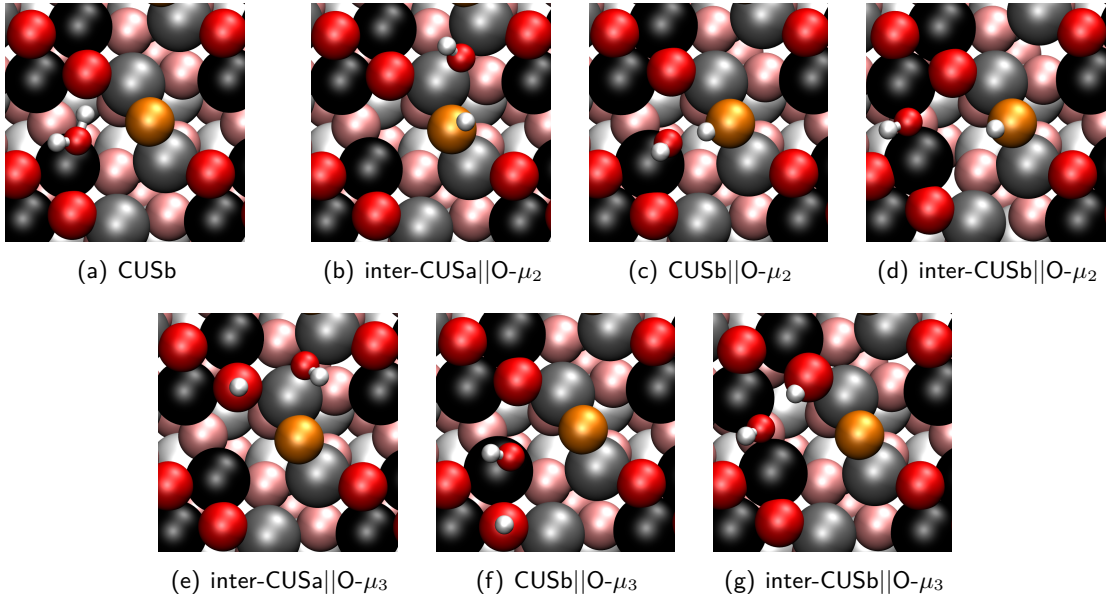


Figure 2.4.: Top view of the adsorption geometries for molecular CUSb (a) and the next neighbor dissociated water ((b)-(g)). The color code is the same as in Figure 2.1(b) and (c), CU₃ grey, CU₂ black, O- μ_2 orange and O- μ_3 red; Hydrogen is illustrated in white; the oxygen from water is in red but as a smaller sphere to make it distinguishable from the surface O atoms; subsurface layers are shown in pale colors.

The molecular minimum is substantially less stable than most of the dissociated species. On the contrary, the dissociated water where the twofold coordinated surface oxygen atom is addressed is very stable, even in comparison to the more stable surface cuts (0001) and (1̄102) that were investigated in our group by Dr. Jonas Wirth [52,55] previously. Dissociated species, where the proton is located at a twofold coordinated surface oxygen are far more stable than the corresponding systems where the threefold coordinated oxygen is occupied. This is due to the higher negative charge and the higher basicity of such a twofold coordinated oxygen atom in comparison with the more saturated threefold coordinated O- μ_3 oxygen atom. In fact, the adsorption can be seen as a Lewis acid / base reaction [58] with the Lewis acid character of the undercoordinated aluminum and the base character of the oxygen from the water molecule. The adsorption of OH at an inter-CUSa site is more favorable than at a CUSb site, because the former corresponds to a site where in the bulk system another oxygen atom would be situated, which is not the case for the CUSb position. Additionally, the CUSb position is electronically and sterically more hindered because of the two threefold coordinated oxygen atoms in the surroundings.

Dissociated species in direct neighborhood as shown in Table 2.2 and Figure 2.4 are more stable

2. Water on $\alpha\text{-Al}_2\text{O}_3(11\bar{2}0)$

than those where the proton and the OH residue are further apart (see Table 2.3), given the OH residue has a stabilizing effect on the H and vice versa. It is apparent from this table that the inter-CUSb||O- μ_3''' -species is more stable than the species inter-CUSb||O- μ_3'' . This is due to the fact that the periodic conditions actually lead to a decrease of the distance between OH groups in the former system. The distances between the neighboring OH groups in the O- μ_3'' system are 6.19 and 8.82 Å, compared to 6.64 and 8.96 Å in the O- μ_3''' system (the numbers refer to the two possible distance in the periodic system, direct and over the border of the unit cell). The latter one is in fact only slightly further away, the average distance is 0.739 Å for inter-CUSb||O- μ_3'' and 0.780 Å for inter-CUSb||O- μ_3''' . Although the distance is larger, there seems to be more stabilization by the surrounding surface atoms. For examples of the corresponding diffusion reactions, see chapter 2.3.

Table 2.3.: Comparison of adsorption energies for next neighbor dissociated species and dissociated species where OH and H are further apart. Results for the adsorption energy E_{ads} are given in eV.

| Adsorbed Species | E_{ads} |
|---------------------------|------------------|
| inter-CUSA O- μ_3 | -1.67 |
| inter-CUSA O- μ_3' | -1.42 |
| inter-CUSb O- μ_3 | -1.89 |
| inter-CUSb O- μ_3'' | -1.16 |
| inter-CUSb O- μ_3''' | -1.22 |

Apart from that, systems with additional atomic layers were studied to gain knowledge towards more extended systems. The corresponding adsorption energies are shown in Table 2.4. Basically, the findings do not differ largely with increasing slab size. The molecular species still is less stable than the O- μ_2 dissociated species and is more stable than the O- μ_3 dissociated ones (except for inter-CUSb||O- μ_3 dissociated system). inter-CUSA||O- μ_2 is the most stable structure through all sampled systems sizes, inter-CUSb||O- μ_2 and CUSb||O- μ_2 change their stability (it approaches to nearly the same value for 25 layers) depending on the number of layers but still are some orders of magnitude less probable than inter-CUSA||O- μ_2 . Dissociated systems occupying the threefold coordinated surface oxygen atom remain in the same stability order. Table 2.4 shows that the most stable systems are already converged for the 10 layer slab with regard to adsorption energies (and also vibrational OD stretch frequencies as will be seen in section 2.4.1).

Furthermore, systems with a higher water coverage were considered to model enhanced systems, some exemplary cases for two water molecules (16.6% coverage), four inter-CUSA||O- μ_2

2.2. Structure Search

Table 2.4.: Adsorption energies calculated from Equation 2.1 for molecular and dissociated species for different vertical slab sizes. All values are given in eV. The most stable systems (inter-CUSa||O- μ_2 , CUSb||O- μ_2 and inter-CUSb||O- μ_2 are highlighted in bold letters.

| System | 10 layers | 15 layers | 20 layers | 25 layers |
|---|--------------|--------------|--------------|--------------|
| CUSb | -1.78 | -1.80 | -1.81 | -1.83 |
| inter-CUSa O-μ_2 | -2.50 | -2.46 | -2.54 | -2.56 |
| inter-CUSa O- μ_3 | -1.67 | -1.67 | -1.78 | -1.80 |
| CUSb O-μ_2 | -2.28 | -2.35 | -2.36 | -2.35 |
| CUSb O- μ_3 | -1.19 | -1.71 | - | - |
| inter-CUSb O-μ_2 | -2.09 | -2.43 | -2.48 | -2.36 |
| inter-CUSb O- μ_3 | -1.89 | -1.59 | -1.65 | -2.09 |

(33.3% coverage) and a fully covered supercell (twelve molecules, 100% coverage), for these systems normal mode analyses were carried out to get vibrational spectra, see Section 2.4.1. Structures can be found in Figures 2.5 and 2.6.

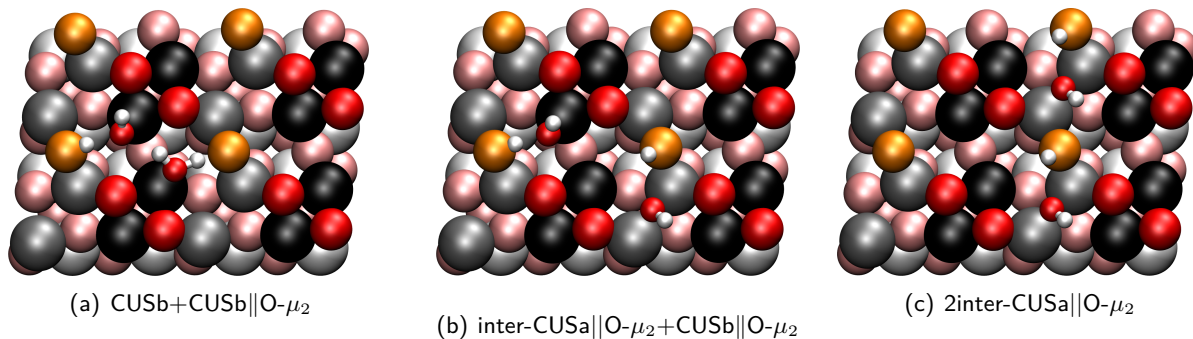


Figure 2.5.: PBE+D2 optimized geometries of systems with two water adsorbates: (a) molecular CUSb and CUSb||O- μ_2 , (b) the two most stable configurations inter-CUSa||O- μ_2 and CUSb||O- μ_2 and (c) 2 inter-CUSa||O- μ_2 , which is the most stable adsorption pattern.

The stability of those species with n adsorbed water molecules is defined as

$$E_{\text{ads}} = E_{\text{ads. species}} - (n \times E_{\text{free water molecule}} + E_{\text{surface}}). \quad (2.2)$$

In Table 2.5, the adsorption energies for the high coverage species mentioned above are given. There are also the results for the higher coverages in comparison to results in the low coverage limit by adding them up (see also column 3 in Table 2.5). The structures where chosen such that the neighborhood effect shows three different outcomes: it can have a stabilizing effect, where the dissociated water stabilizes the molecularly adsorbed water in CUSb(mol)+CUSb||O- μ_2

2. Water on $\alpha\text{-Al}_2\text{O}_3(11\bar{2}0)$

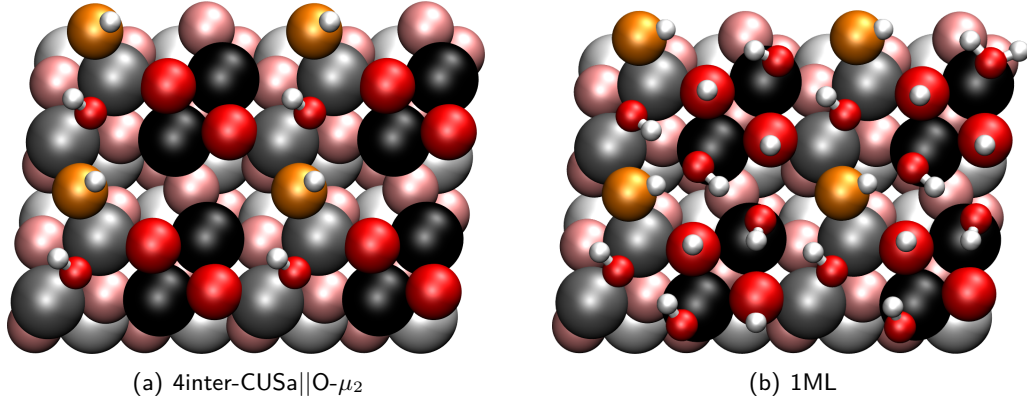


Figure 2.6.: Optimized structures of the (a) 4inter-CUSA||O- μ_2 and (b) fully covered (1ML) system. The latter one shows one molecular species and several hydrogen bonded OH groups.

Table 2.5.: Adsorption energies for higher water coverages in eV. For better comparison in the third column labeled “isolated species” the summed energies for singly adsorbed water as given in Table 2.2 are presented.

| Adsorbed Species | E_{ads} | isolated species |
|--|------------------|------------------|
| CUSb(mol)+CUSb O- μ_2 | -4.57 | -4.06 |
| inter-CUSA O- μ_2 +CUSb O- μ_2 | -4.77 | -4.78 |
| 2inter-CUSA O- μ_2 | -4.84 | -5.0 |
| 4inter-CUSA O- μ_2 | -9.55 | -10.0 |
| 12H ₂ O | -23.39 | ^a |

^a One can not distinguish exactly, but there are 4 inter-CUSA-OD groups, 8 CUSb-OD groups, 8 O- μ_3 and 4 O- μ_2 OD groups, hence one can not calculate a sum of the isolated species.

(Figure 2.5(a)). It can also have the contrary effect, as can be seen in the 2inter-CUSA||O- μ_2 , which becomes less stable (Figure 2.5(c)). On the other hand, there is the inter-CUSA||O- μ_2 +CUSb||O- μ_2 which is merely affected by the neighboring OD residues (Figure 2.5(b)).

As a short excursus, also a “defect site”, the O-II terminated surface, as it is called in the nomenclature of Kurita [59], was calculated. This is the second most stable surface termination under most chemical potential conditions, mostly in Al-rich environment. In this termination, the topmost oxygen layer of the O-I termination is missing. As for the O-I termination, 10 layers were considered and from these the lowest five layers were kept fixed to bulk values. Both the clean surface and the fully covered (1 ML) surface were optimized (see Figure 2.7) and frequency calculations were conducted, to obtain vibrational modes. The structure of the clean surface, of course, differs by the “missing” oxygen O- μ_2 atoms in the topmost layer, and

2.3. Reactions and Microkinetic Model

the fully covered system is even more different: of twelve water molecules that can adsorb, seven adsorb molecularly and five dissociatively. In comparison, the fully covered system for the O-I termination only shows one molecularly adsorbed molecule (*cf.* Figure 2.6(b)).

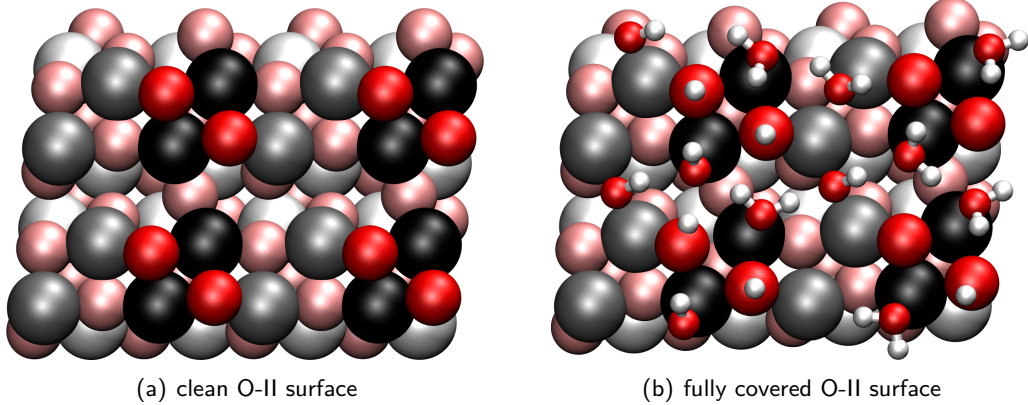


Figure 2.7.: O-II terminated surface, as an example of a defect site optimized with PBE+D2. The top layer oxygen atom from the O-I terminated surface is missing and gives rise to a different chemical behaviour. (a) clean surface, (b) 1ML water adsorbed surface.

2.3. Reactions and Microkinetic Model

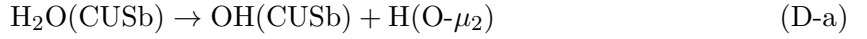
Based on the minimum structures one has to identify reaction pathways to fully understand the reactivity of a system. We utilize the NEB method including climbing image to search for transition states between the minima of the 10 layer slab. We examined three different types of reactions: dissociation from the molecular minimum, as well as OH- and H-diffusion. These reaction paths and corresponding rates were calculated for hydrogen instead of deuterium that was used for vibrational frequencies. The dissociation reactions are named D, diffusion reaction Df-OH and Df-H, respectively, in Table 2.6 and Figures 2.8 and 2.9. In addition, molecular water diffusion on the surface is supposable but due to the low stability, it will dissociate before diffusion can occur. In the publication that emerged from this work (Reference [60]) most of the reactions were introduced, additional reactions paths are supplied here.

We investigated five distinct dissociation reactions: the reactions from CUSb to the twofold coordinated oxygen (D-a) and one to the threefold coordinated O- μ_3 (D-b). One additional dissociation starts from the metastable inter-CUSA molecular structure that is, as was said before, no minimum structure and goes to the most stable species inter-CUSA||O- μ_2 (D-c). Two further dissociation reactions were converged but showed a two step process and are therefore not interesting in the first place (these reactions are CUSb \rightarrow inter-CUSA||O- μ_2 and

2. Water on $\alpha\text{-Al}_2\text{O}_3(11\bar{2}0)$

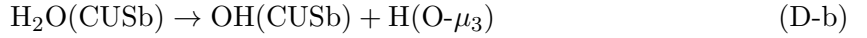
$\text{CUSb} \rightarrow \text{inter-CUSb}\|\text{O}-\mu_2$ and both went via the dissociated $\text{CUSb}\|\text{O}-\mu_2$ intermediate).

As can be seen from Section 2.2 (Table 2.2), the molecular minimum CUSb is low in stability compared to the $\text{O}-\mu_2$ dissociated minima. The reaction D-a leads from the molecular minimum at CUSb to the twofold coordinated $\text{CUSb}\|\text{O}-\mu_2$:

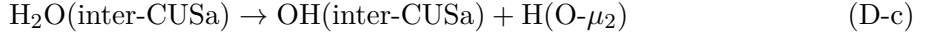


The barrier is very low, about 0.002 eV as one can see from Table 2.6 and Figure 2.8(a), hence the reaction rate constant is very high, in the range of $k_{300\text{K}} = 5.76 \times 10^{12} \text{ s}^{-1}$. This low barrier might be due to underestimation of barrier heights [40] with the used functional PBE (compare section 1.7).

For the other dissociation reaction D-b from CUSb to $\text{CUSb}\|\text{O}-\mu_3$, there is no barrier found at all, the reaction pathway shows simply an upgoing path in energy without any barrier (see Figure 2.8(b)), since the molecular minimum is by 0.15 eV more stable than the dissociated structure on $\text{CUSb}\|\text{O}-\mu_3$. Thus, no reaction rate constant can be calculated.



A further dissociation D-c from the metastable inter-CUSA species also shows no barrier (without Figure), assumingly because the educt is no stable minimum and because the product is much more stable:



On the other hand reaction D-b does also not possess a barrier, so it remains unclear whether it is due to methodology and the barrier is too low to be detected with the settings applied for the calculations or for chemical reasons.

Apart from dissociation that is highly favored on this surface cut compared to more stable alumina surfaces [60], diffusion reactions starting from the dissociated species are important for understanding further processes. The OD diffusion reaction Df-OH-a moves from $\text{CUSb}\|\text{O}-\mu_2$ to the inter-CUSb position, which is relatively fast for OD diffusion reactions compared to the reactions at other alumina surfaces [52, 55].



In this special reaction, the OH residue diffuses from an on top CUSb position into a gap between two CUSb atoms (inter-CUSb position), so that there is not much repulsion with

2.3. Reactions and Microkinetic Model

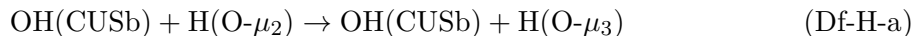
neighboring surface oxygen atoms and other CUS atoms nearby during the diffusion, see Figure 2.8(c). Also the distance that has to be overcome is very small. The barrier height equals 0.35 eV and the corresponding rate constant $k_{300K} = 1.88 \times 10^6 \text{ s}^{-1}$.

In contrast to that the real CUS-to-CUS diffusion reaction Df-OH-b is much slower. It is a diffusion from CUSb to inter-CUSA with the hydrogen residue staying at an O- μ_2 position (see Figure 2.8(d)). This barrier is with 1.07 eV relatively high and leads to $k_{300K} = 2.41 \times 10^{-6} \text{ s}^{-1}$.



This is still faster than OH diffusion reaction for the (0001) alumina surface [52, 61], where the rate constant of a comparable CUS-to-CUS diffusion reaction is $k_{300K} = 4 \times 10^{-45} \text{ s}^{-1}$. For the (1\bar{1}02) surface no OH diffusion was calculated, but the corresponding H₂O diffusion process is around $k_{300K} = 1.4 \times 10^{-3} \text{ s}^{-1}$, whereas the H₂O diffusion process for the (0001) surface is in the range of $k_{300K} = 8 \times 10^{-3} \text{ s}^{-1}$, too. For the (11\bar{2}0) surface no H₂O diffusion reactions can be observed due to the instability of the molecularly adsorbed species that would rather dissociate than diffuse.

A larger variety can be achieved looking at hydrogen diffusion reactions. The different types of surface oxygen atoms and also the distances between OH and H residue make differences in the adsorption energy and also in the observed reactions. As seen before, the hydrogen is preferably found on the twofold coordinated oxygen atom, but the reaction to a neighboring threefold coordinated oxygen is possible and opens the gate to structures with greater distance. The reaction can take place with the OH residue being on a CUSb site:



The reaction shows a proton transfer reaction with a barrier height of 0.95 eV, but the NEB transition state has no imaginary frequency so that no rate can be derived, although the NEB path clearly shows a smooth barrier profile, compare Figure 2.9(a).

A further reaction, called Df-H-b, starting from the most stable inter-CUSA||O- μ_2 to the three-fold coordinated oxygen can be seen in Figure 2.9(b):



The barrier of the free energy is 1.50 eV, giving a rate constant at 300 K of $4.90 \times 10^{-13} \text{ s}^{-1}$. This process is so unlikely because a less favored O- μ_3 position is occupied and this position is also less stabilized by reason of the greater distance of OH_{surf} and OH_{ads} groups. This reaction increases the distance to a position further away than next neighbor. As mentioned before,

2. Water on $\alpha\text{-Al}_2\text{O}_3(11\bar{2}0)$

the nomenclature for these structures uses primes ($'$) to display the distance.

A similar reaction can be seen in Figure 2.9(c) for the OH being situated on inter-CUSb and the hydrogen being adsorbed on an O- $\mu_2^{(')}$ position, diffusing further away to O- μ_3'' , which is less in stability:



The free energy barrier is relatively high with 1.30 eV giving a rate constant $k_{300\text{K}} = 9.96 \times 10^{-1}\text{s}^{-1}$. The ' $'$ in the equation above is set in parentheses because it is the nearest possible O- μ_2 position, but not the nearest possible distance from the OH_{ads}.

Going one step further from reaction Df-H-c, the following reaction leads to the position where OH and H have the greatest possible distance with the applied periodic bounding conditions:



With an energy barrier of 0.94 eV the rate at 300 K is $1.1 \times 10^{-3}\text{s}^{-1}$, see also Figure 2.8(d). These H diffusion paths can be assembled to a longer diffusion path leading from inter-CUSb||O- μ_3 to O- μ_2' to O- μ_3'' and to the furthest possible O- μ_3''' . The first reaction was calculated but did not converge for unknown reasons. The two next steps of this hydrogen migration path were studied (Df-H-c and Df-H-d). The rate of the first step is unknown but it is assumed to be fast, because as the product a very stable O- μ_2 configuration is involved. The second reaction (Df-H-c) has a medium rate with 10^{-1}s^{-1} . The last step of this path is the slowest with 10^{-3}s^{-1} . The corresponding adsorption energy profile is different from that: -1.89, -2.09, -1.16 and -1.22 eV. One can conclude that hydrogen migration in principle is possible but not likely because the O- μ_2 acts as a trap for H that hinders further reactions.

Proton diffusion reactions are way more variable than OH diffusions or dissociation reactions, providing reaction rates at 300 K ranging from 10^{-13} to 10^{-3}s^{-1} . The barriers and therefore also rate constants for H-diffusion cover a wider range depending on the distance between OH and H and of course more importantly on the fact between which types of O- $\mu_{2/3}$ the proton is diffusing.

It was shown that reactions leading to another situation than next neighbored, increasing the distance between OH and H are less favorable since geometries with the residues further apart are energetically less stable (compare Table 2.3).

Rates for backreactions can also be calculated and the results are shown in Table 2.7.

As mentioned before an immense well known problem of GGA is that barriers are underesti-

2.3. Reactions and Microkinetic Model

Table 2.6.: Energy and free energy differences are given: $\Delta E = E(\text{product}) - E(\text{educt})$, $\Delta E^\ddagger = E^\ddagger - E(\text{educt})$, respective for G . The same is given for the transition state - educt. Thermodynamic properties are given at $T = 300\text{ K}$. k is the rate constant from eq. (1.28). The three types of reactions are dissociation (D), OH diffusion (Df-OH) and H diffusion (Df-H). “n.f.” indicates “not found”. Numbers are given in italics if no barrier was confirmed or found.

| Reaction Type | | $\Delta E(\text{eV})$ | $\Delta G_{300\text{ K}}(\text{eV})$ | $\Delta E^\ddagger(\text{eV})$ | $\Delta G_{300\text{ K}}^\ddagger(\text{eV})$ | $k_{300\text{ K}}(\text{s}^{-1})$ |
|-----------------------------------|---------|-----------------------|--------------------------------------|--------------------------------|---|-----------------------------------|
| H_2O dissociation | D-a | -0.50 | -0.52 | 0.01 | 0.002 | 5.76×10^{12} |
| | D-b | <i>0.59</i> | <i>0.53</i> | n.f. | n.f. | n.f. |
| | D-c | <i>-1.15</i> | <i>-1.27</i> | n.f. | n.f. | n.f. |
| OH diffusion | Df-OH-a | 0.19 | 0.22 | 0.35 | 0.39 | 1.88×10^6 |
| | Df-OH-b | -0.21 | -0.13 | 1.07 | 1.10 | 2.41×10^{-6} |
| H diffusion | Df-H-a | <i>0.76</i> | <i>0.58</i> | n.f. | n.f. | n.f. |
| | Df-H-b | 1.08 | 1.04 | 1.65 | 1.49 | 4.90×10^{-13} |
| | Df-H-c | 0.93 | 0.89 | 1.36 | 1.30 | 9.96×10^{-10} |
| | Df-H-d | -0.06 | -0.07 | 1.05 | 0.94 | 1.05×10^{-3} |

mated [40]. Optimizing structures with HSE06 is nearly impossible due to high cost and doing single point calculations on PBE optimized transition state is not very accurate and doesn't deliver better results (unpublished work by Dr. J. Wirth, Universität Potsdam).

2. Water on $\alpha\text{-Al}_2\text{O}_3(11\bar{2}0)$

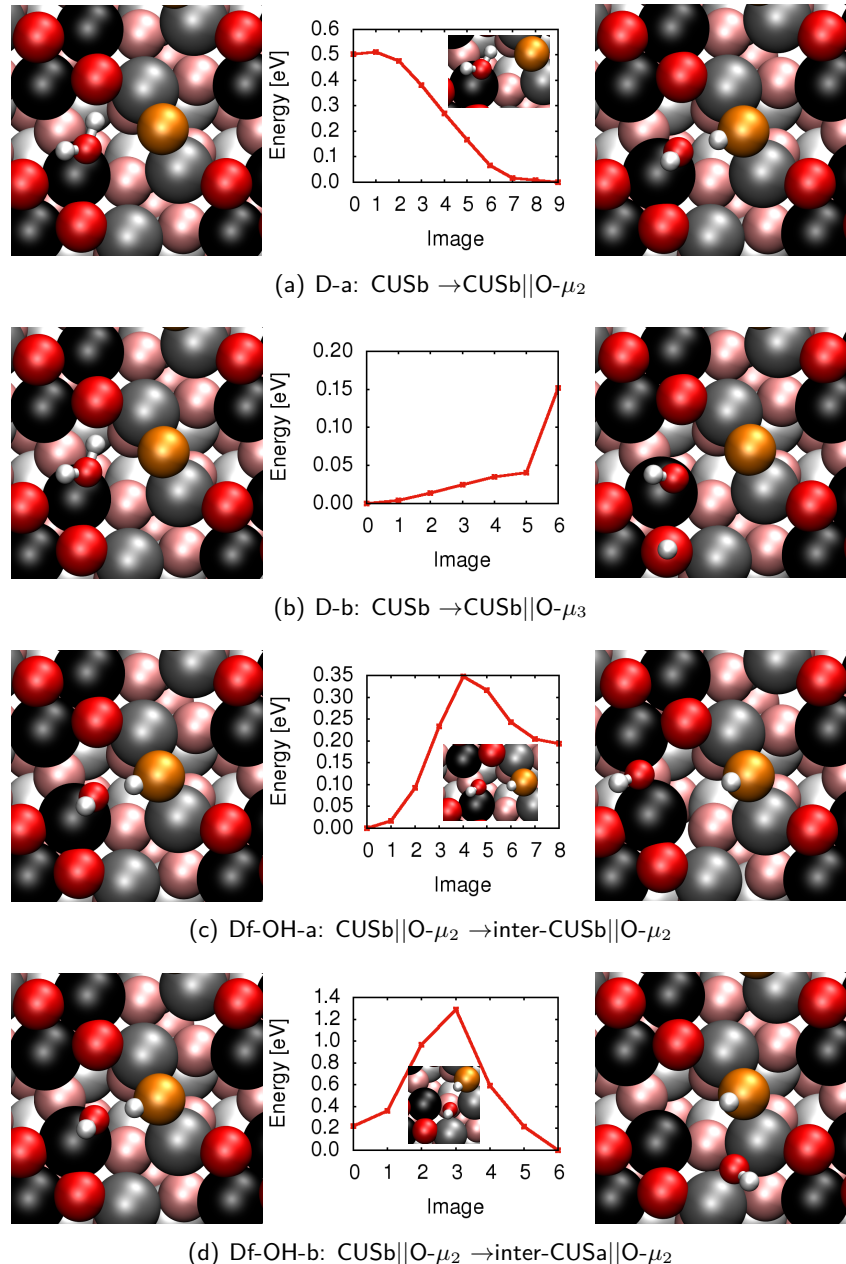


Figure 2.8.: Minimum energy paths with transition states (inlay; if available), and both educt (left) and product (right) states for D-a, D-b, D-c, Df-OH-a and Df-OH-b reactions, respectively. The color code is as explained above.

2.3. Reactions and Microkinetic Model

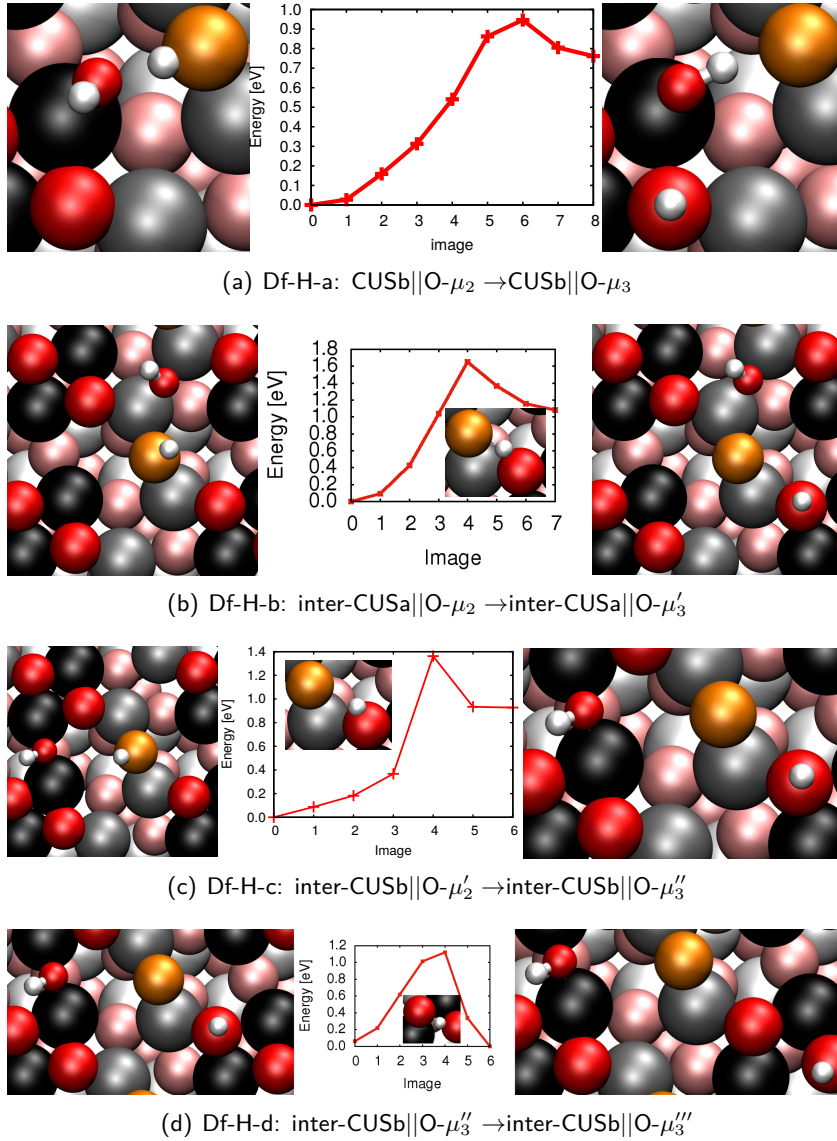


Figure 2.9.: Minimum energy paths with transition states, and both educt and product states for Df-H-a - Df-H-d reactions. The color code is as explained above.

2. Water on $\alpha\text{-Al}_2\text{O}_3(11\bar{2}0)$

Table 2.7.: Reaction rate constants for the backreactions \overleftarrow{k} (right) in comparison with forward reactions \overrightarrow{k} (left). These rates can be calculated via detailed balance $\overleftarrow{k} = \overrightarrow{k} e^{-\Delta G/k_B T}$. All values are given in s^{-1} at a temperature of 300 K.

| Reaction Type | $\overrightarrow{k}_{300 \text{ K}} (\text{s}^{-1})$ | $\overleftarrow{k}_{300 \text{ K}} (\text{s}^{-1})$ |
|---------------|--|---|
| D-a | 5.76×10^{12} | 1.17×10^4 |
| D-b | n.f. | n.f. |
| D-c | n.f. | n.f. |
| Df-OH-a | 1.88×10^6 | 9.86×10^9 |
| Df-OH-b | 2.41×10^{-6} | 1.69×10^{-8} |
| Df-H-a | n.f. | n.f. |
| Df-H-b | 4.90×10^{-13} | 1.49×10^5 |
| Df-H-c | 9.96×10^{-10} | 9.95×10^5 |
| Df-H-d | 1.05×10^{-3} | 7.12×10^{-5} |

2.4. Vibrational Frequencies

Vibrational spectroscopy is of interest because it is a great source of knowledge about chemical systems. The frequencies of vibrations give hints about the chemical environment as hydrogen bonds and other atoms nearby that bind to each other. These vibrational frequencies were calculated for the surface system adsorbed with OD. Our experimental partners from FHI use deuterated water (D_2O) instead of H_2O because the chemical reactivity is the same but the spectroscopic properties are clearer with their applied Laser system, so that all results presented in this particular section are given for D_2O . The experimental SFG spectra (Sum Frequency Generation) for the OD range of the low coverage regime for two different coverages are shown in Figure 2.10 as they were published in [60].

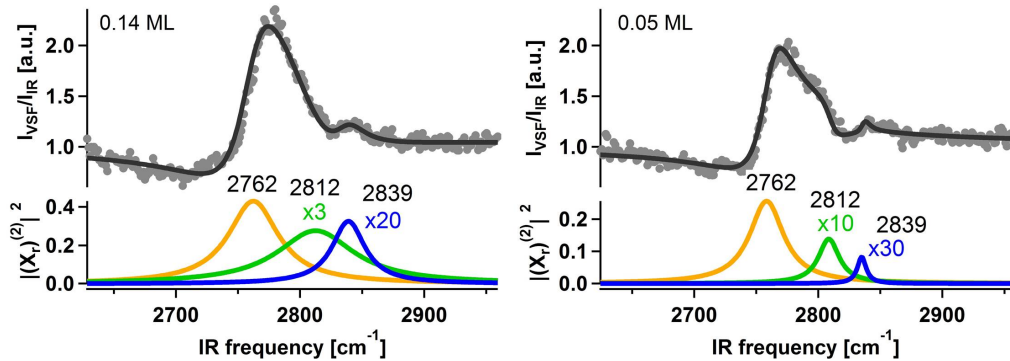


Figure 2.10.: Experimental SFG results for $(11\bar{2}0)$ surface with 0.14ML (mono layer, left spectrum) and 0.05ML water coverage (right) including fit. The experiment was conducted by Yanhua Yue, FHI Berlin. Coverage only influences intensity of the peaks but not the peak position itself. The different coverages are achieved via different preparing temperatures of the sample.

In experiment the alumina single crystal was cleaned in ethanol and Milli-Q water and dried with N_2 before being installed in the ultra high vacuum chamber. It was then sputtered in Ar, and annealed to high temperatures in ultra high vacuum (UHV, 2.5×10^{-10} mbar) and afterwards sputtered three times in oxygen at different temperatures. After this treatment, D_2O was brought onto the surface with a molecular beam source (MBS). For further experimental details see [60] and the supporting information therein. Test calculations with a symmetric slab (where at the top and the bottom water is adsorbed) were done, proving that the asymmetric model including dipole corrections is sufficient to describe the system. Only minor differences could be obtained. Details for this are given in the Appendix.

To calculate the modes in this work mainly two methods were applied: Normal mode analyses (see section 2.4.1) and power spectra from AIMD via velocity-velocity autocorrelation function

2. Water on $\alpha\text{-Al}_2\text{O}_3(11\bar{2}0)$

(section 2.4.3), however the latter results are not fully converged yet and have to be propagated tens to hundred ps instead of 1-2 ps, so only preliminary results will be shown to illustrate the power of this method.

The focus lies mainly on the position of the peaks rather than the intensities, because in the first place it is of greater importance what kind of vibrations gives which peak than the intensity of the peak itself. Also, it is still challenging to determine the frequencies in good comparison with experimental findings before heading to intensities.

In the power spectra from MD calculations the intensities are implicitly received and for the normal mode analyses this work follows two distinctive approaches: dipole corrections and Born effective charges.

In subsection 2.4.1, OD stretch vibrations are presented but also modes for higher coverage systems and lattice vibrations are examined. Subsection 2.4.2 gives the spectra including intensities determined via Born effective charges and in subsection 2.4.3 the results for spectra from the velocity-velocity autocorrelation function are shown.

2.4.1. Normal Mode Analysis

OD Vibrations

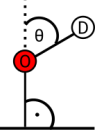
The normal modes are calculated within the harmonic approximation and depend on the mass and the spring constant of the bond. This ansatz is quite good for high frequency modes like OD stretch vibrations. We assume that the OD stretching modes for the three most stable structures would contribute to the spectrum the most. These wavenumbers are presented in Table 2.8 for different slab sizes, as given in Figure 2.2. Also the angle of the OD bond with respect to the surface is given, since vibrations that are in plane cannot be measured with SFG spectroscopy and hence the intensity is a function of this angle.

Following this approach we expect six modes, for each of the three an OD_{surf} and an OD_{ads} . In all cases the relationship between the two individual modes for each considered structure is portrayed by $\tilde{\nu}(\text{OD}_{\text{ads}}) > \tilde{\nu}(\text{OD}_{\text{surf}})$. This can be explained with the different reduced mass for both vibrations: The OD_{surf} oscillator has a slightly larger reduced mass since the deuterium is bound directly to the surface, whereas the adsorbed OD group can act more as a quasi-free OD group [53]. All these vibrations are clearly localized on one of the OD groups, which suggests that the normal modes ansatz is reasonable. Of course, normal modes of all molecular and next neighbor dissociated structures from 10 to the 25 slab layer model were calculated, although as it was mentioned in section 2.2 and is visible from Table 2.8 the slab was already converged

2.4. Vibrational Frequencies

Table 2.8.: Wavenumbers of normal modes for the different slab sizes: OD stretching modes for each of the most stable minima. All values are given in cm^{-1} ; in parentheses, the angle of the OD bonding vector to the surface normal (θ in $^\circ$) is provided. In each column, the left value reflects the adsorbed OD_{ads} group and the right wavenumber the surface OD_{surf} group, respectively. In the right part a sketch of the angle θ between the OD bond and the surface normal is shown.

| Layers | inter-CUSa O- μ_2 | CUSb O- μ_2 | inter-CUSb O- μ_2 | |
|--------|------------------------|----------------------|------------------------|--|
| 10 | 2731 (44), 2694 (36) | 2785 (26), 1711 (61) | 2692 (41), 2689 (54) | |
| 15 | 2728 (44), 2695 (36) | 2783 (24), 1812 (60) | 2711 (34), 2656 (60) | |
| 20 | 2729 (44), 2694 (35) | 2783 (24), 1838 (60) | 2715 (34), 2665 (58) | |
| 25 | 2728 (44), 2696 (35) | 2767 (59), 1750 (62) | 2764 (29), 2724 (41) | |
| exp. | | 2839, 2812, 2762 | | |



with 10 layers concerning OD stretch frequencies.

To consider the probability of observing these species, their respective Boltzmann weights P_i were evaluated:

$$P_i = e^{-G_i/(k_B T)}. \quad (2.3)$$

With this analysis it is possible to show the relative population for different temperatures, given in Table 2.9. In the temperature range relevant for the experiments, it is shown that the population of the species inter-CUSa||O- μ_2 clearly dominates and furthermore that the population of inter-CUSb||O- μ_2 is very low, compared to the others.

Table 2.9.: Boltzmann population P relative to the most stable inter-CUSa||O- μ_2 , calculated according to Equation 2.3 for 130, 300 and 400 K. Values are given for the 10 layer system.

| | P_{130K} | P_{300K} | P_{400K} |
|------------------------|-----------------------|----------------------|----------------------|
| inter-CUSa O- μ_2 | 1 | 1 | 1 |
| CUSb O- μ_2 | 1.4×10^{-6} | 6.1×10^{-3} | 3.2×10^{-2} |
| inter-CUSb O- μ_2 | 1.0×10^{-15} | 1.2×10^{-6} | 6.6×10^{-5} |

From the results for the frequencies of the three most stable structures (from Table 2.8), one can see, that for all slab sizes, there are four relevant modes to be expected. One of them is noticeable lower in energy that is due to hydrogen bonding (OD_{surf} vibration of CUSb||O- μ_2). Also the angle of the bonding vector with respect to the surface normal is very high (i.e. the bond is more in plain, values and schematic representation shown in Tab. 2.8) so that the expected intensity is remarkably lower and may be not visible in experiment because of the

2. Water on $\alpha\text{-Al}_2\text{O}_3(11\bar{2}0)$

angle dependence of the intensity in SFG.

With this in mind, we are able to predict three peaks, which fits well to the experimental results of Yanhua Yue from FHI Berlin (see Figure 2.10). Comparing these results in absolute numbers is not very impressive as before in the literature, but relative numbers are in good agreement, see results for experiment and all different sized layer slabs in Table 2.10. With this

Table 2.10.: Wave number differences $\Delta\tilde{\nu}$ are given in [cm^{-1}]. $\Delta\tilde{\nu}_1$ depicts the difference between the surface OD group of the inter-CUSa||O- μ_2 species and the respective surface OD group on O- μ_2 and $\Delta\tilde{\nu}_2$ is the difference between the same surface OD group and the adsorbed OD group on CUSb from CUSb||O- μ_2 .

| layers | $\Delta\tilde{\nu}_1$ | $\Delta\tilde{\nu}_2$ |
|--------|-----------------------|-----------------------|
| 10 | 37 | 91 |
| 15 | 33 | 88 |
| 20 | 35 | 89 |
| 25 | 32 | 71 |
| exp. | 50 | 77 |

it becomes clear, that for OD stretching bonds there is no trend visible, the 10 layer system already gives reasonable results and none of the employed larger slab models are an improvement.

Two problems of this approach are, that we neglect anharmonicities, that are especially important for hydrogen bonded vibrations and also the absence of neighbor effects, that can be solved by computing higher coverage systems.

The influence of higher coverage was examined for systems already presented in section 2.2. The coverage differs from 2D₂O molecules per supercell to four and twelve water molecules, which equals 1ML. Here the frequencies of the OD stretching modes are affected due to the neighbor adsorbates, for some structures more and for others less (e.g. the system with 2inter-CUSa||O- μ_2).

Dipole Intensities and Lattice Vibrations of Further Systems

TODO: *experimental results are still missing, compare modes of low coverage limit to spectra with higher coverage, ask Lu for more data of higher coverage.*

For the lattice vibrations the same normal modes of the 10 layer slab were checked to get a first impression into how the spectra can appear. But for a better description of the deeper lying phonon vibrations we need to consider more layers of the bulk in order to get more reliable results. From an experimental point of view it is suggested that SFG spectra can give

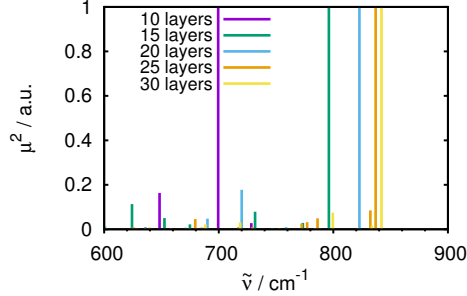


Figure 2.11.: Comparison of the spectra for different slab sizes from 10 to 25 layers for the clean surface obtained with normal mode analyses and intensities from dipole corrections.

insight into at least three atomic layers of the bulk. To make sure these are described well, the system size was expanded, performing calculations for the most stable adsorption geometries for more layered systems, going up to $6 \times 5 = 30$ atomic layers (with five being the number of atomic layers in the unit cell in z direction, compare Figure 2.2), for the clean surface and for 25 layers for the adsorbate covered surface. These more layered optimized geometries do not differ strongly from the ten layer ones that were presented in Section 2.2, Figure 2.4 and hence are not shown. Respective adsorption energies can be found in Table 2.4. For the low energy modes, one has to keep in mind, that normal modes may not be a perfect description of these deeply delocalized vibrations but still might be sufficient.

In this section intensities are elaborated from dipole corrections. The results for the clean surface are shown in Figure 2.11. For different sized slabs, the results differ largely. Especially the ten layer system is shifted strongly to lower energy compared to the other slab sizes. In Table 2.11 can be seen that the most intense peak is shifted to higher wavenumbers with increasing slab size. All spectra shown in this section were normalized to the most intense peak.

Table 2.11.: Comparison of the results for the different slab sizes with NMA: most intense peak from dipole corrections of the lattice vibrations for the clean surface.

| Layers | 10 | 15 | 20 | 25 | 30 |
|--------------------------------|-----|-----|-----|-----|-----|
| $\tilde{\nu} [\text{cm}^{-1}]$ | 700 | 796 | 823 | 837 | 842 |

While this trend is true for the clean surface and the lattice region of the covered systems, it does not hold for the OD vibrations regime. As it was already mentioned the OD frequencies seem to be converged for the 10 layer slab and both position and intensity show no eminent difference, see Figures 2.12, 2.13 and 2.14. The exact wavenumbers differ slightly for the OD regions but in general are in good agreement, except for the hydrogen bonded peak in the

2. Water on $\alpha\text{-Al}_2\text{O}_3(11\bar{2}0)$

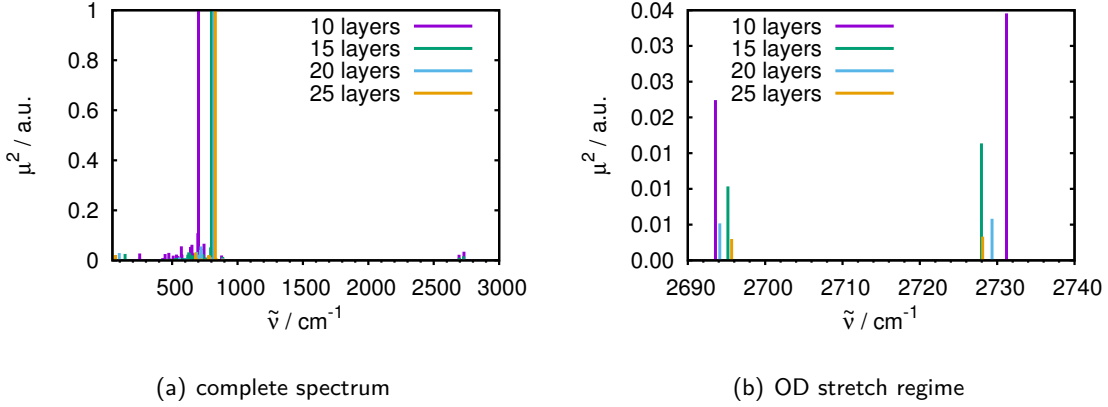


Figure 2.12.: Comparison of inter-CUSa||O- μ_2 frequencies for different slab sizes in z direction, obtained by normal mode analyses with intensities from dipole corrections.

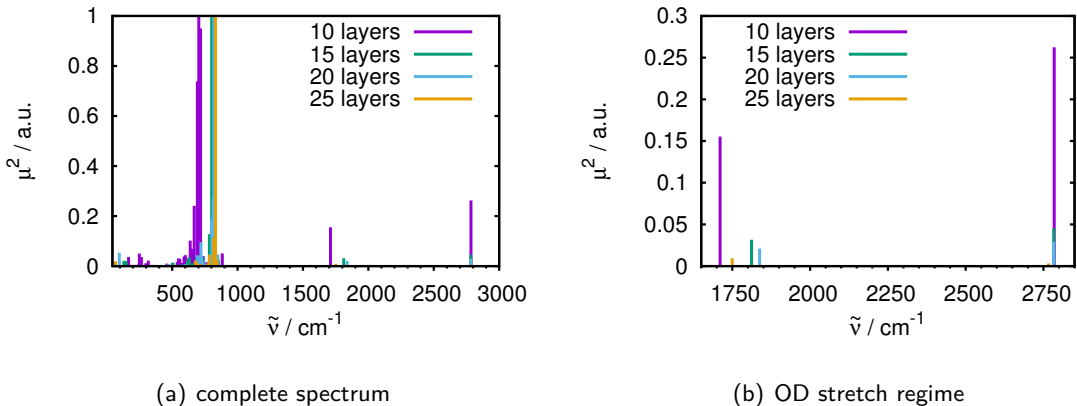


Figure 2.13.: Comparison of CUSb||O- μ_2 frequencies for different slab sizes, obtained by normal mode analyses with intensities from dipole corrections.

CUSb||O- μ_2 , confer Figure 2.8. However, the lattice region below 1000 cm^{-1} is systematically affected, as in the clean surface system. *TODO: which one fits the experimental results best? wait for experimental results*

The higher coverage systems (see Figures 2.5-2.6) were also examined. The total spectrum and the OD range are shown in Figure 2.15, including a comparison between the systems with two D₂O molecules and the corresponding systems with only one adsorbate. For all three systems the agreement is reasonably good. If the water molecules interact strongly with each other, the peaks are shifted heavily. The system inter-CUSa||O- μ_2 +CUSb||O- μ_2 ((a) and (b) of Figure 2.15) seems to be affected only weakly, inter-CUSa||O- μ_2 +inter-CUSa||O- μ_2 ((c) and (d)) is shifted slightly more. The system CUSb+CUSb||O- μ_2 ((e) and (f)) however, is shifted signif-

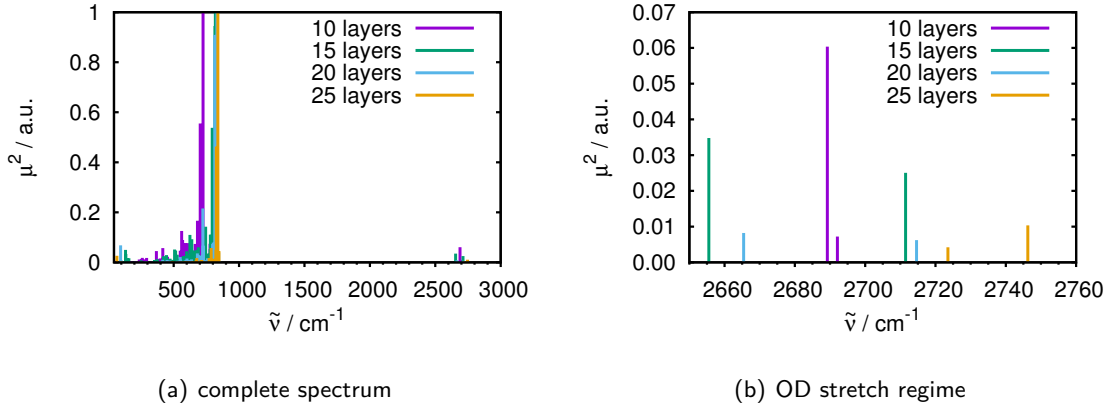


Figure 2.14.: Comparison of inter-CUSb||O- μ_2 frequencies for different slab sizes in z direction, obtained by normal mode analyses with intensities from dipole corrections.

icantly, displaying a strong interaction between the molecularly adsorbed and the dissociated groups, stabilizing each other. This is interesting since in the adsorption energy the three systems acted differently, the inter-CUSA||O- μ_2 +inter-CUSA||O- μ_2 decreased its stability, whereas the system inter-CUSA||O- μ_2 +CUSb||O- μ_2 did not change and CUSb+CUSb||O- μ_2 even was more stabilized. With this in mind, it makes sense that the system, in which the adsorption energy is merely affected also shows hardly any difference to the single adsorption in the spectrum. On the other hand, the system where the molecular water is stabilized by its dissociated neighbor, the spectrum is shifted strongly. The inter-CUSA||O- μ_2 +inter-CUSA||O- μ_2 is more balanced, because the geometry does not change largely and only the adsorption energy is affected (in a destabilizing way).

Looking at the spectrum of the system with four adsorbed water molecules (1/3 coverage) we obtain Figure 2.16. All of these water molecules are adsorbed in inter-CUSA||O- μ_2 , see Figure 2.6(a) and 2.16, which is the most stable and hence the most probable adsorbed species. We see as expected the stretch vibrations of the adsorbed residue at higher wavenumbers. There are three modes for asymmetric (OD oscillators in contrary phases) and one for symmetric stretch vibrations (all OD oscillators in phase) around 2740 cm^{-1} . At lower wavenumbers (between 2691 and 2693 cm^{-1}) there are localized OD_{surf} vibrations. Below that there are delocalized combined vibrations of lattice and OD. In comparison to the singly adsorbed system (red line) there is an astonishing agreement, both in the OD range and the lattice region.

In contrast to the latter systems, for the 1ML system it is not easy to compare to the singly adsorbed species, since it consists of a complex mixture of twelve adsorbed OD residues (on CUSb, inter-CUSA and inter-CUSb), as well as twelve surface OD groups on O- μ_2 but also

2. Water on $\alpha\text{-Al}_2\text{O}_3(11\bar{2}0)$

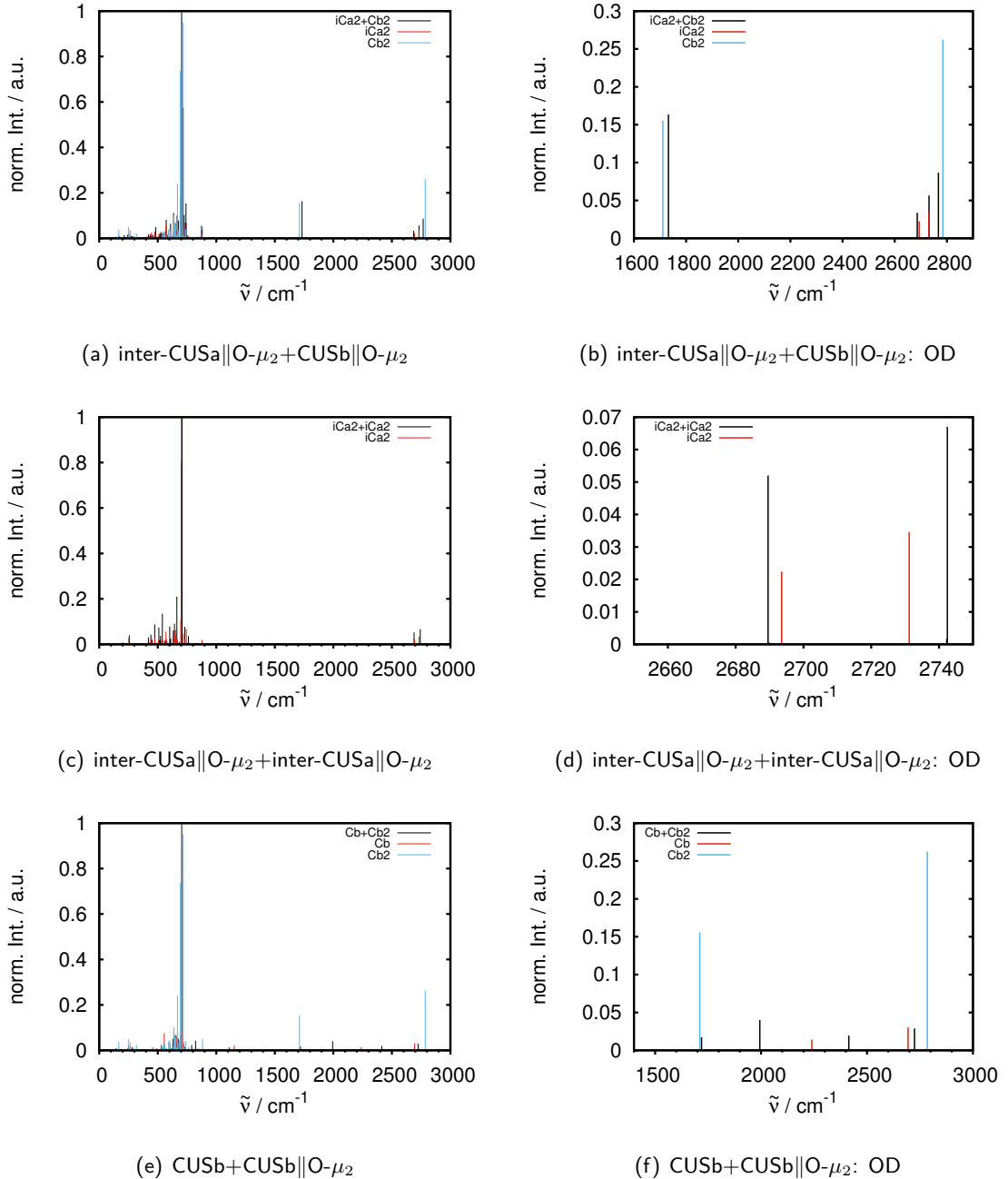


Figure 2.15.: Peaks from normal mode analyses and dipole intensities for two water molecules per supercell (10 layers) in comparison with the corresponding systems with one water molecule. The left row shows the complete spectrum and the right row the OD range.

the less favorable threefold coordinated O- μ_3 . Due to this magnitude of different species, the system possesses many peaks in the OD region, see Figure 2.17. Hydrogen bonding and in-

2.4. Vibrational Frequencies

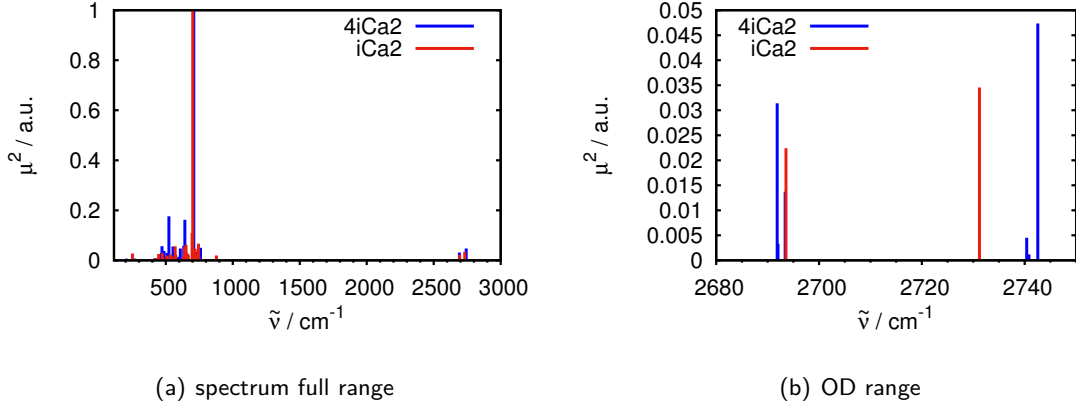


Figure 2.16.: Peaks from normal mode analyses and dipole intensities for four water molecules per supercell (10 layers). (a) shows the full spectral range and (b) only the OD range above 2680 cm^{-1} . The short notation stands for iCa2=inter-CUSa||O- μ_2 .

teraction between groups shift many of the peaks. Below 900 cm^{-1} delocalized OD and lattice vibrations can be found (panel (a)). In the region between 872 and 1117 cm^{-1} (shown in (b) of Figure 2.17) there are bending like vibrations of mostly O- μ_2 D groups. From ≈ 2000 to 2740 cm^{-1} various OD stretch vibrations occur. These are split into three distinct regions: From ≈ 2000 - 2220 cm^{-1} in plane vibrations of strongly hydrogen bonded species can be found. From 2400 - 2450 cm^{-1} in plane vibrations of non hydrogen bonded species occur and above 2550 cm^{-1} out of plane OD stretching bonds appear. As before, the agreement between dif-

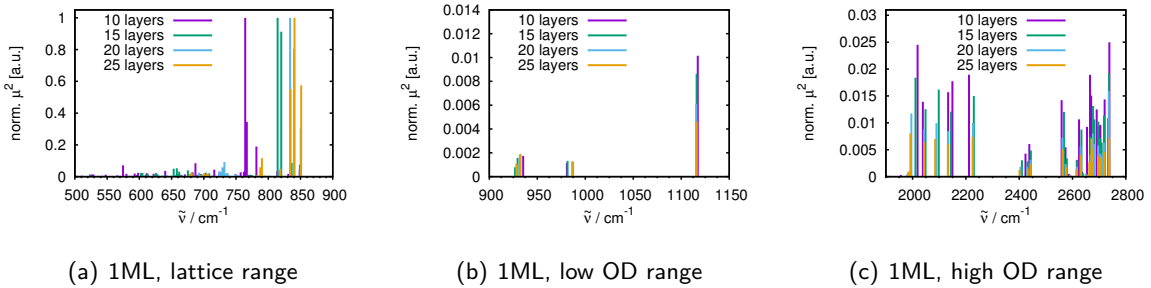


Figure 2.17.: Comparison of the spectra of the fully with D_2O covered surface. Shown is a comparison between the different slab sizes for (a) the lattice region, (b) the low energy OD range with butterfly like vibrations and (c) the high energy OD range. The regions that are not shown do not contain peaks.

ferent sized slab models in the OD range (without hydrogen bonding) is very good (Figure 2.17(c)), in the hydrogen bonded region around 1116 cm^{-1} is convincing (Figure 2.17(b)) and

2. Water on $\alpha\text{-Al}_2\text{O}_3(11\bar{2}0)$

only in the lattice region (Figure 2.17(a)) is slightly different with the highest energy peak shifted to higher energy with increasing slab size, which is the same trend as for the clean surface and the low coverage systems.

Apart from the most stable surface termination (called O-I in [59]), calculations of the second most stable surface termination (O-II) were done, where the uppermost O layer is “missing”. Frequencies were analyzed of the clean surface and the fully covered system, for both the 10 and 25 layer systems. In Figure 2.18 the intensities from dipole corrections for the clean (a)

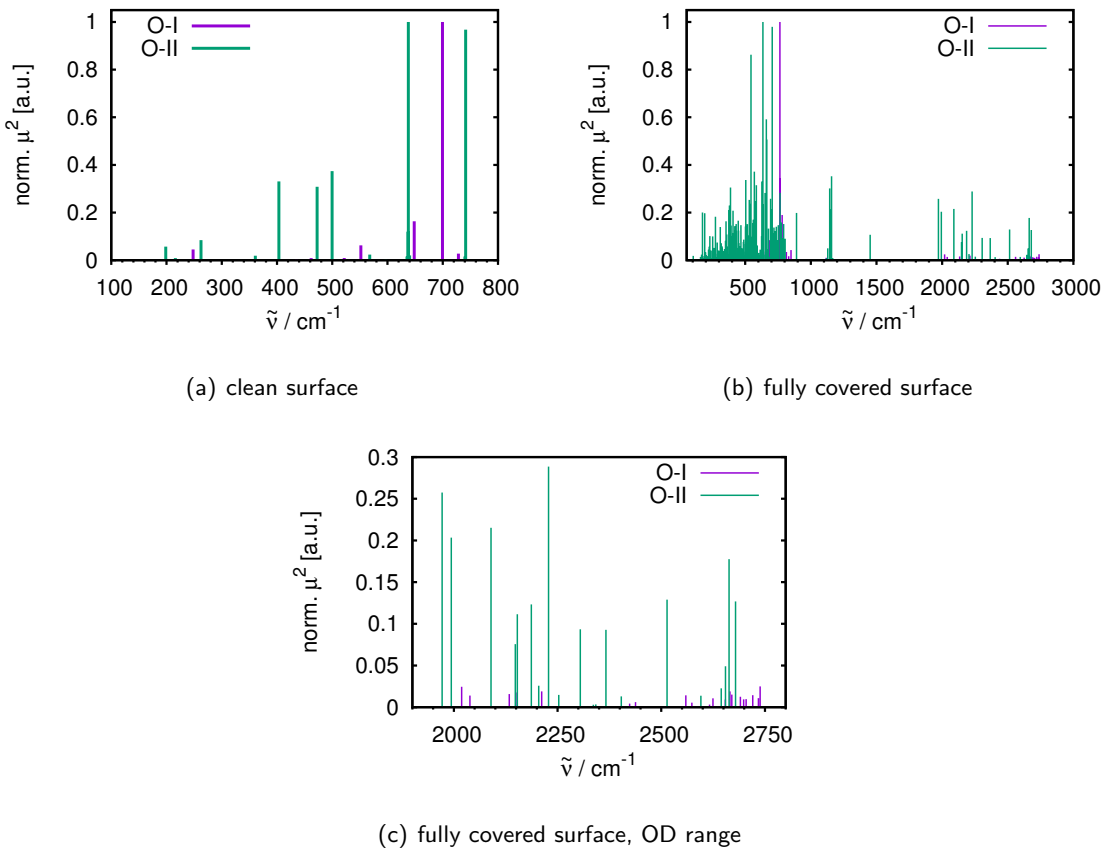


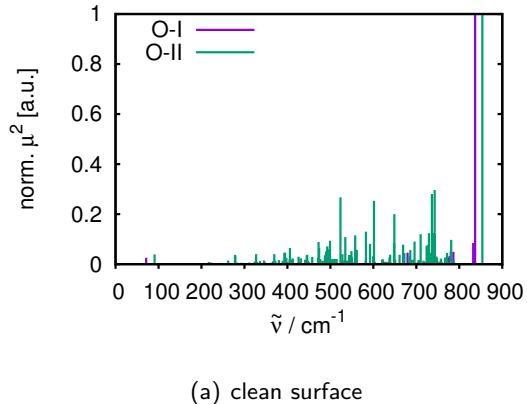
Figure 2.18.: Comparison of the 10 layer slab spectra calculated with normal mode analysis and intensities from the dipole corrections. The clean surface (a), O-I termination (most stable under the whole range of chemical potential) and O-II termination (see Kurita [59], also relatively stable over a wide chemical potential range). The comparison of the fully covered O-I and O-II terminations is shown in (b) with a detailed view of the OD range in (c).

and the fully covered surface termination O-II ((b), (c)) in comparison to the more stable O-I termination are given for the 10 layer slab. For the clean surface, the spectra deviate by shifted

2.4. Vibrational Frequencies

peaks around 50 cm^{-1} and different intensity distributions. In contrast to that, the differences for the fully covered surfaces are more pronounced due to the different structures including especially more molecularly adsorbed water for the O-II termination.

Also for a larger slab with 25 layers, this comparison was done, see Figure 2.19 They are very



(a) clean surface

Figure 2.19.: Comparing the O-I and O-II terminated clean surface of the 25 layer system shows very similar results for both systems are obtained. The most intense peak is shifted by around 20 cm^{-1}

similar and the most intense peak is only shifted by 20 cm^{-1} . For the O-I termination the intensities are weaker than for the O-II terminated surface for most vibrations, but overall the differences are not so pronounced. In the larger slab model there are many more bulk atoms than surface atoms that can contribute to vibrations. Due to this the differences between O-I and O-II termination get less significant for the larger system.

TODO: continue here when the calculations are ready! Compare O-I and O-II for 10 and 25 layer slabs, for fully covered.

2.4.2. Born Effective Charges

As a second method of obtaining intensities, Born effective charges were evaluated. These results were obtained for the three most stable adsorbed systems with 10 layers. For getting the spectrum an angle of the IR beam of 45° was assumed. Since both the dipole corrections intensities and the BEC calculations are based on normal modes, the frequencies are equal and only the intensities can differ. In Figure 2.20 the spectra for the three most stable structures can be seen, (a) depicts the whole range and (b) the OD range only. The peak around 1700 cm^{-1} comes solely from the hydrogen bonded CUSb||O- μ_2 OD group. The other non hydrogen bonded peaks come above 2500 cm^{-1} and the lattice region can be seen below 1000 cm^{-1} .

2. Water on $\alpha\text{-Al}_2\text{O}_3(11\bar{2}0)$

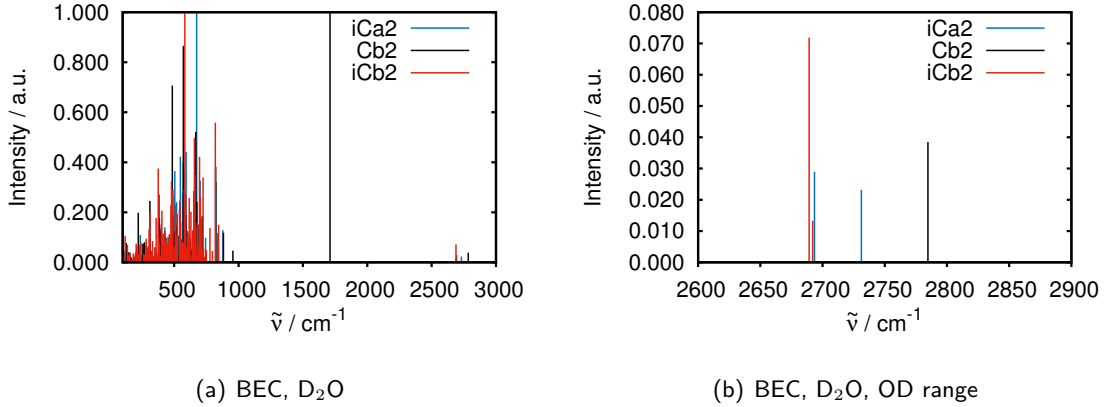


Figure 2.20.: IR spectrum with intensities based on Born effective charges (BEC) evaluation for the three most stable species, (a) full spectrum, (b) OD range above 2600 cm⁻¹.

In comparison to the results from the dipole corrections, of course, the positions of the peaks are unaffected. For inter-CUSa||O- μ_2 the intensities in the OD range are nearly the same, although the more intense peaks are changed. In the lattice region the agreement is not as excellent. For the OD region of CUSb||O- μ_2 , the agreement is worse, BEC predicts the H-bonded peak at 1711 cm⁻¹ to be the most intense whereas the dipole corrected intensities give this in the lattice region which is in general very distinctive. Concerning the inter-CUSb||O- μ_2 the OD region shows good agreement, also the more intense peak is the same. Again in the lattice region, the difference is larger. This might be due to the fact, that low energy modes are less precisely represented by normal modes and both methods give low quality results.

In Table 2.12 a comparison between dipole and BEC intensity results of the OD stretch vibrations can be found. The results are in reasonable agreement for inter-CUSa||O- μ_2 and

Table 2.12.: Comparison of the IR intensities for the 10 layer system obtained from dipole corrected calculations and from the Born effective charges based approach. It was normalized to the highest intensity peak.

| | $\tilde{\nu}$ [cm ⁻¹] | Intensity [a.u.] | |
|------------------------|-----------------------------------|------------------|-------|
| | | dip. | BEC |
| inter-CUSa O- μ_2 | 2731 | 0.034 | 0.023 |
| | 2694 | 0.022 | 0.029 |
| CUSb O- μ_2 | 2785 | 0.262 | 0.038 |
| | 1711 | 0.155 | 1.0 |
| inter-CUSb O- μ_2 | 2692 | 0.007 | 0.013 |
| | 2689 | 0.060 | 0.072 |

2.4. Vibrational Frequencies

inter-CUSb||O- μ_2 , but are deviate largely for the hydrogen bonded CUSb||O- μ_2 system. Corresponding *intensities* from AIMD calcualtions are presented in section 2.4.3.

2.4.3. Velocity-Velocity Autocorrelation Function

The velocity-velocity autocorrelation function that is evaluated from AIMD calculations and Fourier transformed to get information from the time to the frequency domain. This is a totally different ansatz to calculating a spectrum. No frequency analysis has to be done, *i.e.* no harmonic approximation is applied. Instead the classical movement of the nuclei at a specific temperature is taken into account. At 300K for the clean surface (30 layers) and the three most stable adsorbed structures (inter-CUSA||O- μ_2 , CUSb||O- μ_2 and inter-CUSb||O- μ_2 , 10 layers each) the respective MD were calculated, starting from the minimum structure. The presented spectra are only preliminary results, since the propagation duration is substantially too short, so that it can not be excluded, that the system is not converged properly. Usually, for a converged study, a preequilibration phase of several ps is assumed and afterwards the production run is up to 100 or even more ps, but this results still give a good first glimps to what the spectrum could look like.

The shown “intensities” correspond to oscillator amplitudes and can not be perfectly reasonably compared to the IR intensities obtained from BEC or dipole corrected normal modes, but still as a first impression it is a useful approximation.

For the clean surface, the 30 layer model was applied, with a propagation duration of 5 ps. As for the normal modes results, all peaks are below 900 cm⁻¹, see Figure 2.21. The most intense peak in the power spectrum can be observed at significantly lower energy than for any normal mode based result. Also more peaks are present in the whole range from 0 to around 900 cm⁻¹.

The results for the adsorbed species were obtained by AIMD calculations of the 10 layer system at a temperature of 300K. Again, the three most stable species were researched. The system inter-CUSA||O- μ_2 was propagated for 3.68 ps. The respective spectrum is shown in Figure 2.22(a) and shows two intense peaks in the OD region at 2691 and 2726 cm⁻¹. These two fit very well to the peaks in the normal mode calculations at 2694 and 2731 cm⁻¹. In the lattice region, as it could be observed for the clean surface as well, the intense peaks are at lower wavenumbers and there is no strong agreement.

The spectrum of the CUSb||O- μ_2 system can be seen in Figure 2.22(b). It was propagated for 3.67 ps. The OD range shows one clear peak at around 2757 cm⁻¹, that can be compared to the non-hydrogen bonded peak at 2785 cm⁻¹ in the normal modes. In contrast to that, the hydrogen bonded peak that can be found in the normal modes calculation at 1711 cm⁻¹ is

2. Water on $\alpha\text{-Al}_2\text{O}_3(11\bar{2}0)$

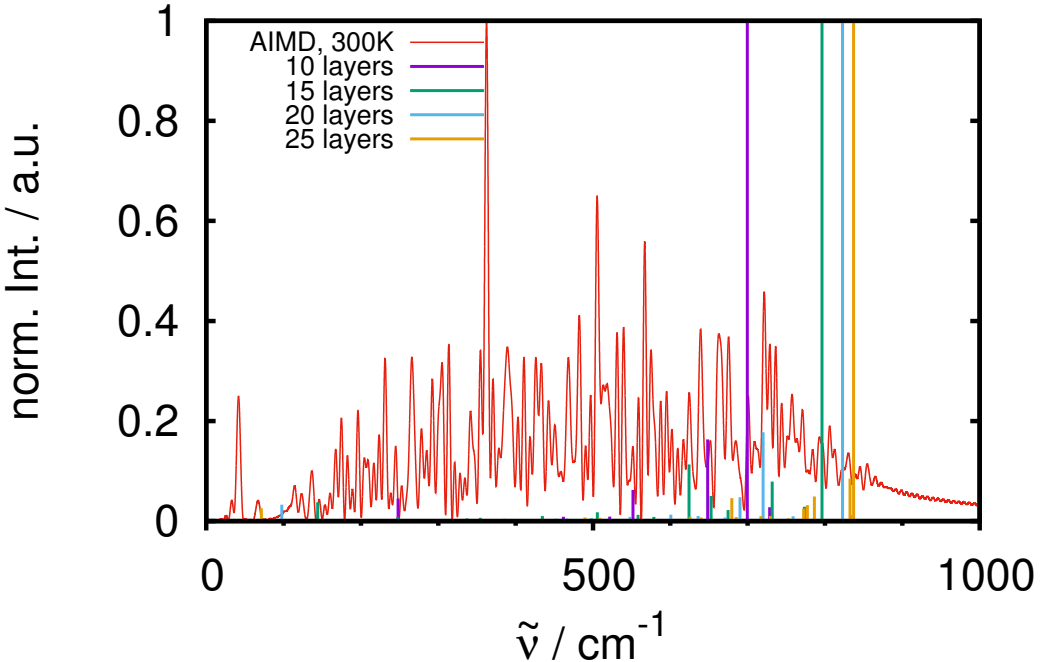


Figure 2.21.: Power spectrum of the clean surface of the 30 layer slab, calculated from velocity-velocity autocorrelation function of a canonical (NVT) AIMD trajectory at 300 K (5000 steps, 5 ps). In addition to the power spectrum, the stick spectra of the dipole corrected normal modes for different slab sizes are shown.

given in the power spectrum as a multitude of small peaks smeared in the region between 1300 and 2100 cm^{-1} , indicating delocalization between the O_{ads} and O_{surf} . The lattice region the intense peaks are distributed wider and also the most intense peak of the lattice region is at a higher energy than the normal modes suggest.

For the inter-CUSb||O- μ_2 species with a trajectory duration of about 3.68 ps, the OD region is in very good agreement with the normal mode results (see Figure 2.22(c)). Compared to the normal modes where we observe two peaks, there is one broad peak around 2694 cm^{-1} that covers both peaks from the normal modes (2689 and 2692 cm^{-1}). It is possible that both groups overlap and lead to the broad peak. Also in the lattice region there is good compliance, the most intense peaks are only separated by 20 cm^{-1} which is the best result for the computed systems.

Although these results are far from being converged, the agreement with normal mode results is very good and lets hope for even more accurate results with longer propagation duration.

2.4. Vibrational Frequencies

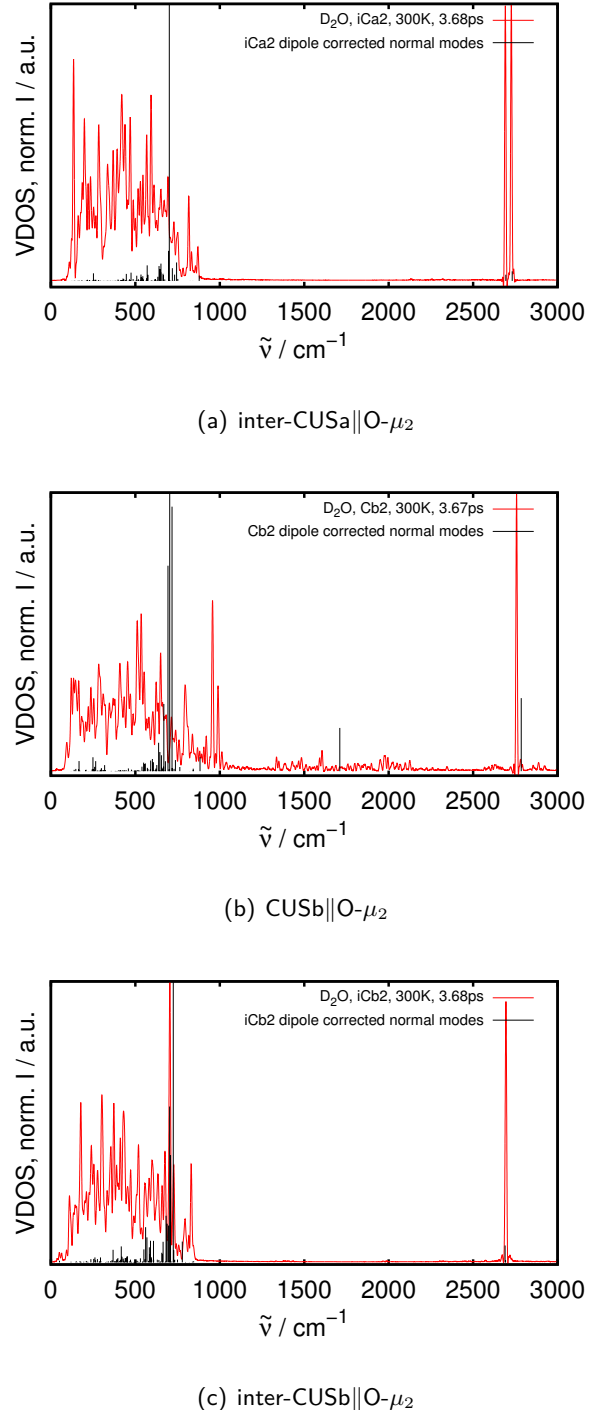


Figure 2.22.: Power spectra are shown in red, obtained from NVT AIMD trajectories at 300K for the geometries (starting points were geometry optimized structures at 0 K) of the most stable structures via velocity-velocity autocorrelation function. Duration of the trajectories is given inside the figures and is approximately 3.7 ps. In black the spectrum with intensities from dipole corrected normal modes is shown for comparison.

3. Water on $\alpha\text{-Al}_2\text{O}_3(0001)$

The (0001) surface is the most stable surface site of alumina under UHV conditions, and was subject of several studies so far [4, 59, 62, 63] *TODO: cite some more, theory and experiment*. Both experimental and theoretical studies discovered characteristics and specialties of this crystal cut. In our workgroup previous work was done concerning the stability of low limit water coverage and their vibrational spectroscopic behaviour, reaction pathways between these stable minima, but also studying higher water coverages and hydroxylated surface systems [52–54].

In this work, the focus lies on two topics:

- (i) Understanding the scattering processes of a water molecule (D_2O) being shot at the surface with a molecular beam source with the help of AIMD and
- (ii) The improvement of reaction rates with different methods beyond GGA functionals (as PBE).

First, the surface and the most stable adsorption patterns are introduced (section 3.1), followed by the results for the molecular beam scattering [64] (section 3.2) and the improvements for the reaction rates (see section 3.3).

3.1. Surface Model and Static Calculations

The most stable surface cut is a stoichiometric, Al terminated one, and in contrast to the $(11\bar{2}0)$ surface there is only one type of Al-CUS atom, which acts as a reactive Lewis-acid site. Also, all oxygen atoms are threefold coordinated, that leads to a topography not as complex as for the higher indexed surfaces. We apply here a 2×2 supercell with vectors that were optimized from the bulk structure vectors (previous work of Dr. J. Wirth [52]). The surface slab consists of nine atomic layers, that equals three repeating units in z direction of the type $\text{Al}-\text{O}_3-\text{Al}\dots$, with the top five layers being allowed to relax during optimization and AIMD and the lowest four layers being fixed to bulk values, see Figure 3.1. The unit cell vectors in there are equal to $\underline{a} = \underline{b} = 9.66 \text{ \AA}$ and a 60° angle between them. The \underline{c} -vector of the slab model is perpendicular to the plane spanned by \underline{a} and \underline{b} and is 31.4 \AA long, hence the vacuum gap between two slabs in this direction is 26.4 \AA . The stability, vibrations

3. Water on $\alpha\text{-Al}_2\text{O}_3(0001)$

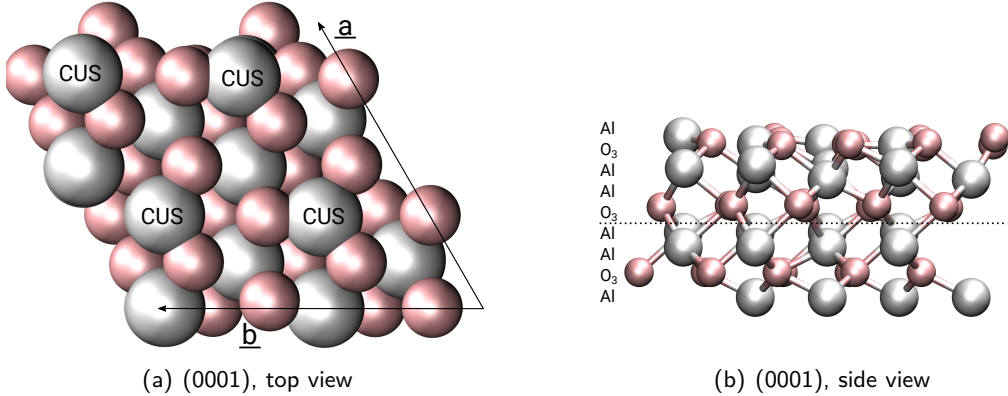


Figure 3.1.: Surface model of the (0001), the most stable surface cut under UHV conditions. The top view (a) shows four Al CUS atoms, that are surrounded by three threefold coordinated surface oxygen atoms. (b) reveals the side view of the Al terminated surface cut in detail with the atomic layers.

and reactivity of one water molecule per 2×2 supercell were already studied by Dr. Jonas Wirth. As it was published in [52], there is one molecular minimum on top of a CUS atom and three dissociated states (see Figure 3.2): the next neighboring 1-2 dissociated state, the 1-4 dissociated structure with the hydrogen atom being one position further and the 1-4' that is the configuration with the greatest possible distance for this slab size. From these, the 1-2 dissociated species is the most stable one and the 1-4' is the least stable one, see Table 3.1. For the stability of the molecular and the 1-4 dissociated species, the situation is more controversial in the literature TODO: cite from Jonas paper the other works. In our periodic DFT studies with VASP, it lies between the previously mentioned ones, depending on the exact method employed, for PBE+D2 the molecular adsorbed species is more stable than 1-4, for the functional PW91+D2 the 1-4 dissociated is more stable, whereas PW91 without dispersion corrections gives the same adsorption energy for both species (the values for the adsorption energy are calculated analogously to the (11 $\bar{2}$ 0) surface cut, Equation (2.1)). Calculations with an atom centered basis instead of plane waves with the crystal code show, that for most basis sets the molecular species is more stable and for others, they are both equal in adsorption energy, see Section 3.3.

Of course, there are reactions linking these minima, dissociation, OH- and H-diffusion were studied, as well as rotation of an OH group and molecular water diffusion from CUS to CUS. The latter two do not play a crucial role in this work, especially the CUS to CUS diffusion of molecular water is very improbable due to the slow reaction rate. Adsorption energies and reaction rates that are of importance for this work are shown in Table 3.1 and 3.2, these PBE

3.1. Surface Model and Static Calculations

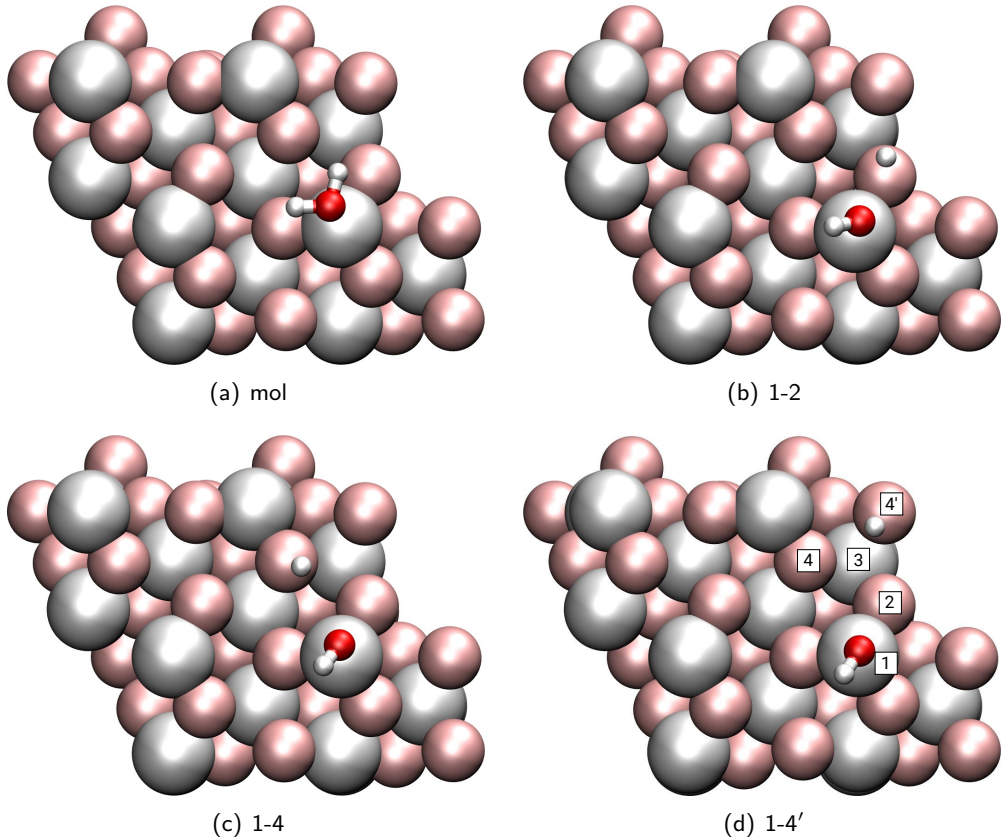


Figure 3.2.: Adsorption geometries of the molecular and the three dissociated species. Adsorption energies for these species can be found in Table 3.1. Additionally, panel (d) shows the numbering of the surface atoms that provides the nomenclature.

results were unpublished work obtained by Dr. J. Wirth.

Table 3.1.: Adsorption energies for the stable minima in eV. All values were calculated with PBE including D2 dispersion corrections and are unpublished work of Dr. J. Wirth.

| | E _{ads} [eV] | | | |
|--|-----------------------|-------|-------|-------|
| | mol | 1-2 | 1-4 | 1-4' |
| | -1.31 | -1.69 | -1.30 | -1.21 |

The desorption process from the surface itself was studied, by starting from the molecular minimum, gradually doing optimizations with greater O-surface distance and letting everything relax except for the c coordinate of the water-oxygen atom. This calculations gives an energy profile for the adsorption/desorption but no barrier could be found (see Figure 3.3), so the underlying adsorption process is assumed to be barrierless.

3. Water on $\alpha\text{-Al}_2\text{O}_3(0001)$

Table 3.2.: Reaction rate constants k in s^{-1} at 300 K with corresponding barrier heights ΔE^\ddagger and $\Delta G_{300\text{K}}^\ddagger$ in eV for the processes connecting the minima. Calculations were done with PBE+D2 (also from unpublished work of Dr. J. Wirth).

| | reaction | | | back reaction | | |
|-----------|---------------------|-----------------------------------|----------------------|---------------------|-----------------------------------|----------------------|
| | ΔE^\ddagger | $\Delta G_{300\text{K}}^\ddagger$ | $k_{300\text{K}}$ | ΔE^\ddagger | $\Delta G_{300\text{K}}^\ddagger$ | $k_{300\text{K}}$ |
| diss-1-2 | 0.13 | 0.11 | 8.0×10^{10} | 0.50 | 0.50 | 2.3×10^4 |
| diss-1-4 | 0.19 | 0.14 | 2.8×10^{10} | 0.19 | 0.14 | 2.7×10^{10} |
| diff-2-4 | 0.82 | 0.68 | 2.7×10^1 | 0.44 | 0.29 | 9.1×10^7 |
| diff-2-4' | 0.81 | 0.67 | 3.8×10^1 | 0.33 | 0.20 | 3.1×10^9 |
| diff-4-4' | 0.61 | 0.41 | 7.1×10^5 | 0.51 | 0.33 | 1.7×10^7 |

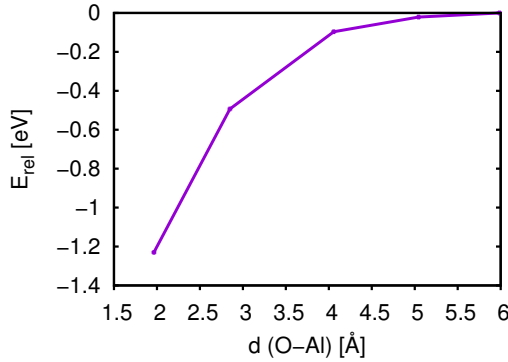


Figure 3.3.: Energy profile of the adsorption process, relative to the energy of the system with a distance of 5.98 Å. $d(\text{O-Al})$ denotes the distance between the oxygen atom of the water and the Al-CUS where the water is/was adsorbed molecularly.

3.2. AIMD for MBS Process

Molecular beam experiments have shown recently that water is able to adsorb both molecularly and dissociatively on an $\alpha\text{-Al}_2\text{O}_3(0001)$ surface. The results show an enhanced dissociation probability compared to “pinhole dosing”, which may be referred to as adsorption under thermal equilibrium conditions. However, precise mechanistics of the ongoing reactions and their relative probabilities are not known. In this work *ab initio* molecular dynamics calculations were conducted to unravel this process. These results were published in [64]. In these simulations heavy water (D_2O) collides with the $\alpha\text{-Al}_2\text{O}_3(0001)$ surface. This was done in comparison to the results of R. Kramer Campen, Interfacial Molecular Spectroscopy group, FHI Berlin. Previous studies by Hass *et. al.* [62, 63] discussed the idea whether water will adsorb molecularly and dissociate in a consecutive step or if it can dissociate directly. This study considered an adsorbed water that was propagated rather than water being shot on the surface.

3.2. AIMD for MBS Process

To tackle this question, AIMD calculations were conducted for a water molecule approaching the surface, with different beam and surface models applied.

3.2.1. Beam Model

For the understanding of a Molecular Beam source experiment, the introduction of a beam is an essential part of the model. However, it was not possible to compute a fully realistic beam that was statistically converged, which would require wide knowledge about energy and velocity distributions and a systematic high dimensional sampling, that is not feasible with the computational power available at the moment. Instead as a first order approach, a single, rigid water (D_2O) molecule (initial parameters are $d_{OD} = 0.97\text{\AA}$ and bond angle of 104.5°) was sent perpendicularly from a center of mass position from a distance of 4\AA onto the surface, in agreement with the experiment. Also higher distances were tested but no difference could be detected, see Appendix for more information. Having these degrees of freedom excluded, six are still left (see Figures 3.4, 3.5 and Table 3.3): two for the impact site $[a_0, b_0]$ as it is given relative to the supercell vectors \underline{a} and \underline{b} , three Euler angles α , β and γ for the rotational orientation of the molecule with respect to the surface and the kinetic energy E_{kin} that gives the molecule a momentum towards the surface, solely as translational motion, no vibration or rotation included. These parameters are varied systematically to gain insight into the process. As was mentioned before, the barriers can be high (and corresponding rates low), especially for the H-diffusion reactions, but the adsorption process itself is barrierless, and additionally the incoming water molecule holds kinetic energy so that processes, that are slow at room temperature otherwise, can be speeded up.

Further details on the improvements of this simplest model are made in subsection 3.2.6, that address clustering and rotational and vibrational excited water, respectively.

3.2.2. Example Trajectories

Before going to the details, example trajectories for each process leading to one of the four most stable adsorbed species, molecular adsorption, 1-2 dissociation, 1-4 dissociation and 1-4' dissociation are shown in Figure 3.6. The applied parameters are reported in the respective caption. These figures were all obtained from canonical calculations (NVT) at 300 K (see Figure 3.6, the trajectory shown in (d) was additionally preexcited in the asymmetric stretch mode leading to 1-4' dissociation). As one can see, molecular, 1-2 and 1-4 dissociated species can occur directly at the impact time of the water molecule at the surface and is henceforth called direct dissociation from the gas phase. For the 1-4' dissociation shown in Figure 3.6(d), this process does not happen directly at the impact but (in this case) ca. 40 fs later, so this

3. Water on $\alpha\text{-Al}_2\text{O}_3(0001)$

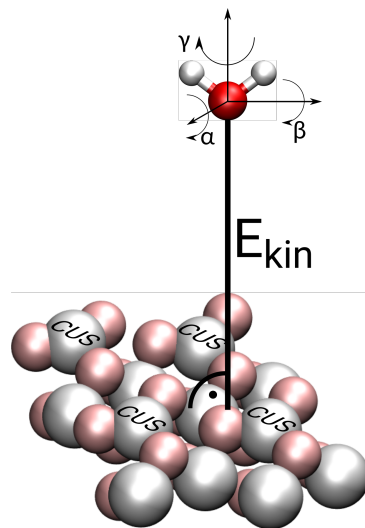


Figure 3.4.: Sketch for initial parameters of the trajectories. The water molecule's center of mass is situated 4 Å above the surface and is arranged within the shown coordinate system, before being impinged to the surface with a defined kinetic energy E_{kin} .

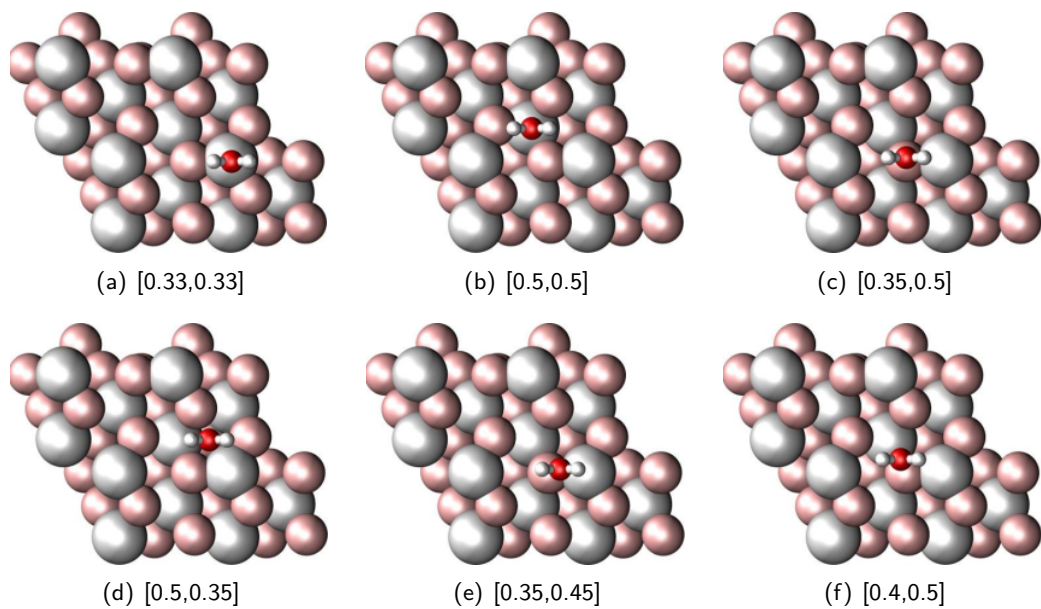
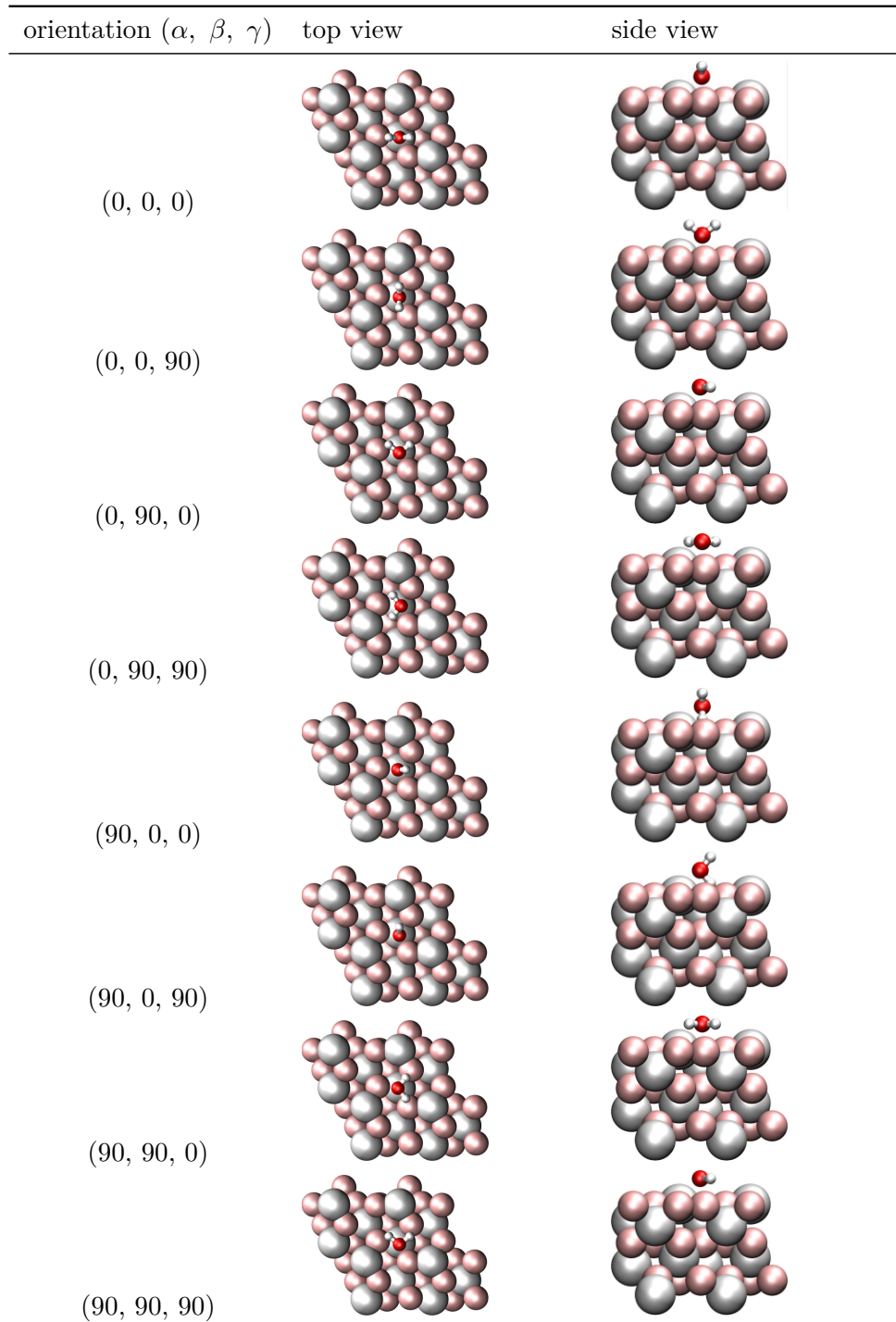


Figure 3.5.: The six impact points $[a_0, b_0]$ that were used in the AIMD calculations (shown for the rotational orientation $[0, 0, 0]$, topview). The different points reflect the most important sites of the surface, $[0.33, 0.33]$ is on top of an Al CUS, $[0.5, 0.5]$ on top of an Al in a subsurface layer. $[0.35, 0.5]$ is on top of a surface oxygen atom, whereas $[0.5, 0.35]$ is on top of a subsurface oxygen atom. $[0.35, 0.45]$ is in a gap between an Al CUS and a surface oxygen and $[0.4, 0.5]$ is in the gap between a surface O and a subsurface Al atom.

3.2. AIMD for MBS Process

Table 3.3.: Orientations of the water molecule, given in $^{\circ}$. Shown are both top view and side view at impact point 0.5,0.5. (look from the right-hand side to the top view)



3. Water on $\alpha\text{-Al}_2\text{O}_3(0001)$

is referred to as indirect dissociation with a molecular intermediate. This indirect process is not unique for the 1-4' dissociated species, all the other species including the molecular one can be observed to happen indirectly by either being reflected first from the surface before adsorbing/dissociating or by adsorbing molecularly before dissociating. However, the 1-4' species was the only one that could not be observed after direct dissociation.

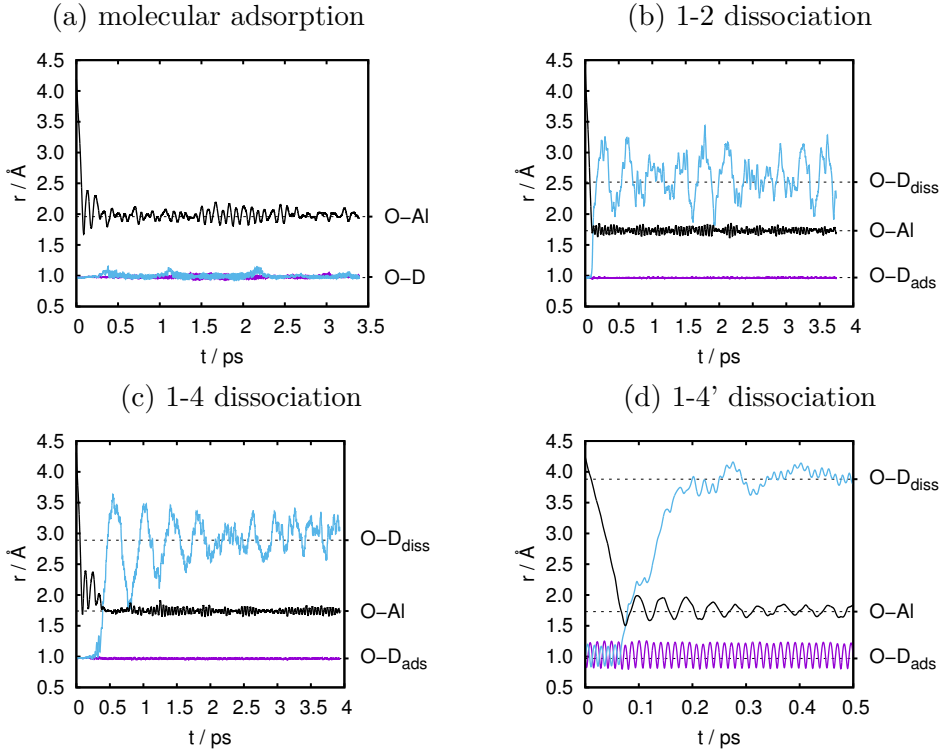


Figure 3.6.: The four adsorbed states of water, as shown in Figures 3.2(a)-(d) can be obtained in these exemplary trajectories. All of them are from canonical (NVT) trajectories at $T = 300\text{ K}$. The initial parameters: (a) $E_{\text{kin}} = 0.7\text{ eV}$, $[a_0, b_0] = [0.33, 0.33]$, $[\alpha, \beta, \gamma] = [0, 0, 90]$; (b) $E_{\text{kin}} = 0.7\text{ eV}$, $[a_0, b_0] = [0.35, 0.45]$, $[\alpha, \beta, \gamma] = [0, 0, 0]$; (c) $E_{\text{kin}} = 0.7\text{ eV}$, $[a_0, b_0] = [0.33, 0.33]$, $[\alpha, \beta, \gamma] = [0, 90, 0]$; (d) $E_{\text{kin}} = 0.7\text{ eV}$, $[a_0, b_0] = [0.35, 0.5]$, $[\alpha, \beta, \gamma] = [0, 0, 0]$. As specified in Subsection 3.2.6, for the latter the water molecule was vibrationally preexcited along the asymmetric stretch normal coordinate. The r values (y axis) corresponds to the bond lengths between water-O and the CUS Al atom on which either D_2O or the water hydroxyl unit OD adsorb (O-Al), the distance between water-O and D in non-dissociated (fragments of) D_2O (O-D or O-D_{ads}), and the distance between water-O and D in dissociated (fragments) of D_2O (O-D_{diss}), respectively. Also the interatomic distances of the minimum geometries are given as horizontal dashed lines. Panel (d) shows that the 1-4' state is not obtained directly but reached via a short-lived 1-2 dissociation intermediate.

3.2. AIMD for MBS Process

3.2.3. Microcanonical AIMD at clean surface

The effects of a single D₂O shot to the cool surface with an NVT ensemble (microcanonical AIMD, the 0 K optimized geometry of the surface had no initial momenta) were studied systematically by probing over three parameters: Five different kinetic energies (from 0.5 to 0.9 eV in 0.1 eV steps), six lateral impact points at the surface ([0.33,0.33], [0.5,0.5], [0.35,0.5], [0.5,0.35], [0.35,0.45], [0.4,0.5], see also Figure 3.5) and eight different orientations of the water with respect to the surface ([0,0,0], [0,0,90], [0,90,0], [0,90,90], [90,0,0], [90,0,90], [90,90,0], [90,90,90], see also Table 3.3). These $5 \times 6 \times 8 = 240$ AIMD trajectories for the clean surface at $T = 0$ K were carried out for ca. 1.2 ps each.

In the trajectories either molecular adsorption, 1-2 dissociation or reflection could be observed. Dissociation was assumed, if the OD distance was greater than 1.3 Å, but it was made sure that the results did not differ for a greater cutoff distance. Interestingly, only 1-2 dissociation and no 1-4 dissociation could be observed for the conditions (NVT, clean surface), although the molecular and the 1-4 dissociated species are almost equal in energy, and also the barrier heights ΔE^\ddagger for the dissociation to 1-2 (0.13 eV) and 1-4 (0.19 eV) do not differ largely (*cf.* Table 3.2). As it is shown later, other conditions are necessary for reaching 1-4 dissociation.

For a statistical analysis of the data see Figure 3.7, where the probabilities for reflection,

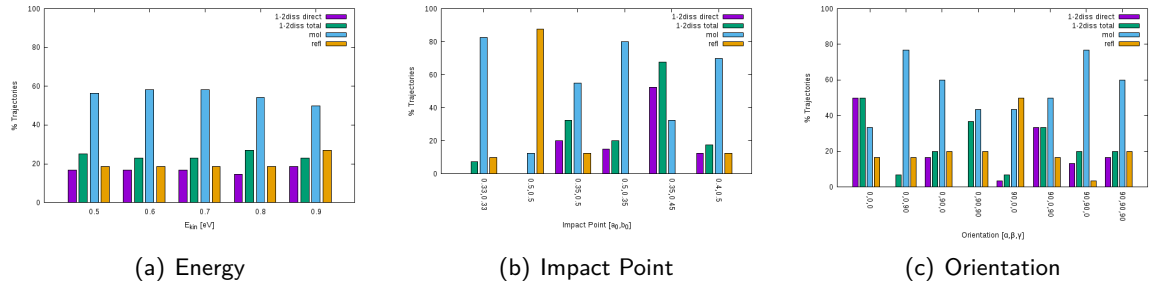


Figure 3.7.: Bar charts showing the statistics of NVE AIMD trajectories at 0 K for a single D₂O molecule approaching the clean alumina(0001) surface. (a) summarizes the findings for all kinetic energies E_{kin} averaged over $6 \times 8 = 48$ combinations of impact point and orientation. In (b), for all impact points $[a_0, b_0]$ is averaged over $5 \times 8 = 40$ combinations of kinetic energy and rotational orientation and (c) gives an overview over all orientational orientations $[\alpha, \beta, \gamma]$, averaged over $5 \times 6 = 30$ combinations of kinetic energy and impact points. The columns give percentages of the different outcomes - here labeled as “refl” reflection, “mol” molecular adsorption and direct and total 1-2 dissociation (“1-2 diss direct” and “1-2 diss total”). If one type of outcome did not occur, no column is shown.

molecular adsorption and 1-2 dissociation are shown as a function of the kinetic energy (a), impact point (b) and the orientation (c). It was distinguished between direct and indirect

3. Water on $\alpha\text{-Al}_2\text{O}_3(0001)$

dissociation. Admittedly, this analysis is restricted by the number of trajectories (240). From these figures and the data one can derive the following conclusions:

As anticipated, all three processes could be observed, reflection (20.4%, 49 of the 240 trajectories), molecular adsorption (55.4%, 133 trajectories) and 1-2 dissociation (24.2%, 58 trajectories). Probabilities for all outcomes can be found in the Appendix.

Looking at the influence of the kinetic energy in Figure 3.7(a), the results do not depend largely on the initial kinetic energy of the molecule, at least for the probed energy range. In all cases molecular adsorption dominates, followed by 1-2 dissociation and reflection, that are in the same range around 20-25%. This reflection probability P_{diss} is only increased for 0.9 eV, at the expense of the molecular species. To tackle the low energy regime, one additional trajectory of 0.1 eV was done ($[a_0, b_0] = [0.35, 0.45]$; $[\alpha, \beta, \gamma] = [0, 0, 0]$), for which $P_{\text{diss}} = 1$ for all energies ≥ 0.5 eV. In the case of $E_{\text{kin}} = 0.1$ eV, the trajectory only shows molecular adsorption. This result was rather surprising, since the kinetic energy plus the adsorption energy minus the barrier height is with $(0.1 + 1.31 - 0.13)$ eV = 0.28 eV larger than the reaction barrier. It seems that the excess energy is not available for the OD bond breaking and instead relaxes in other degrees of freedom of the system. That allows to draw the conclusion, that a minimum kinetic energy is necessary for the dissociation process. In the experiments of R. K. Campen, a kinetic energy of the beam between 0.6 and 0.75 eV is used. This minimum energy constraint can be one possible explanation of the difference between MBS and pinhole dosing. In the latter case, the only energy of a water molecule comes from the thermal energy that can be estimated for a D₂O molecule in the gas phase at 300 K to be around $\frac{3}{2}k_B T \approx 40$ meV.

In contrast to the kinetic energy, the lateral impact point at the surface has a great influence on adsorption and dissociation probabilities as can be seen in Figure 3.7(b). For the impact point [0.5, 0.5], that is at a non-surface Al position, 88% of the trajectories get reflected and molecular adsorption and 1-2 dissociation are oppressed, whereas for [0.33, 0.33], directly on top of an Al CUS position, 83% adsorb molecularly which dominates clearly over 1-2 dissociation. In contrast to both sites, [0.35, 0.45] which lies at a gap between the CUS position and a neighboring oxygen atom leads to a high dissociation probability of $P_{\text{diss}} \approx 68\%$ with a minor percentage of indirect dissociation. This high dissociation probability can be explained by the fact, that the molecule hits the surface already in a “product-like” geometry, so that the OD bond breakage is facilitated.

The initial rotational orientation has also an effect (cf. Figure 3.7(c)), although not so clearly as for the impact point dependence. This might be explained when looking at the trajectories in detail, so one can see, that the water molecule rotates due to the attractive and repulsive interaction with the surface atoms. That leads to a reorientation of the water molecule right before adsorbing, so that the initial orientation is not remembered by the system largely. The

3.2. AIMD for MBS Process

orientation of the molecule shortly before reaching the surface is more important, also here, if the molecule's orientation is already in a product-like state, the dissociation probability is elevated.

As can be seen from the data, direct dissociation dominates mostly over indirect dissociation, although it is dependent on the initial conditions, *e. g.* for the initial orientation [0,90,90] only indirect dissociation is observed.

3.2.4. Thermalized Surface

After getting an impression about the system with the microcanonical MD at the clean surface, as a next step the thermalized surface at 300 K is studied. For this the naked surface was preequilibrated at 300 K for 1 ps and the obtained geometry with the included velocities was used as an input to the following calculations. Here, only a kinetic energy of 0.7 eV was considered, since this energy is the closest to previous experiments by Campen and also the energy dependence was shown to be insignificant. The water molecule was then shot onto the equilibrated surface and the heat bath acted from the start on the water molecule. This is not huge a problem, since the molecule hits the surface quickly and thus hardly affects the dynamics.

First, for a selection of five parameter sets 100 NVT trajectories were calculated each at a temperature of 300 K. These parameter sets are

$$[a_0, b_0][\alpha, \beta, \gamma] = [0.35, 0.45], [0, 0, 0]; [0.35, 0.45], [0, 90, 90]; [0.35, 0, 45], [90, 90, 90]; [0.4, 0.5], [0, 0, 0]; [0.5, 0.35], [90, 0, 90].$$

These parameters led in the previous microcanonical ensemble to 1-2 dissociation and were chosen because the idea was that the thermal effects might trigger them to dissociate or diffuse to the 1-4 species. The duration of the trajectories was 1 ps and were done analogously as explained in Section 3.2.3 except for now the thermalized surface. All of these 500 trajectories dissociated 1-2, no reflection, molecular adsorption or further dissociation could be observed. As it seems, the thermal contribution is low, which was unexpected. The energy of the thermalized surface can be estimated by $N_s \times 3k_B T = 2.8 \text{ eV}$ (with $N_s = 36$ being the number of atoms in the surface slab that were allowed to relax/move). This energy is in the same range as the kinetic energy of the incoming water molecule ($\approx 2 \text{ eV}$). Indeed, this surface energy is not valid for the small surface range where the impact takes place, so that the thermal energy of the atom(s) of the impingement is considerably smaller.

As a next step, for all $6 \times 8 = 48$ combinations of parameters, but with the thermalized surface, were done for all six impact points and eight orientations presented in Section 3.2.3, but only for a kinetic energy of 0.7 eV. For each of the sets, two trajectories of 4 ps duration were

3. Water on $\alpha\text{-Al}_2\text{O}_3(0001)$

calculated. This restriction is due to high computational costs and gives rise to only a limited statistical significance. The long duration accounts for processes that occur later after the impact, that could have been missed by shorter trajectories. In Table 3.4, the probabilities for each process is shown, in comparison with the previous microcanonical AIMD trajectories. Because six of the trajectories aborted due to numerical reasons, here only 42 trajectories can be evaluated and the comparison is, of course, done only with the corresponding microcanonical trajectories. In the first line of the table, the results for the complete probed space for the

Table 3.4.: Statistical results for NVE (both upper lines) and NVT trajectory at 300 K (lower line).

The models differ only by the thermalized surface, for all trajectories a single D_2O was sent on a clean surface with a kinetic energy of $E_{\text{kin}} = 0.7 \text{ eV}$. The initial parameters were the 48 and selected 42 from Section 3.2.3, respectively, as explained in the text.

| ensemble | no. of trajectories | P_{refl} | P_{mol} | $P_{\text{diss}} (1\text{-}2)$ | $P_{\text{diss}} (1\text{-}4)$ |
|--------------------|---------------------|-------------------|------------------|--------------------------------|--------------------------------|
| NVE ¹ | 48 | 0.19 | 0.58 | 0.23 | 0.00 |
| NVE ^{1,3} | 42 | 0.19 | 0.55 | 0.26 | 0.00 |
| NVT ² | 42×2 | 0.12 | 0.54 | 0.24 | 0.11 |

¹ Propagation time 1.22 ps. ² Propagation time 4 ps. ³ A subset of the NVE/48 data set, corresponding to the same initial impact parameters as used for the NVT ensembles.

NVE ($T=0$) is shown, the second line gives the results for the corresponding 42 microcanonical trajectories and in the third line, the canonical results for 42 NVT trajectories ($T = 300 \text{ K}$) are given. For all, the kinetic energy is $E_{\text{kin}} = 0.7 \text{ eV}$. In contrast to the microcanonical MD, the canonical yields 1-4 dissociation at a percentage of around 11% and gives slight decreases in the reflection, whereas molecular adsorption and 1-2 dissociation almost remain constant. From the 1-4 dissociated trajectories, 44% dissociated directly and 56% indirectly after initial molecular adsorption. Interestingly, all initial conditions in the trajectories that show 1-4 dissociation in the NVT led only to molecular adsorption in the NVE AIMD. The idea supposed earlier emanated that 1-4 dissociation from trajectories that gave 1-2 dissociation in NVE, but apparently the molecular species plays a more important role.

Note, that the surface temperature indeed has an effect on the probabilities for the different processes and also 1-4 dissociation could be observed. As before, the first impact can lead to reflection and in a “bouncing” process, the molecule can also adsorb after another impact, in few cases also on another CUS atom as the initial impact was on.

3.2.5. Refined Surface Model

In the experiment, after a certain time, the coverage will be higher, which will have an impact on the incoming molecule. To account for this a preadsorbed surface model was applied, where

3.2. AIMD for MBS Process

the minimum structure of the surface with a single adsorbed water molecule was used and a second D₂O was sent onto this surface. For the preadsorbed water, the three minima were assumed: (a) the molecular minimum, (b) the 1-2 dissociated species and (c) the less stable 1-4 dissociated water. The preadsorbed OD/D₂O was adsorbed at the position [0.33,0.33], in the lower right 1 × 1 sub cell of the supercell in Figure 3.2(a)-(c), that is located around the CUS atom at this lateral impact point.

For the incoming second water molecule with an initial kinetic energy of 0.7 eV, one has to distinguish between two cases: The impact points $[a_0, b_0]$ were chosen such that (i) the second water molecule is shot in the same 1 × 1 sub cell where the preadsorbed water is adsorbed (the lower right part of the supercell) and (ii) in another sub cell, here, the lower left part. Once again, various initial orientations and impact points were probed for a propagation time of 1 ps.

First, NVE (microcanonical, $T = 0\text{ K}$ of the initial surface) were done. (i) In the first case, the incoming water is shot to the direct vicinity (same sub cell) of the preadsorbed molecular water, the second *incoming* D₂O is observed to be either reflected or adsorb molecularly at another CUS atom after initial reflection from the preadsorbed water molecule. In the case of molecular preadsorbed water, the impact of the second molecule can make the molecular *preadsorbed* water dissociate to 1-2, 1-4 and even 1-4'. Assumingly, part of the energy is not used to overcome the barrier to diffusion/dissociation but to interaction with the preadsorbed molecular species. However, this does not happen for the 1-2 and the 1-4 *preadsorbed* species; only in one case 1-4 reacts to the molecular adsorbed species. As can be seen in Table 3.5, there is a difference between impact points direct on the CUS atom [0.33, 0.33] and the impact position next to the CUS position [0.35, 0.45]. Additional data is shown in the Appendix, Section D.

Considering the impact point [0.33,0.33] of the incoming water, exactly where the preadsorbed water is located, one can see either reflection (R) or molecular adsorption after diffusion to another CUS site (M in Table 3.5).

In contrast to that, an impact point near the CUS atom, [0.35,0.45], gives rise to a greater number of different outcomes. In the case of the molecular preadsorbed species, molecular adsorption on a neighboring CUS and physisorption above the preadsorbed molecular species (*i.e.* the molecule is not bound directly to a CUS atom but to water (fragments) via hydrogen bonds) can be observed, which leads to the conclusion, that clustering occurs at the surface. For the 1-2 dissociated preadsorbed system, also 1-2 dissociation on a neighboring CUS can be discovered. The 1-4 dissociated preadsorbed species gives in addition to molecular adsorption and physisorption also reflection. If the preadsorbed species is dissociated, molecular adsorption is clearly favored, followed by physisorption.

3. Water on $\alpha\text{-Al}_2\text{O}_3(0001)$

Table 3.5.: Selected results of preadsorbed surface trajectories for the microcanonical ensemble (NVT , $T = 0\text{ K}$, $E_{\text{kin}} = 0.7\text{ eV}$). The three relevant cases are: molecular, 1-2 and 1-4 dissociated preadsorption. R=reflection, M=molecular adsorption (chemisorption), P=molecular physisorption, D(1-2)=1-2 dissociation, D(1-4)=1-4 dissociation. The two letters for each cell give the outcomes for the *incoming* molecule (first entry) and the *preatsorbed* water (second entry). For the case that the preadsorbed species changed its character, a * is attached. “term.” refers to terminated trajectories. Missing entries mean that no calculation was done.

| orientation [α, β, γ] | type of preadsorption | | | | | |
|--|---|---|---|---|-----------|--|
| | molecular | | 1-2 dissociated | | | |
| | impact position [a_0, b_0] [0.33,0.33] | impact position [a_0, b_0] [0.35,0.45] | impact position [a_0, b_0] [0.33,0.33] | impact position [a_0, b_0] [0.35,0.45] | | |
| [0, 0, 0] | M, D(1-2)* | P, D(1-2)* | | M, D(1-2) | R, D(1-4) | |
| [0, 0, 90] | | M, D(1-2)* | | M, D(1-2) | P, D(1-4) | |
| [0, 90, 0] | | P, D(1-4)* | R, D(1-2) | M, D(1-2) | R, D(1-4) | |
| [0, 90, 90] | | P, D(1-4')* | | M, D(1-2) | term. | |
| [90, 0, 0] | | P, D(1-2)* | | M, D(1-2) | M, D(1-4) | |
| [90, 0, 90] | | P, M | | D(1-2), D(1-2) | P, D(1-4) | |
| [90, 90, 0] | | P, D(1-4)* | | M, D(1-2) | R, D(1-4) | |
| [90, 90, 90] | | M, D(1-2)* | R, D(1-2) | M, D(1-2) | M, D(1-4) | |
| | | P, D(1-4)* | | M, D(1-2) | P, D(1-4) | |

Looking at the preadsorbed species, the molecular species is mostly affected by the incoming molecule by showing dissociation to all dissociated states (1-2, 1-4 and also 1-4'), whereas the 1-2 dissociated preadsorbed species is not influenced at all. Only for one of the 1-4 preadsorbed trajectories, a change of the state is observed, to a molecular species via proton transfer from the incoming water molecule.

(ii) In the second case, a neighboring sub cell (the lower left one) is the aim of the molecular beam, where no water is preadsorbed. The preadsorbed water or water fragments are hardly disturbed by the incoming D_2O , due to the great distance of the residues. Only a single trajectory out of 36 changed its character: the molecularly preadsorbed species exchanged a proton with the neighboring 1-2 dissociated incoming species after the impact and therefore dissociated.

Surprisingly, the incoming molecule is affected by the preadsorbed species in the way that the dissociation probability is increased and 1-4 dissociation occurs, in contrast to comparable previous microcanonical with a clean surface: Mostly molecular adsorption ($P_{\text{mol}}=0.47$), dissociation ($P_{1-2}=0.22$ and $P_{1-4}=0.14$), physisorption ($P_{\text{phys}}=0.11$) take place. Reflection is drastically decreased ($P_{\text{refl}}=0.06$). Respective values for microcanonical MD of the clean surface are $P_{\text{mol}}=0.58$, $P_{1-2}=0.23$, $P_{1-4}=0$, $P_{\text{phys}}=0$ and $P_{\text{refl}}=0.19$. Although the statistics may not be sufficient, the reduced probability of reflection can be interpreted with attractive inter-

3.2. AIMD for MBS Process

action of both the incoming and the preadsorbed molecule and leads to a higher probability of dissociation.

Summarizing these findings, one can say, that the preadsorbed enhancement of the system leads to further outcomes of the scattering as physisorption/clustering on the surface and the so far unreached 1-4 and 1-4' species, the latter by dissociation of preadsorbed molecular water. As it is not surprising, the influence is more massive with the incoming water molecule being near the preadsorbed species.

In analogy to these NVE trajectories, canonical (NVT, with $T = 300\text{ K}$) trajectories with the preadsorbed systems were done. As before (Section 3.2.4), as a starting point the preequilibrated structures of molecular adsorption, 1-2 and 1-4 dissociation were used, that have been equilibrated at 300 K for 1 ps. The following trajectories including the 0.7 eV water “beam” were run for 1 ps. As for the respective microcanonical trajectories, one has to distinguish between the water aiming at (i) the same sub cell (lower right) and (ii) the neighboring sub cell (lower left 1×1 sub cell). The results do not differ largely in comparison to the NVE ensemble, but some probabilities are altered. For case (i) in comparison with the microcanonical preadsorbed surface one can see that only physisorption is enhanced, whereas the other processes (molecular adsorption, 1-2, 1-4 dissociation and reflection) are suppressed. In the case of the water hitting the neighboring subcell (ii) similar effects can be seen, although here molecular adsorption is favored and the other processes (1-4 dissociation, physisorption and reflection) are reduced. 1-2 dissociation happens with almost the same amount as in the NVE ensemble. Also concerning the preadsorbed water (fragment) there are changes, especially for the molecular preadsorbed species in case (i): Only in four out of 24 cases the character of the preadsorbed water changes. For the case of molecular preadsorption and the neighboring CUS, there is an increase in the molecular adsorption ($P_{1-2}=0.34$ instead of 0.23 for microcanonical) leading to the conclusion, that the influence of the preadsorbed species is high despite the distance so that the non-locality of the process is enhanced. For further probabilities see Appendix.

3.2.6. Refined Beam Model

Enhancing the beam is a further refinement and is done here in two different ways: assuming a water cluster as the approaching species and as a second improving method exciting the water molecule rotationally, vibrationally and with a combination of both.

Clustering

As a cluster, the $(\text{D}_2\text{O})_4$ system was optimized in the same periodic boundary conditions as the cell before but without the surface, for geometry see Figure 3.8. The same cluster was already

3. Water on $\alpha\text{-Al}_2\text{O}_3(0001)$

shown to be the most stable one by Wales et al. [65], there it is called “up-down-up-down”. This cluster was then fired with a kinetic energy of 0.9 eV at the cold clean surface (NVE) from a distance of 4 Å (distance to the center of mass of the cluster) above the Al surface layer, with a duration of around 1.22 ps. Once again, several impact points (again defined for the center of mass position) and orientations of the cluster were considered. These orientations were applied analogously to the previous ones with the axes of the rotations shown in Figure 3.8(b).

Evaluating the data shows that the cluster breaks up upon contact with the surface into

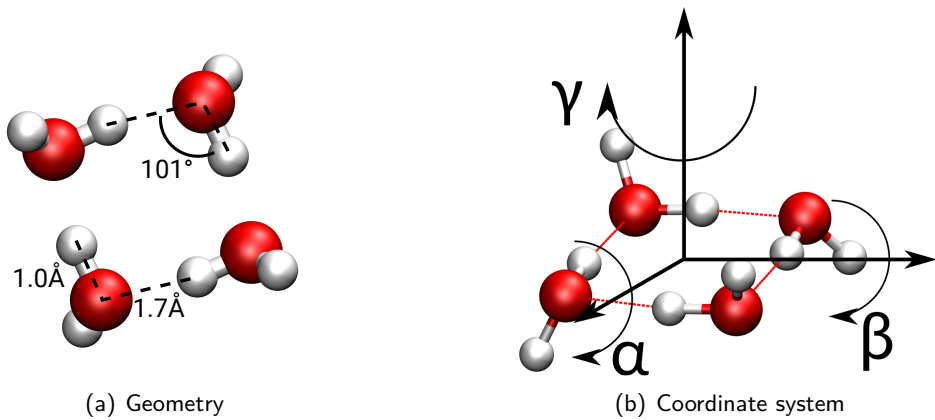


Figure 3.8.: (D_2O)₄ cluster for simulation of effects of higher coverages. (a) shows the optimized geometry, especially the DOD bond angle and the OD bond lengths and (b) shows the coordinate system for the rotations along the axes with the angles α , β and γ .

individual D_2O molecules and these undergo different processes, to a great extent influenced by the surrounding water molecules, due to the high coverage of 1 ML (the 2×2 supercell with its four CUS positions can hold up to four water molecules in one mono layer). The water can adsorb molecularly or dissociatively (both directly and indirectly), physisorb, deuterium atoms can diffuse or single molecules can be reflected totally. Two examples of the final geometries can be found in Figure 3.9.

Mostly independent of the settings, the molecules interact strongly with each other showing a profoundly dynamic behavior. This gives rise to processes that were not possible for the clean surface NVE and a single water situation, where no 1-4 dissociation nor physisorption were observed. Of course, the probabilities for dissociation, molecular adsorption and reflection are different, the probability of molecular adsorption is strongly diminished to the advance of 1-2, 1-4 and 1-4' dissociation and physisorption. For details see Appendix.

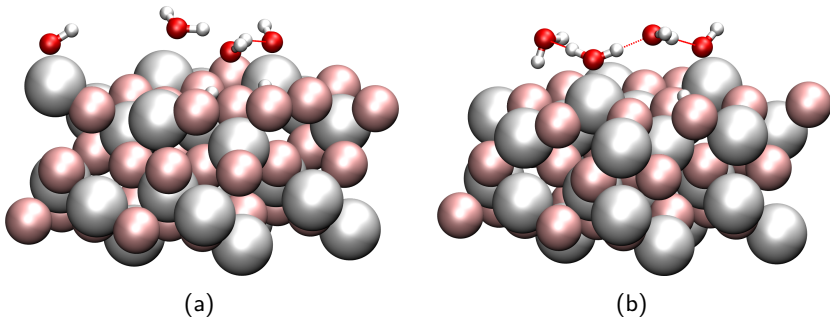


Figure 3.9.: Side views of the last time step (1.22 ps) for two initial conditions: (a) $E_{\text{kin}} = 0.9 \text{ eV}$, $[a_0, b_0] = [0.5, 0.35]$, and $[\alpha, \beta, \gamma] = [0, 0, 0]$ and (b) $E_{\text{kin}} = 0.9 \text{ eV}$, $[a_0, b_0] = [0.35, 0.5]$, and $[\alpha, \beta, \gamma] = [90, 90, 0]$. Hydrogen bonds are shown as red dashed lines. Physisorption, molecular adsorption and dissociation can be seen in both snapshots.

Rotationally and vibrationally preexcited Water

Here, qualitative results are given for a D_2O molecule that is at the beginning of the trajectory not rigid as before but excited rotationally and/or vibrationally. It is shot with a kinetic energy of 0.7 eV at the clean surface in an NVE ensemble for a trajectory duration of 2 ps at the impact point $[0.35, 0.5]$ with the initial orientation $[0, 0, 0]$. With these applied conditions in the rigid case (microcanonical at 0 K without rotational or vibrational excitation), the molecule dissociates to the 1-2 structure, the same for the thermalized surface at $T = 300 \text{ K}$.

The vibrational excitations were chosen as follows: For the single water molecule in the periodic boundary conditions a normal mode analysis was done. The eigenvectors of the dynamical matrix for the symmetric stretch, asymmetric stretch and the bending mode were used: The eigenvectors of the dynamical matrix equal normal mode displacements. They were scaled by a factor of 0.1 and these positions were used as initial positions for the dynamics. This corresponds to an atom displacement along normal modes out of the equilibrium position, *i.e.*, a vibrational excitation. It was used as an input for the MD trajectories in addition to the initial momentum towards the surface. For the rotational preexcitations along the three axes, D atoms were given initial momenta to induce a rotational motion corresponding to rotational energies of $\sim 0.2 \text{ eV}$.

The results for the rotation around the γ -axis (*cp.* Figure 3.4) shows molecular adsorption whereas rotations around the other two axes give 1-2 dissociation as in the initial microcanonical trajectories without rotational excitation. In the cases of vibrational preexcitation, the symmetric stretch leads to reflection, the asymmetric stretch gives 1-4' dissociation after initial 1-2 dissociation (as was already addressed in Figure 3.6) and with the bending mode being excited, the water dissociates to 1-2. Also, a small collection of combinations of vibrations

3. Water on $\alpha\text{-Al}_2\text{O}_3(0001)$

with rotations were calculated, that lead to either molecular adsorption (rotation around α and bending mode), or 1-2 dissociation (rotation around γ and asymmetric stretch; and rotation around β and symmetric stretch).

Quantitatively, the results may depend strongly on the excitation energy, that was not of concern here, one can say, that preexcitation has an effect on the dynamics of the water adsorption and dissociation, respectively, that were not possible with the rigid water molecule.

Although a large number of trajectories were done with the contingent at the HLRN facility a reliable statistics could not be achieved. It was only computationally feasible to do trajectories with 1 to 4 ps duration. Also only a limited set of degrees of freedom could be probed, *e.g.* the angle of the beam with respect to the surface was no other than 90° and initial orientations were only probed in 90° steps. Apart from that, no quantum effects were considered. Still these results show very well the effect of enhanced dissociation probability, how clustering occurs, the influence of elevated temperature and rotations and vibrations [64].

3.3. Improvement of Reaction Rates

For a model reaction we try to improve the reaction rate of a specific chosen reaction with a higher level method. This reaction is a H-diffusion reaction on the (0001) surface studied before in our group, the Df-H-4-2 reaction [52], that moves a proton in the 1-4 position to the OH residue to the 1-2 dissociated state (see Figure 3.10). The transition state was calculated

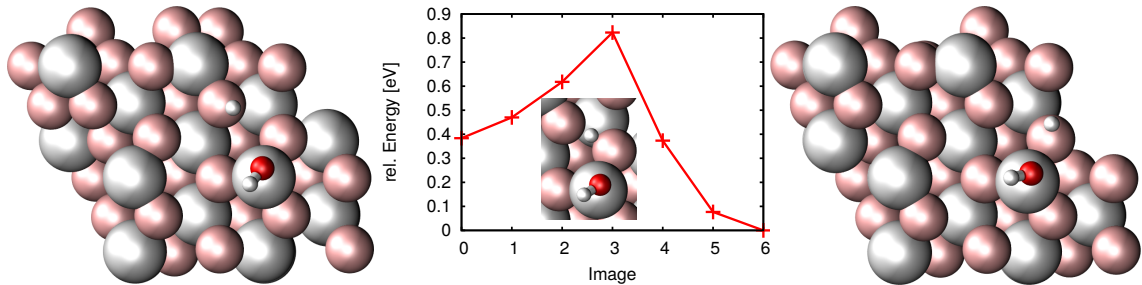


Figure 3.10.: Reaction path of the Df-H-4-2 proton diffusion reaction in the PBE-D2 level of theory, left is the educt (1-4), in the middle the minimum energy path with the transition state geometry as an inlay and on the right the product (1-2) of the reaction. *Data with friendly permission by Jonas Wirth.*

with PBE+D2 with the implementation of nudged elastic band in VASP. Rates were calculated via Eyring (Equation (1.28)). A further previous approach were single point calculations at the HSE level of theory (hybrid functional) on top of PBE optimized geometries were done for the minima and the transition state is presented. Additionally, for this process a 1-D potential energy surface was calculated and then the Schrödinger equation was solved to obtain the wave function and see the localization/delocalization of the reaction pathway. These results are summarized in Table 3.6.

Table 3.6.: PW91, PBE+D2 after geometry optimization and transition state via NEB, HSE single point calculations on top of PBE optimized geometries. Both were calculated from Eyring equation (1.28). The exact tunneling was calculated from a 1-D potential and the calculation of the Schrödinger equation in this potential. These calculations were done by Dr. J. Wirth and are partially unpublished.

| Method | k [s^{-1}] |
|------------------------|--------------------|
| PW91 | 1.97×10^8 |
| PBE | 9.15×10^7 |
| HSE | 3.15×10^7 |
| “exact” tunneling (1D) | 6.49×10^8 |

It is now a goal to expand these methods to the following: By first calculating the adsorption

3. Water on $\alpha\text{-Al}_2\text{O}_3(0001)$

energies and the barrier within a atom centered orbital method with the hybrid functional B3LYP and also going beyond density functional theory and going to perturbation theory (local Möller-Plesset perturbation theory of second order, LMP2). After this, the transition state shall be reoptimized with B3LYP and the respective rates shall be calculated for this geometry both with density functional theory (PBE and B3LYP) and MP2.

Adsorption Energies

Going beyond pure density functionals and also beyond DFT has been too costly for a long time, simply not applicable for surface adsorbat system that large and electron rich. In the Crystal14 [45] and cryscor [46] code atom centered bases are used instead of plane waves so that large scale systems can also be computed. With this it is possible to calculate periodic HFTODO: *mention this?*, PBE, B3LYP and even MP2.

In Table 3.7 the adsorption energy results of previous VASP calculations with different methods (PBE and PW91) and dispersion corrections are shown. The adsorption energy is calculated according to Equation (2.1).

Table 3.7.: Adsorption energies of the three adsorption states of the 0001 surface site with VASP, i.e. periodic DFT calculations with a plane wave basis. Values are given in eV. The 1-4' system was not calculated with PW91 [52]. *mention 1-4' results?*

| method | mol | 1-2 diss | 1-4 diss | 1-4' diss |
|---------|-------|----------|----------|-----------|
| PW91 | -1.25 | -1.59 | -1.25 | - |
| PW91+D2 | -1.40 | -1.81 | -1.45 | - |
| PBE+D3 | -1.29 | -1.63 | -1.30 | -1.25 |

The adsorption energy is in favor of the 1-2 dissociated species for all methods, and dependent on dispersion corrections, the molecular and 1-4 dissociated are equal (PW91, PBE+D3) or is slightly more stable (PW91+D2).

In the Crystal code, several basis sets for each atom are available, it is necessary to utilize some basis sets and compare the results to former VASP calculations. The basis sets that were tested are summarized in Table 3.8.

This was first done for PBE, the same functional that was used for the VASP calculations. The geometries of H_2O , the clean surface and the three adsorbed species (mol, 1-2 and 1-4) were geometry optimized. The corresponding adsorption energies can be found in Table 3.9. In contrast to the VASP calculations all basis sets that were tested predict the stability order $1\text{-}2 > \text{mol} > 1\text{-}4$, whereas VASP depending on the dispersion corrections gives $1\text{-}2 > 1\text{-}4 \geq \text{mol}$.

3.3. Improvement of Reaction Rates

Table 3.8.: Basis set overview for Al, O and H in the Crystal14 calculations.

| basis set | Al | O | H |
|-----------|------------------------------|--------------------------|-----------------|
| 1 | Al_s8511p511d11_Heifets_2013 | O_8411(d11)_Heifets_2013 | H_pob_TZVP_2012 |
| 2 | Al_pob_TZVP_2012 | O_pob_TZVP_2012 | H_pob_TZVP_2012 |
| 3 | Al_m-6-311G(d)_Heyd_2005 | O_m-6-311G(d)_Heyd_2005 | H_pob_TZVP_2012 |
| 4 | Al_85-11G*_catti_1994 | O_m-6-311G(d)_Heyd_2005 | H_pob_TZVP_2012 |
| 5 | Al_86-21G*_harrison_1993 | O_pob_TZVP_2012 | H_pob_TZVP_2012 |
| 6 | Al_85-11G*_catti_1994 | O_pob_TZVP_2012 | H_pob_TZVP_2012 |
| 7 | Al_86-21G*_harrison_1993 | O_m-6-311G(d)_Heyd_2005 | H_pob_TZVP_2012 |

Table 3.9.: Adsorption energies from Equation (1.28) of the three adsorption states of the (0001) surface site (PBE+D3, geometry optimizations were done with the respective basis set from Table 3.8). All values are given in eV.

| basis set | mol | 1-2 diss | 1-4 diss |
|-----------|-------|----------|----------|
| 1 | -1.57 | -1.77 | -1.38 |
| 2 | -1.47 | -1.69 | -1.35 |
| 3 | -1.72 | -1.96 | -1.59 |
| 4 | -1.87 | -2.11 | -1.75 |
| 5 | -1.58 | -1.73 | -1.40 |
| 6 | -1.53 | -1.78 | -1.43 |
| 7 | -1.74 | -1.96 | -1.58 |

In addition, for basis set 1, adsorption energies were calculated with the VASP optimized structure (*i. e.* single point calculation with Crystal) to compare to VASP results. Those results are given in Table 3.10. Both crystal results (reoptimized and VASP optimized geometry) give

Table 3.10.: Adsorption energies of the four adsorption states of the 0001 surface site (PBE+D3 with basis set 1 (see Table 3.8)). Values are given in eV. VASP values are reoptimized from J. Wirth's work with PBE+D3.

| | mol | 1-2 diss | 1-4 diss |
|------------------|-------|----------|----------|
| crystal (opt) | -1.57 | 1.77 | -1.38 |
| crystal (no opt) | -1.67 | -1.87 | -1.52 |
| VASP | -1.29 | -1.63 | -1.30 |

qualitatively the same ordering of the stability (mol is more stable than 1-4), which is different to former VASP results, although quantitative differences exist. Interestingly, the reoptimized system seems more stable due to different amounts of stabilization in the clean surface, the adsorbed system and the water molecule.

3. Water on $\alpha\text{-Al}_2\text{O}_3(0001)$

Going beyond PBE (GGA functional), the hybrid functional B3LYP including D3 dispersion corrections was applied. Geometry optimizations were done and adsorption energies were examined, see Table 3.11.

Table 3.11.: Adsorption energies of the three adsorption states of the (0001) surface site (B3LYP+D3; geometry optimization). Values are given in eV. Basis sets 5 and 6 give similar results as VASP and are highlighted with bold numbers.

| basis set | mol | 1-2 diss | 1-4 diss |
|-----------|--------------|----------|--------------|
| 1 | -1.56 | -1.88 | -1.45 |
| 2 | -1.57 | -1.92 | -1.53 |
| 3 | -1.78 | -2.15 | -1.68 |
| 4 | -1.90 | -2.25 | -1.83 |
| 5 | -1.57 | -1.95 | -1.57 |
| 6 | -1.62 | -2.01 | -1.62 |
| 7 | -1.80 | -2.14 | -1.69 |

Most basis sets also give the same ordering as PBE+D3, but basis 5 and 6 qualitatively give the same results as VASP (mol = 1-4 diss, like PW91 and PBE+D3) and also basis set 2 is very close to this.

One basic problem, that does not occur in the plane wave based periodic calculations is the so called basis set superposition error (BSSE). This error is due to overlapping basis functions from different atom centers, leading to an overstabilization of the system. To overcome this, one can apply counterpoise corrections (CP) or alternatively use a larger basis. For CP the parts of the system are treated individually and also with so called ghost basis and ghost atoms. This means a calculation for the water with a “ghost surface”, where the water molecule is treated normally and the surface consists of atom orbitals but with no charge, so that the electrons of water can occupy them. On the other hand a similar calculation with the surface and a “ghost water molecule” (or OH and H residues, respectively) has to be done. Since the structure of the dissociated species, especially for the 1-4 dissociated water with a greater OH-H distance, does not have to be stable without the surface or with a ghosted surface, it is unclear whether these calculations will converge.

To apply this scheme, four further calculations are required:

- a) the water in the adsorbed geometry plus the surface made from ghost atoms
- b) the surface in the adsorbed geometry plus the ghost water molecule
- c) the water in the adsorbed geometry but without surface

3.3. Improvement of Reaction Rates

d) the surface in the adsorbed geometry but without the water.

Then the BSSE-corrected energy can be calculated as:

$$E_{\text{water-surface}} - E(a) - E(b) + E(c) + E(d) - E_{\text{relaxed water molecule}} - E_{\text{relaxed surface}} . \quad (3.1)$$

The BSSE itself would then be:

$$E(a) + E(b) - E(c) - E(d) . \quad (3.2)$$

The adsorbate-surface interaction energy (stabilizing) is:

$$E_{\text{water-surface}} - E(a) - E(b) , \quad (3.3)$$

and the relaxation energy (which is anti stabilizing) is:

$$E(c) + E(d) - E_{\text{relaxed water molecule}} - E_{\text{relaxed surface}} . \quad (3.4)$$

When one applies this to the adsorbed systems with basis set 5, the following results can be obtained, see Table 3.12.

Table 3.12.: BSSE-corrected energy, BSSE, adsorbate-surface interaction energy and relaxation energy according to Equations (3.1)-(3.4) for mol, 1-2 diss and 1-4 diss with PBE+D3 using basis set 5. Values are given in eV.

| | mol | 1-2 diss | 1-4 diss |
|-----------------------|-------------|------------|----------|
| BSSE-corr. E. | -1.4276409 | -4.4848569 | - |
| BSSE | -0.14208315 | 2.7554316 | - |
| Ads-surf interact. E. | -1.4689164 | -9.4423711 | - |
| Relax. Energy | 0.04127551 | 12.197803 | - |

As assumed before, the 1-4 structure did not converge, because of missing stability in the ghosted calculations. The OH and H residues that are in that case far apart are not stabilized from the ghosted surface (without the real surface). In fact, also the 1-2 dissociated structure without the surface is an unphysical system and therefore it is questionable whether these results are reliable.

3. Water on $\alpha\text{-Al}_2\text{O}_3(0001)$

At least for molecular water one can evaluate the BSSE. For this basis set and geometry it is around 10% of the interaction energy. It is not much but it is of the order of the difference between the mol and 1-4 diss. On the other hand it is likely that in 1-4 diss the BSSE is of similar magnitude and the difference between the two adsorption geometries will remain. From the results also follows that the relaxation energy is rather small, at least for the case of molecular adsorption (it is not sure whether the 1-2 results can be trusted).

Since it was not possible to calculate the BSSE and respective relaxation and interaction energies for the 1-4 dissociated system, it is necessary to go on using an extended basis instead, to get (hopefully) the same effect as with CP corrections. This larger basis set is, here, a triple zeta basis set with high angular momentum. As before, geometry optimizations were done and the adsorption energies were evaluated, as can be seen in Table 3.13.

Table 3.13.: Adsorption energies for the high angular momentum basis set for the method given in the first column. All values are given in eV.

| | mol | 1-2 diss | 1-4 diss |
|----------------|-------|----------|----------|
| HF* | -1.14 | -1.67 | -1.19 |
| PBE+D3 | -1.41 | -1.68 | -1.32 |
| B3LYP+D3 | -1.43 | -1.81 | -1.40 |
| MP2* (dual) | -1.31 | -1.61 | -1.18 |
| MP2* (no dual) | -1.34 | -1.69 | -1.26 |

* Results will be shown and explained in the next paragraph.

PBE+D3 with the new basis set gives the same ordering as all other basis sets that were applied. The results are very close to the ones with basis set 2 from Table 3.9. For B3LYP+D3, the same order of stability is achieved, although there is only a small difference of 0.3 eV between mol and 1-4. Here, the results from the large basis are close to basis sets 1 and 2. To go beyond density functional theory, first HF and on top of this MP2 calculations were done. The HF calculations were carried out as singlepoint calculations with the optimized geometries from B3LYP calculations with the biggest basis set applied. The resulting adsorption energies can be found in Table 3.14.

Table 3.14.: Adsorption energies for HF with the high angular momentum basis set (single point calculations on top of B3LYP/high angular momentum basis set). All values are given in eV.

| mol | 1-2 diss | 1-4 diss |
|-------|----------|----------|
| -1.14 | -1.67 | -1.19 |

3.3. Improvement of Reaction Rates

With these calculations done, first a localization of the orbitals was done. Optional, at this point a dual basis expansion can be done, to increase the basis even further (this was done for Al and O), so that a basis set of the size of approximately augmented triple zeta can be achieved. For this one step of a HF calculation was done. These two results are compared in Table 3.15. It is visible that there is indeed a difference in stability with and without the dual basis set. Especially the 1-2 diss gets stabilized but also the 1-4 dissociated structure gains stability, compared to the molecular minimum, that is predicted to be equal by both methods.

Table 3.15.: MP2 adsorption energies of the three adsorption states of the (0001) surface site. Values are given in eV for the high angular momentum basis set. The upper part with the dual basis set and the lower without the corresponding dual basis set expansion.

| | mol | 1-2 diss | 1-4 diss |
|--------------------|-------|----------|----------|
| with dual basis | -1.31 | -1.61 | -1.17 |
| without dual basis | -1.34 | -1.69 | -1.26 |

The results of MP2 (both with and without dual basis set expansion) are compared to DFT results with PBE+D3 and B3LYP+D3 in Table 3.13. Here the overall trend for DFT that mol is more stable than 1-4 diss is confirmed by the dual basis set expanded MP2 calculation, but without this expansion, MP2 gives both geometries an almost degenerate energy. As in all previous calculations, 1-2 dissociation is shown to be the most stable adsorbed species.

Reaction Rate

For the reaction Df-H-4-2 introduced earlier shown in Figure 3.10, a transition state with a corresponding rate were recalculated with B3LYP+D3 and basis set 5, since GGA (*e. g.* the functional PBE) is known to underestimate barriers [40], so going beyond GGA is vital. Previous results with PBE and PW91 as well as hybrid functional results (single point calculations on top of PBE geometries) are shown in Table 3.6.

A transition state optimization was done, but this failed to converge. However, one point of the optimization showed only a small energy change in the micro Hartree region ($\approx 10^{-5}$ eV), atom displacements were tiny and the gradient was not too large either, so that this structure was examined further. A normal mode analysis showed one single imaginary frequency, as expected for a transition state of first order. Now from this geometry, PBE and MP2 energies were computed, to calculate a rate with the Eyring equation (1.28). These results for B3LYP, PBE and MP2 are shown in Table 3.16 *TODO: Table dE, dG and k(300K) for crystal reoptimized geometry.*

3. Water on $\alpha\text{-Al}_2\text{O}_3(0001)$

Table 3.16.: ΔE , $\Delta G(300\text{ K})$ in eV and $k_{300\text{K}}$ in s^{-1} for the reoptimized reaction Df-H-4-2 with B3LYP+D3 with crystal.

| | B3LYP (reopt) | B3LYP(no opt) | VASP |
|------------|---------------|---------------|-------------------|
| ΔE | | | 0.44 |
| ΔG | | | 0.29 |
| k | | | 9.1×10^7 |

Since this obtained transition state geometry was not converged properly, also calculations with PBE, B3LYP and MP2 at the VASP optimized transition state geometry were done and corresponding outcomes are presented in Table 3.16 *TODO: Table with dE , dG and $k(300\text{K})$ for vasp optimized geometry.*

- TODO: ΔG^\ddagger from frequency analysis*
- calculate rates with reoptimized TS*
- calculate rates with VASP geometry TS*

Frequency Analysis

Apart from calculating adsorption energies, also normal modes with crystal were calculated with the functional B3LYP+D3 and PBE+D3, both with basis set 2 from Table 3.8. In addition to that, anharmonic corrections for both O-D bonds per system have been done. *TODO: mention how this is done? Appendix?*

In Table 3.17 the results for PBE and B3LYP for the (0001) surface are summarized. In

Table 3.17.: OD stretch vibration results with basis set 2 at the **(0001)** surface. Wavenumbers $\tilde{\nu}$ were calculated at the PBE and B3LYP level of theory with D3 corrections and also wavenumbers including anharmonic corrections $\tilde{\nu}_{\text{anh}}$. The presented VASP results were done by Dr. J. Wirth with a plane wave and PBE+D2.

| stretch | PBE | | B3LYP | | VASP PBE |
|-------------------------|------------------------------------|---|------------------------------------|---|------------------------------------|
| | $\tilde{\nu}$ [cm^{-1}] | $\tilde{\nu}_{\text{anh}}$ [cm^{-1}] | $\tilde{\nu}$ [cm^{-1}] | $\tilde{\nu}_{\text{anh}}$ [cm^{-1}] | $\tilde{\nu}$ [cm^{-1}] |
| mol: OD ₁ | 2657 | 2562 | 2747 | 2650 | 2664 |
| mol: OD ₂ | 2539 | 2490 | 2627 | 2584 | 2550 |
| 1-2: OD _{surf} | 2596 | 2521 | 2697 | 2623 | 2629 |
| 1-2: OD _{ads} | 2808 | 2727 | 2883 | 2805 | 2810 |
| 1-4: OD _{surf} | 2621 | 2531 | 2715 | 2631 | 2647 |
| 1-4: OD _{ads} | 2795 | 2788 | 2873 | 2788 | 2795 |

comparison with former VASP calculations, the PBE results with crystal do not deviate much. In contrast to that, B3LYP results are systematically higher in energy. For both

3.3. Improvement of Reaction Rates

functionals anharmonic corrections decrease the wavenumbers of the OD vibrations, so that the B3LYP+anharmonic corrections are again at the same level as uncorrected PBE with crystal and the results with VASP. In comparison with experimental SFG spectra [53], the overall agreement with VASP results was not convincing. The measured wavenumbers are: 2729, 2764, 2790 2900 and 2910 cm⁻¹. These could be assigned to the respective OD vibrations of different (dissociatively) adsorbed species. *Here the 1-4' species was not considered with Crystal.* Instead differences between the peaks with respect to the highest energy peak (OD_{ads} of 1-2 diss) were calculated which then showed very good agreement, see Table 3.18. Applying the same for the Crystal, even better results can be reached with B3LYP.

Table 3.18.: Vibrational frequency differences of the results presented in Table 3.17 with respect to the highest energy mode, OD_{ads} of 1-2 diss. All values are wavenumbers $\tilde{\nu}$ given in cm⁻¹.

| resonances | PBE | PBE+anh. | B3LYP | B3LYP+anh. | VASP | Exp. |
|----------------|-----|----------|-------|------------|------|------|
| 1-2ads-1-2surf | 212 | 206 | 186 | 182 | 181 | 191 |
| 1-2ads-1-4surf | 187 | 196 | 168 | 174 | 163 | 146 |
| 1-2ads-1-4ads | 13 | -61 | 10 | 17 | 15 | 10 |

Analogous to these calculations for the (0001) surface, the most stable adsorbed species at the (11̄20) surface were optimized with PBE+D3 and B3LYP+D3, respectively and the corresponding vibrational frequencies were evaluated. Corresponding results are shown in Table 3.19. Similar to the results for the (0001) surface cut, the PBE+D2/D3 results for both VASP

Table 3.19.: Stretch wavenumbers $\tilde{\nu}$ for both of the OD groups at the (11̄20) surface for the three most stable species. Frequencies were calculated at the B3LYP+D3 and PBE+D3 level of theory with basis set 2, Wavenumbers including anharmonic corrections $\tilde{\nu}_{anh}$ are also given. The VASP results were obtained with a plane wave basis and PBE+D2 corrections. The abbreviations stand for: iCa2 inter-CUSa||O- μ_2 , Cb2 CUSb||O- μ_2 and iCb2 inter-CUSb||O- μ_2 .

| stretch | PBE | | B3LYP | | VASP result |
|--------------------------|-----------------------------------|---|-----------------------------------|---|-----------------------------------|
| | $\tilde{\nu}$ [cm ⁻¹] | $\tilde{\nu}_{anh}$ [cm ⁻¹] | $\tilde{\nu}$ [cm ⁻¹] | $\tilde{\nu}_{anh}$ [cm ⁻¹] | $\tilde{\nu}$ [cm ⁻¹] |
| iCa2: OD _{surf} | 2682 | 2599 | 2773 | 2695 | 2694 |
| iCa2: OD _{ads} | 2728 | 2644 | 2811 | 2729 | 2731 |
| Cb2: OD _{surf} | 1658 | 1310 | 2019 | 1722 | 1711 |
| Cb2: OD _{ads} | 2769 | 2687 | 2843 | 2765 | 2785 |
| iCb2: OD _{surf} | 2657 | 2595 | 2778 | 2694 | 2689 |
| iCb2: OD _{ads} | 2688 | 2569 | 2777 | 2689 | 2692 |

and Crystal are in good agreement and B3LYP+D3 vibrations are higher in energy. Anhar-

3. Water on $\alpha\text{-Al}_2\text{O}_3(0001)$

monic corrections deliver lower energy modes, so that B3LYP including anharmonic corrections is again in the same range as the PBE results. In the experiments [60] three peaks are visible, that could be assigned to both OD groups of inter-CUSa||O- μ_2 and the OD_{ads} group of CUSb||O- μ_2 . The corresponding wavenumbers are 2762, 2812 and 2839 cm⁻¹. Compared to VASP results and crystal PBE+D3, these experimental wavenumbers are shifted by around 50-80 cm⁻¹ which is significantly better than for the (0001) surface. This good agreement could be caused by error cancellation. With anharmonic corrections, the agreement is even worse. Only the B3LYP+D3 results agree very well with deviations of one to eleven wavenumbers, which is an astonishingly well compliance. One has to mention, that here influence of the basis set is strong and larger basis sets were not feasible due to high computational costs. As it was shown before, anharmonic corrections shift the results to lower wavenumbers and decrease the overall agreement.

Summary

In this work great progress was made in understanding the (11 $\bar{2}$ 0) surface of α -Al₂O₃ in contact with water in the low coverage regime. This surface cut is the third most stable one under UHV conditions and has not been studied to a great extent yet. After optimization of the clean, defect free surface, the stability of different adsorbed species could be classified. One molecular minimum and several dissociated species could be detected, and starting from these reaction rates between minima were evaluated. In addition to reactivity, harmonic vibrational frequencies were determined for comparison with the findings of the experimental group from Fritz-Haber Institute in Berlin. Especially the vibrational frequencies could be assigned with very good agreement to experimental SFG spectra. *TODO: Also, lattice vibrations were studied in close collaboration with the experimental partners. As a novelty, they perform SFG spectra at very low frequencies to get deep into the lattice vibration region. Concerning this, a bigger slab model with greater expansion perpendicular to the surface was applied. The overall agreement with lower energy modes is typically worse than for high energy OD vibrations.*

The molecular beam scattering of water on (0001) surface was studied. This is the most stable surface cut under UHV conditions and was studied by many groups both theoretically and experimentally. In previous work by Hass the dissociation was studied by AIMD of molecularly adsorbed water, referring more to an equilibrium situation. The experimental method to obtaining this is pinhole dosing. In contrast to this earlier work, the dissociation process of heavy water when being shot from a molecular beam source was reproduced in this work by periodoc *ab initio* molecular dynamics simulations. This experimental method results in a non-equilibrium situation. This calculations with different surface and beam models let us understand better the results of the non-equilibrium situation. This gives, in contrast to a more equilibrium situation with pinhole dosing, an increase in the dissociation probability, which could be reproduced and also understood mechanistically by those calculations.

Several higher level methods were tested to improve reaction rates.*TODO: to be continued...*

Acknowledgment

I want to thank my doctoral father Prof. Dr. Saalfrank, for giving me the scientific opportunity to research on surface systems and all the valuable discussions and advices. Also I am deeply grateful to my supervisor Dr. Jonas Wirth who gave me support during my time starting as a Bachelor's student, during my Master's thesis and also through the beginning of my PhD. Thanks to PD Dr. Tillmann Klamroth for discussions about programming and millions of theoretical questions that arose during the work, Dr. Radosław Włodarczyk for his endless knowledge with VASP and programming in general, Giacomo Melani (soon to be Dr.) for his advice and his help, and also the discussions about our teaching duties in mathematics and the whole workgroup for all the valuable discussions and the help. Also for the great atmosphere, that was some times productive and some times also just relaxing and felt very comfortable, here especially Clemens Rietze, Robert Scholz, Gereon Floss, and Steven Lindner. Also I want to thank my second supervisor Beate Paulus for discussion and help beyond research topics. Great acknowledgement to my experimental cooperation partners from FHI, Yanhua Yue, Dr. Harald Kirsch and Dr. R. Kramer Campen for the great work and publications we did together. Thanks to Dr. Denis Usyat for all his patience and knowledge and valuable discussions about crystal/cryscor and his help.

I want to thank Dr. Jean Christophe Tremblay who brought me to theoretical chemistry by bringing my attention to this field of science. Christiane Wunderlich who was my school teacher in chemistry, without whom I would not have studied chemistry.

Appendix

TODO: Enumeration of the figures and tables, not starting with A..

Conversion of reciprocal coordinates a, b, c coordinates to x, y, z coordinates via matrix product:

$$(a'_1, b'_1, c'_1) \begin{pmatrix} a_1 & a_2 & a_3 \\ b_1 & b_2 & b_3 \\ c_1 & c_2 & c_3 \end{pmatrix} = (x_1, y_1, z_1)$$

with the matrix that is built up by the cell vectors a, b and c .

A. Experimental Techniques

In this work several experimental techniques were used from our collaborating group at the FHI in Berlin, that is why the basics of those methods shall be explained briefly.

A.1. Vibrational Sum Frequency Generation

This method is a surface specific vibrational spectroscopy. An UV/Vis and an IR Laser beam are overlapped spatially and in time to produce the so called sum frequency signal, see Figure A.1. There also the energy scheme is given: The system is excited with a pulse to a vibrationally excited state and with a UV/Vis pulse to a virtual state. The resulting SFG signal is a sum of both frequencies. For this, the polarization of the beam is important, it can be either s or

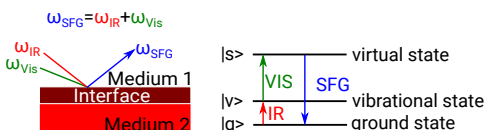


Figure AA.1: Scheme of the SFG Process, left side the spatially overlapping Laser beams are shown, on the right side the orbital representation with the excitation to a virtual orbital is given.

p polarized. The selection rules result in the surface specificity: The SFG only occurs if the vibration is IR and Raman active and additionally only in systems with inversion symmetry.

Appendix

This makes this method predestinated for analysis of surfaces, because neither the bulk nor the gas phase are inversion symmetric, however the interface (=surface, at least three atomic layers) is, so that the only signals come from this region. It is usually abbreviated SFG (sum frequency generation) but also named VSF(G) (vibrational sum frequency (generation)).

A.2. Thermal Desorption Spectroscopy

In thermal desorption spectroscopy (TDS, also temperature programmed desorption, TPD) the prepared sample is heated with a defined temperature program. Thus, adsorbates are removed from surface according their binding energies and detected as a function of temperature with any detection method required. The analysis sheds light on adsorption strength and probable reaction networks.

A.3. Molecular Beam Source vs. Pinhole Dosing

When doing the experiment the method of preparation seems crucial for the results, because these result in different surface situations. Our collaborators use the so called Molecular Beam Source but also widely used is pinhole dosing. Here the idea behind these methods and the main differences shall be explained.

Pinhole Dosing (PD): Water is brought with a high partial pressure onto the surface. Problem here: in the gas phase and on the walls of the measuring chamber can be amounts of water left that can influence the measurement. This leads to an equilibrium situation.

Molecular Beam Source (MBS): A medium, e.g. water is probed onto the surface at a very low pressure. Non-equilibrium situations are generated by the kinetic energy of the beam.

The difference between pinhole doser and MBS is that the former cannot heat the gas source to higher temperature but MBS can heat it to more than 800 K and this high energy is able to increase the dissociation of the gas source for example water or CH₄. MBS is used instead of pinhole doser to enhance the dissociated population on the sample surface.

A.4. Low-Energy Electron Diffraction

Spectroscopical method for determining crystal structures in crystalline materials by an electron beam with an energy in the range from 20 to 200 eV. Electrons are observed as a diffraction pattern on a fluorescent screen. The structure can be derived from the geometry of this pattern and the lattice geometry can be seen. Problem is the high energy of the beam that can lead to damage in the sample.

B. Symmetric Slab Frequency

In addition to the different sized slabs, a symmetric model of the surface with 15 layers was built. On both the top and the bottom, D₂O adsorbed dissociatively in inter-CUSa||O- μ_2 . A figure of the structure can be found in Figure B.2. In this model all atoms were allowed

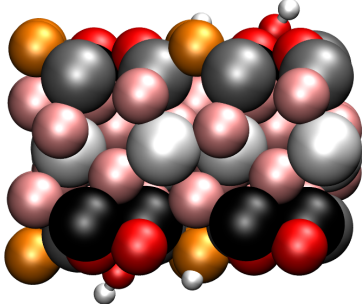


Figure AB.2: PBE+D2 optimized geometry of the 15 layer symmetric slab. The adsorbed species is the most stable inter-CUSa||O- μ_2 . Color code as explained above.

to relax. Henceforth, the normal mode analysis gives three imaginary frequencies (with very small energy, yet negative), that represent frustrated translation in a, b and c direction. The spectrum was calculated at the basis of dipole corrected normal modes and can be seen in Figure B.3. The high energy part (see Figure B.3(b)) shows that each of the two peaks comes

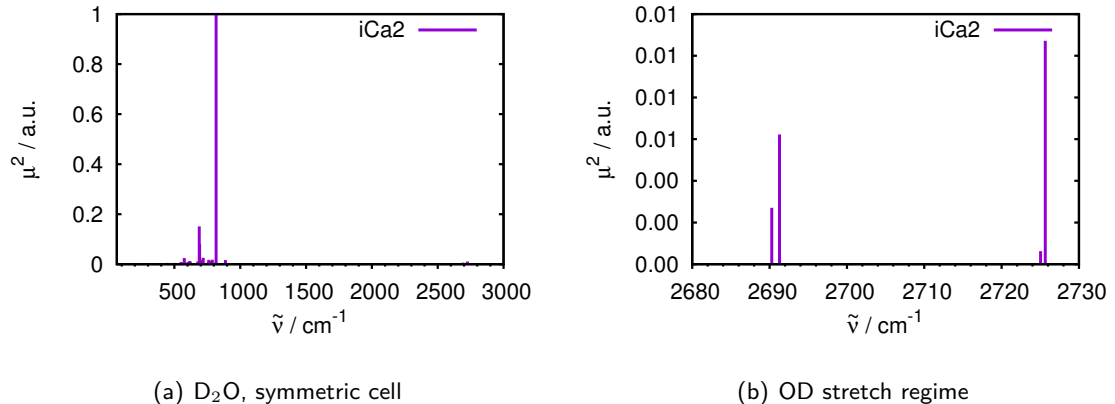


Figure AB.3: Stick spectrum of the 15 layer symmetric adsorption model normalized to the most intense peak. (a) shows the total range of the dipole corrected spectrum and (b) gives a closer look at the OD range, featuring two doublets.

as a doublet due to the imperfect degeneracy of “both sides” of the slab, which has numerical reasons. These doublets lie at 2690 and 2725 cm⁻¹, which is slightly lower than the asymmetric model (only one adsorbate on the top) results for all applied slab sizes. For example, for the

Appendix

15 layer system the peaks come up at 2695 and 2728 cm^{-1} . In the lattice region, these shifts are stronger, but nevertheless small in general. The most intense peak is shifted from 801 to 816 (15 layer symmetric slab) but this shift is rather small. The overall agreement is very good so that it can be concluded, that although the computational costs are increased the symmetrically adsorption ansatz does not give any new insights to the system.

C. Distance Test for Water Molecule

As explained in the main text, Subsection 3.2.1, the distance of the water molecule and the surface was set to 4 \AA . Further test calculations were done to prove that this distance is sufficient. In Figure C.4 it could be shown, that there is only a difference in the impact time, caused by the longer distance to the surface but no difference in the outcomes of the trajectories, since all other parameters stay the same.

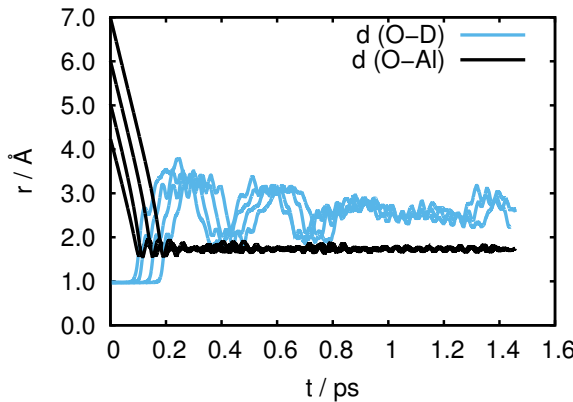


Figure AC.4: Trajectories for D_2O approaching the surface for initial molecule-surface distances of 4 , 5 , 6 and 7 \AA from left to right. Black lines depict the O-Al distance whereas the blue lines show the O-D distance of the dissociating deuterium, respectively. The impact time is, of course, different. Parameters for these calculations were: impact point $[0.35, 0.5]$, orientation $[0, 0, 0]$ and kinetic energy $E_{\text{kin}} = 0.7\text{ eV}$. All four trajectories give 1-2 dissociation.

D. Reaction Probabilities

In this section, the probabilities P for different findings of the AIMD molecular beam scattering simulations shall be given in detail. Therefore the following abbreviations are used:

D. Reaction Probabilities

P_{mol} =molecular adsorption, $P_{\text{diss}}(1\text{-}2)$ = 1-2 dissociation, $P_{\text{diss}}(1\text{-}4)$ = 1-4 dissociation, $P_{\text{diss}}(1\text{-}4')$ = 1-4' dissociation, P_{phys} = physisorption (of molecular D₂O), and P_{refl} =reflection. In case of two numbers in one cell, the first one refers to direct dissociation, and the second gives the probability for indirect dissociation, for example after initial molecular adsorption.

Due to the rounding procedure, the sum of the probabilities can be slightly different from 1. If no probabilities for an outcome are listed, the process did not occur. One has to have in mind that all results are obtained for only a limited amount of trajectories whose number is given, respectively.

D.1. Microcanonical AIMD at a Clean Surface at $T = 0$

The probabilities for the microcanonical (NVE) results for a clean surface with a single, rigid D₂O molecule and a $T = 0$ K surface for different initial kinetic energies E_{kin} from 0.5 to 0.9 eV are shown in Table D.1

Table AD.1: Results for the NVE, $T = 0$ K trajectories of a single D₂O molecule approaching the clean surface. Average was calculated over all 48 combinations of eight rotational orientations and six lateral impact points for each initial kinetic energy.

| E_{kin} [eV] | P_{mol} | $P_{\text{diss}}(1\text{-}2)$ | P_{refl} |
|-----------------------|------------------|-------------------------------|-------------------|
| 0.5 | 0.56 | 0.17 + 0.08 | 0.19 |
| 0.6 | 0.58 | 0.17 + 0.06 | 0.19 |
| 0.7 | 0.58 | 0.17 + 0.06 | 0.19 |
| 0.8 | 0.54 | 0.15 + 0.12 | 0.19 |
| 0.9 | 0.50 | 0.19 + 0.04 | 0.27 |

D.2. Refined Surface Models: Effects of Precovrage

An improvement to the clean surface model is the so called precovered surface, with one D₂O per 2×2 supercell. This preadsorbed water was either adsorbed molecularly or dissociatively (1-2 or 1-4). To this prepared surface a single D₂O molecule was brought with an initial kinetic energy of 0.7 eV with $T = 0$ K (NVE ensemble). The impact site was either in the same 1×1 subcell or in a neighboring part of the subcell. The obtained probabilities in Table D.2 were averaged over 89 trajectories. More details can be found in the table caption and footnotes.

In addition to the NVE trajectories at $T = 0$ K, analog NVT calculations were done for a thermalized and preadsorbed surface. The surface including the preadsorbed species was equilibrated for 1 ps at $T = 300$ K starting from the minimum structure of the adsorbed

Appendix

Table AD.2: NVE reaction probabilities for D₂O approaching the preadsorbed surface with an initial kinetic energy of 0.7 eV. The term "same CUS" refers to a D₂O hitting the 1 × 1 subcell where the water is preadsorbed and "neighbor CUS" refers to a situation, where the incoming molecule hits another subcell. The preadsorbed water was considered to be either adsorbed molecularly ("preads. mol"), 1-2 dissociated ("preads. 1-2") or 1-4 dissociated ("preads 1-4").

| | preads. | P_{mol} | $P_{\text{diss}}(1-2)$ | $P_{\text{diss}}(1-4)$ | P_{phys} | P_{refl} |
|--------------|------------------|------------------|------------------------|------------------------|-------------------|-------------------|
| same CUS | mol ¹ | 0.57 | 0.00+0.04 | 0.04+0.00 | 0.32 | 0.04 |
| | 1-2 ² | 0.77 | 0.08+0.00 | 0.00 | 0.00 | 0.15 |
| | 1-4 ³ | 0.42 | 0.00 | 0.00 | 0.33 | 0.25 |
| neighbor CUS | mol ⁴ | 0.36 | 0.18+0.05 | 0.23 | 0.18 | 0.00 |
| | 1-2 ⁵ | 0.57 | 0.29 | 0.00 | 0.00 | 0.14 |
| | 1-4 ⁶ | 0.71 | 0.14 | 0.00 | 0.00 | 0.14 |

¹ 28 trajectories, for [0.35,0.5], [0.5,0.35] and [0.35,0.45] all eight orientations and for the remaining three impact points only selected ones: [0.33,0.33]: [0,90,0] and [90,90,90]; [0.5,0.5]: [90,90,0] and [0.4,0.5]: [0,90,0]

² 13 trajectories, for [0.35,0.45] all eight orientations, [0.33,0.33]: [0,90,0] and [90,90,90]; [0.5,0.5]: [90,90,0]; [0.35,0.5]: [0,0,0]; [0.4,0.5]: [0,90,0]

³ 12 trajectories, for [0.35,0.45] all orientations were calculated, but [0,90,90] failed, for [0.33,0.33]: [0,90,0] and [90,90,90]; [0.5,0.5]: [90,90,0]; [0.35,0.5]: [0,0,0]; [0.4,0.5]: [0,90,0]

⁴ 22 trajectories, for [0.35,1.0] and [0.5,0.85] all orientations, [0.33,0.83]: [0,90,0] and [90,90,90]; [0.5,1.0]: [90,90,0]; [0.35,0.95]: [0,0,0] and [90,90,0]; [0.4,1.0]: [0,90,0]

⁵ seven trajectories, for [0.33,0.83]: [0,90,0] and [90,90,90]; [0.5,1.0]: [90,90,0]; [0.35,1.0]: [0,0,0]; [0.35,0.95]: [0,0,0] and [90,90,0]; [0.4,1.0]: [0,90,0]

⁶ seven trajectories, for [0.33,0.83]: [0,90,0] and [90,90,90]; [0.5,1.0]: [90,90,0]; [0.35,1.0]: [0,0,0]; [0.35,0.95]: [0,0,0] and [90,90,0]; [0.4,1.0]: [0,90,0]

species. To this surface, water with a kinetic energy of 0.7 eV was shot in 140 trajectories. More details are given in the table footnotes.

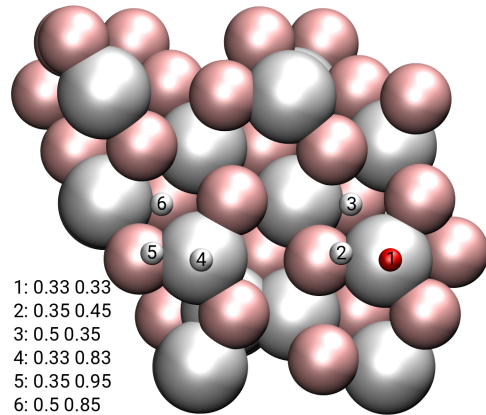


Figure AD.5: Distinctive lateral impact points for the trajectories from Table D.3 at the "same" and the "neighboring" CUS.

D. Reaction Probabilities

Table AD.3: Probabilities for the NVT (canonical) case at 300 K. Three impact points were considered for the "same CUS": [0.33,0.33], [0.35,0.45] and [0.5,0.35] and four for the "neighbouring CUS": [0.33,0.83], [0.35,0.95] and [0.5,0.85]. These are shown for clarification in Figure D.5. If not mentioned otherwise, all eight rotational orientations were considered.

| | preads. | P_{mol} | $P_{\text{diss}}(1-2)$ | $P_{\text{diss}}(1-4)$ | P_{phys} | P_{refl} |
|--------------|------------------|------------------|------------------------|------------------------|-------------------|-------------------|
| same CUS | mol | 0.08+0.17 | 0.00+0.04 | 0.00 | 0.63 | 0.08 |
| | 1-2 | 0.00+0.83 | 0.00 | 0.00 | 0.13 | 0.04 |
| | 1-4 ¹ | 0.05+0.40 | 0.00+0.05 | 0.00 | 0.40 | 0.10 |
| neighbor CUS | mol | 0.63 | 0.17+0.17 | 0.04 | 0.00 | 0.00 |
| | 1-2 | 0.71 | 0.21 | 0.08 | 0.00 | 0.00 |
| | 1-4 | 0.92 | 0.08 | 0.00 | 0.00 | 0.00 |

¹ for [0.33,0.33] the orientations [0,0,0], [90,90,0] and [90,90,90] and for impact points [0.5,0.35] the orientation [90,0,90] the trajectories failed and were not analyzed

D.3. Refined Beam Models: Clustering and Preexcitation

Apart from a refined surface model, the beam model was enhanced, too. In Table D.4 probabilities for a $(\text{D}_2\text{O})_4$ cluster are shown. This cluster was shot at the surface with an initial kinetic energy of 0.9 eV towards a cold ($T = 0\text{K}$), clean surface in an NVE (microcanonical) MD ansatz. In total, ten trajectories for four different impact points and three different orientations were done (for one impact point, only one orientation was considered).

Table AD.4: Reaction probabilities for a $(\text{D}_2\text{O})_4$ cluster approaching a clean surface with $E_{\text{kin}} = 0.9$ eV of microcanonical (NVE, $T = 0$) trajectories.

| P_{mol} | $P_{\text{diss}}(1-2)$ | $P_{\text{diss}}(1-4)$ | $P_{\text{diss}}(1-4')$ | P_{phys} | P_{refl} |
|------------------|------------------------|------------------------|-------------------------|-------------------|-------------------|
| 0.25 | 0.05+0.10 | 0.03+0.18 | 0.00+0.05 | 0.18 | 0.18 |

In addition to considering a water cluster, microcanonical MD of a single D_2O molecule that was vibrationally and/or rotationally excited were conducted. In addition to the linear momentum towards the surface, the molecule was excited vibrationally (symmetric, asymmetric stretch and bending) or rotationally (around the three axes) and four rotations coupled with vibrational modes. This was done in ten trajectories for only one set of parameters ([0.35,0.5],[0,0,0]) for a kinetic energy of 0.7 eV. Probabilities are given in Table D.5

D.4. $(\text{D}_2\text{O})_2$ Cluster

Also one type of $(\text{D}_2\text{O})_2$ cluster was tested (see Figure D.6). The structure is not the minimum structure but another dimolecular water cluster. Even in the case of the $(\text{D}_2\text{O})_2$ cluster,

Appendix

Table AD.5: Reaction probabilities an excited D₂O. Microcanonical (NVE, $T = 0$) trajectories of vibrationally and/or rotationally excited D₂O approaching a clean surface were done with $E_{\text{kin}} = 0.7 \text{ eV}$.

| P_{mol} | $P_{\text{diss}}(1\text{-}2)$ | $P_{\text{diss}}(1\text{-}4)$ | $P_{\text{diss}}(1\text{-}4')$ | P_{phys} | P_{refl} |
|------------------|-------------------------------|-------------------------------|--------------------------------|-------------------|-------------------|
| 0.20 | 0.30+0.20 | 0.00 | 0.00+0.10 | 0.00 | 0.20 |

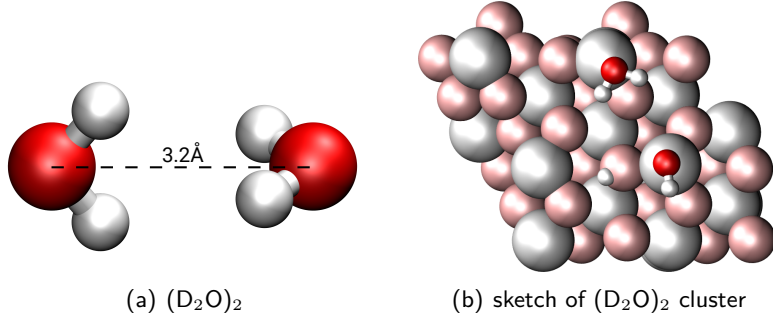


Figure AD.6: (a) Structure of the optimized (D₂O)₂ cluster. (b) shows an example situation at the last step (after 1.2 ps) for 2 water molecules for the initial parameters $[a_0, b_0] = [0.35, 0.45]$, $[\alpha, \beta, \gamma] = [90, 0, 90]$.

strong interaction between the molecules can be observed, although not as much as for the tetramer. Also “only” molecular adsorption, 1-2 and 1-4 dissociation occur within the sampling. Interestingly, there is no case, where both molecules react in the same way. For most dissociated trajectories there is only direct dissociation at the moment of the impact, with the only indirect one dissociating 0.3 ps later. Apart from that, no further dissociation and diffusion reactions were observed.

Table AD.6: Reaction probabilities for microcanonical (NVE, $T = 0$) trajectories of the (D₂O)₂ cluster with a clean surface hitting with an initial kinetic energy $E_{\text{kin}} = 0.7 \text{ eV}$.

| P_{mol} | $P_{\text{diss}}(1\text{-}2)$ | $P_{\text{diss}}(1\text{-}4)$ | P_{refl} |
|------------------|-------------------------------|-------------------------------|-------------------|
| 0.4 | 0.15+0.05 | 0.05 | 0.35 |

D. Reaction Probabilities

Publications

This Work:

- (1) Heiden, S.; Yue, Y.; Kirsch, H.; Wirth, J.; Saalfrank, P.; Campen, R. K.: »Water Dissociative Adsorption on $\alpha\text{-Al}_2\text{O}_3(11\bar{2}0)$ Is Controlled by Surface Site Undercoordination, Density, and Topology«, *The Journal of Physical Chemistry C* **2018**, 122 (12), 6573-6584.
- (2) Heiden, S.; Wirth, J.; Campen, R. K.; Saalfrank, P.: »Water Molecular Beam Scattering at $\alpha\text{-Al}_2\text{O}_3(0001)$: An *Ab Initio* Molecular Dynamics Study«, *The Journal of Physical Chemistry C* **2018**, 122 (27), 15494-15504.

References

- [1] Ago, H.; Nakamura, K.; Ikeda, K.; Uehara, N.; Ishigami, N.; Tsuji, M. Aligned Growth of Isolated Single-Walled Carbon Nanotubes Programmed by Atomic Arrangement of Substrate Surface, *Chem. Phys. Lett.* **2005**, *408*, 433-438.
- [2] Cagnello, M.; Delgado, J.; Hernández, J.; Bakmutsky, K. .; Montini, T.; Gámez, J. C.; Gorte, R.; Fornasiero, P. Exceptional Activity for Methane Combustion over Modular Pd@CeO₂ Subunits on Functionalized Al₂O₃, *Science* **2012**, *337*, 713-717.
- [3] Knözinger, H.; Ratnasamy, P. Catalytic Aluminas: Surface Models and Characterization of Surface Sites, *Catal. Rev.* **1978**, *17*, 31-70.
- [4] Elam, J. W.; Nelson, C. E.; Cameron, M. A.; Tolbert, M. A.; George, S. M. Adsorption of H₂O on a Single-Crystal α -Al₂O₃(0001) Surface, *J. Phys. Chem. B* **1998**, *102*, 7008-7015.
- [5] Potter, A. E. J. Environmental Effects of the Space Shuttle, *Environ. Sci.* **1978**, *21*, 15-21.
- [6] Cofer, W. R.; Lala, G. G.; Wightman, J. P. Analysis of Mid-Tropospheric Space Shuttle Exhausted Aluminum Oxide Particles, *Atmos. Environ.* **1987**, *21*, 1187-1196.
- [7] Jones, A. E.; Bekki, S.; Pyle, J. A. On the Atmospheric Impact of Launching the Ariane 5 Rocket, *J. Geophys. Res.: Atm.* **1995**, *100*, 16651-16660.
- [8] Jackman, C. H.; Fleming, E. L.; Chandra, S.; Considine, D. B.; Rosenfield, J. E. Past, Present, and Future Modeled Ozone Trends with Comparisons to Observed Trends, *J. Geophys. Res.: Atm.* **1996**, *101*, 753-28.
- [9] Riedel, E.; Janiak, C. *Anorganische Chemie*; Walter de Gruyter: Berlin, 7 ed.; 2007.
- [10] Breuer, H. *dtv-Atlas Chemie, Band 1, Allgemeine und anorganische Chemie*; dtv: München, 9 ed.; 2000.
- [11] Trail, D.; Watson, E. B.; Tailby, N. D. The Oxidation State of Hadean Magmas and Implications for Early Earth's Atmosphere, *Nature* **2011**, *480*, 79-82.
- [12] Frei, R.; Gaucher, C.; Poulton, S. W.; Canfield, D. E. Fluctuations in Precambrian Atmospheric Oxygenation Recorded by Chromium Isotopes, *Nature* **2009**, *461*, 250–253.
- [13] Buick, R. When did Oxygenic Photosynthesis Evolve?, *Philos. Trans. R. Soc. Lond. B: Biol. Sci.* **2008**, *363*, 2731–2743.

- [14] Olson, J. M. Photosynthesis in the Archean Era, *Photosynth. Res.* **2006**, *88*, 109–117.
- [15] Kirschvink, J. L.; Kopp, R. E. Palaeoproterozoic Ice Houses and the Evolution of Oxygen-mediating Enzymes: The Case for a Late Origin of Phtosystem II, *Philos. Trans. R. Soc. Lond. B: Biol. Sci.* **2008**, *363*, 2755-2765.
- [16] Jensen, F. *Introduction to Computational Chemistry*; Wiley: 2 ed.; 2007.
- [17] Born, M.; Oppenheimer, R. Zur Quantentheorie der Molekeln, *Annalen der Physik* **1927**, *389*, 457–484.
- [18] Tuma, C.; Sauer, J. A Hybrid MP2/Planewave-DFT Scheme for Large Chemical Systems: Proton Jumps in Zeolites, *Chem. Phys. Lett.* **2004**, *387*, 388-394.
- [19] Monkhorst, H. J.; Pack, J. D. Special Points for Brillouin-Zone Integrations, *Phys. Rev. B* **1976**, *13*, 5177.
- [20] Holleman, A.; Wiberg, E.; Wiberg, N. *Lehrbuch der anorganischen Chemie*; Walter de Gruyter: 2007.
- [21] Tosoni, S.; Tuma, C.; Sauer, J.; Civalleri, B.; Ugliengo, P. A Comparison between Plane Wave and Gaussian-type Orbital Basis Sets for Hydrogen Bonded Systems: Formic Acid as a Test Case, *J. Chem. Phys* **2007**, *127*, 154102-1-11.
- [22] Blöchl, P. E. Projector Augmented-Wave Method, *Phys. Rev. B* **1994**, *50*, 17953.
- [23] Kresse, G.; Joubert, D. From Ultrasoft Pseudopotentials to the Projector Augmented-Wave Method, *Phys. Rev. B: Condens. Matter Mater. Phys.* **1999**, *59*, 1758-1775.
- [24] Boys, S.; Bernardi, F. The Calculation of Small Molecular Interactions by the Differences of Separate Total Energies. Some Procedures with Reduced Errors, *Mol. Phys.* **1970**, *19*, 553-566.
- [25] Marx, D.; Hutter, J. *Ab Initio Molecular Dynamics: Basic Theory and Advanced Methods*; Cambridge University Press: 2012.
- [26] Verlet, L. Computer "Experiments" on Classical Fluids. I. Thermodynamical Properties of Lennard-Jones Molecules, *Phys. Rev.* **1967**, *159*, 98–103.
- [27] Nosé, S. A Unified Formulation of the Constant Temperature Molecular Dynamics Methods, *J. Chem. Phys.* **1984**, 511-519.
- [28] Nosé, S. A Molecular Dynamics Method for Simulations in the Canonical Ensemble, *Mol. Phys.* **1984**, 255-68.
- [29] Hoover, W. G. Canonical Dynamics: Equilibrium Phase-Space Distributions, *Phys. Rev. A: At., Mol., Opt. Phys.* **1985**, 1695-97.
- [30] Karhánek, D.; Bučko, T.; Hafner, J. A Density-Functional Study of the Adsorption of Methane-Thiol on the (111) Surfaces of the Ni-Group Metals: II. Vibrational Spectroscopy, *J. Phys.: Condens. Matter* **2010**, *22*, 265006-1-9.

- [31] Born, M.; Huang, K. *Dynamical Theory of Crystal Lattices*; Oxford University Press: 1954.
- [32] Grillo, F.; Garrido Torres, J. A.; Treanor, M.-J.; Larrea, C. R.; Götze, J. P.; Lacovig, P.; Fruchtl, H. A.; Schaub, R.; Richardson, N. V. Two-Dimensional Self-Assembly of Benzotriazole on an Inert Substrate, *Nanoscale* **2016**, *8*, 9167-9177.
- [33] Baroni, S.; Giannozzi, P.; Testa, A. Green's-Function Approach to Linear Response in Solids, *Phys. Rev. Lett.* **1987**, *58*, 1861–1864.
- [34] Giannozzi, P.; Gironcoli, S.; Pavone, P.; Baroni, S. *Ab initio* Calculation of Phonon Dispersion in Semiconductors, *Phys. Rev. B* **1991**, *43*, 7231–7242.
- [35] Brüesch, P. *Phonons: Theory and Experiments II*; Springer: 1986.
- [36] Baroni, S.; de Gironcoli, S.; Corso, A. D.; Giannozzi, P. Phonons and Related Crystal Properties from Density-Functional Perturbation Theory, *Rev. Mod. Phys.* **2001**, *75*, 515–562.
- [37] Thomas, M.; Brehm, M.; Fligg, R.; Vöhringer, P.; Kirchner, B. Computing Vibrational Spectra from *Ab Initio* Molecular Dynamics, *Phys. Chem. Chem. Phys.* **2013**, *15*, 6608.
- [38] Horníček, J.; Kaprálová, P.; Bouř, P. Simulations of Vibrational Spectra from Classical Trajectories: Calibrations with *Ab Initio* Force Fields, *J. Chem. Phys.* **2007**, *127*, 084502-1-9.
- [39] Hudecová, J.; Hopmann, K.; Bouř, P. Correction of Vibrational Broadening in Molecular Dynamics Clusters with the Normal Mode Optimization Method, *J. Phys. Chem. B* **2012**, *116*, 336–342.
- [40] Zhao, Y.; González-García, N.; Truhlar, D. G. Benchmark Database of Barrier Heights for Heavy Atom Transfer, Nucleophilic Substitution, Association, and Unimolecular Reactions and Its Use to Test Theoretical Methods, *J. Phys. Chem. A* **2005**, *109*, 2012-2018.
- [41] Becke, A. D. Density-functional Thermochemistry. III. The Role of Exact Exchange, *J. Chem. Phys.* **1993**, *98*, 5648–5652.
- [42] Møller, C.; Plesset, M. S. Note on an Approximation Treatment for Many-Electron Systems, *Phys. Rev.* **1934**, *46*, 618-622.
- [43] Usyat, D.; Maschio, L.; Schütz, M. Periodic Local MP2 Method Employing Orbital Specific Virticals, *J. Chem. Phys.* **2015**, *143*, 102805-1-12.
- [44] Usyat, D.; Maschio, L.; Schütz, M. Periodic Local Møller-Plesset Perturbation Theory of Second Order for Solids, *Handbook of Solid State Chemistry* **2017**, *5*, 59-86.
- [45] Dovesi, R.; Orlando, R.; Erba, A.; Zicovich-Wilson, C. M.; Civalleri, B.; Casassa, S.; et. al., CRYSTAL14: A Program for the Ab Initio Investigation of Crystalline Solids, *Int. J. Quant. Chem.* **2014**, *114*, 1287-1317.
- [46] Pisani, C.; Schütz, M.; Casassa, S.; Usyat, D.; Maschio, L.; Lorenz, M.; Erba, A. Cryscor: A Program for the Post-Hartree-Fock Treatment of Periodic Systems, *Phys. Chem. Chem. Phys.* **2012**, *14*, 7615-7628.

- [47] Kresse, G.; Hafner, J. *Ab initio* Molecular Dynamics for Liquid Metals, *Phys. Rev. B: Condens Matter Mater. Phys.* **1993**, *47*, 558-561.
- [48] Kresse, G.; Hafner, J. *Ab initio* Molecular-Dynamics Simulation of the Liquid-Metal - Amorphous-Semiconductor Transition in Germanium, *Phys. Rev. B: Condens. Matter Mater. Phys.* **1994**, *49*, 14251-69.
- [49] Kresse, G.; Furthmüller, J. Efficiency of Ab-Initio Total Energy Calculations for Metals and Semiconductors using a Plane-Wave Basis Set, *Comput. Mat. Sci.* **1996**, *6*, 15-50.
- [50] Kresse, G.; Furthmüller, J. Efficient Iterative Schemes for Ab Initio Total-Energy Calculations using a Plane-Wave Basis Set, *Phys. Rev. B: Condens. Matter Mater. Phys.* **1996**, *54*, 11169-86.
- [51] Kresse, G.; Joubert, D. From Ultrasoft Pseudopotentials to the Projector Augmented-Wave Method, *Phys. Rev. B: Condens. Matter Mater. Phys.* **1999**, *59*, 1758-1775.
- [52] Wirth, J.; Saalfrank, P. The Chemistry of Water on α -Alumina: Kinetics and Nuclear Quantum Effects from First Principles, *J. Phys. Chem. C* **2012**, *116*, 26829-26840.
- [53] Kirsch, H.; Wirth, J.; Tong, Y.; Wolf, M.; Saalfrank, P.; Campen, R. K. Experimental Characterization of Unimolecular Water Dissociative Adsorption on α -Alumina, *J. Phys. Chem. C* **2014**, *118*, 13623-13630.
- [54] Tong, Y.; Wirth, J.; Kirsch, H.; Wolf, M.; Saalfrank, P.; Campen, R. K. Optically Probing Al-O and O-H Vibrations to Characterize Water Adsorption and Surface Reconstruction on α -Alumina: An Experimental and Theoretical Study, *J. Chem. Phys.* **2015**, *142*, 054704.
- [55] Wirth, J.; Kirsch, H.; Włoszczyk, S.; Tong, Y.; Saalfrank, P.; Campen, R. K. Characterization of Water Dissociation on α -Al₂O₃(1102): Theory and Experiment, *Phys. Chem. Chem. Phys.* **2016**, *18*, 14822-14832.
- [56] Passerini, L. Solid Solutions, Isomorphism and Symmorphism of the Oxide of Trivalent Metals: The Systems Al₂O₃-Cr₂O₃, Al₂O₃-Fe₂O₃, Cr₂O₃-Fe₂O₃, *Gazz. Chim. Ital.* **1930**, *60*, 544.
- [57] Wyckoff, R. W. G. *The Structure of Crystals*; American Chemical Society: 1931.
- [58] Stair, P. C. The Concept of Lewis Acids and Bases Applied to Surfaces, *J. Am. Chem. Soc.* **1982**, *104*, 4044-4052.
- [59] Kurita, T.; Uchida, K.; Oshiyama, A. Atomic and Electronic Structures of α -Al₂O₃ Surfaces, *Phys. Rev. B* **2010**, *82*, 155319.
- [60] Heiden, S.; Yue, Y.; Kirsch, H.; Wirth, J.; Saalfrank, P.; Campen, R. K. Water Dissociative Adsorption on α -Al₂O₃(1120) Is Controlled by Surface Site Undercoordination, Density, and Topology, *J. Phys. Chem. C* **2018**, *122*, 6573-6584.
- [61] Wirth, J. *Chemische Reaktionen in Substrat-Adsorbat-Systemen: Eine kinetische Perspektive*, Thesis, Universität Potsdam, 2014.

- [62] Hass, K. C.; Schneider, W. F.; Curioni, A.; Andreoni, W. The Chemistry of Water on Alumina Surfaces: Reaction Dynamics from First Principles, *Science* **1998**, *282*, 265–268.
- [63] Hass, K. C.; Schneider, W. F.; Curioni, A.; Andreoni, W. First-Principles Molecular Dynamics Simulations of H₂O on α -Al₂O₃(0001), *J. Phys. Chem. B* **2000**, *104*, 5527–5540.
- [64] Heiden, S.; Wirth, J.; Campen, R. K.; Saalfrank, P. Water Molecular Beam Scattering at α -Al₂O₃(0001): An *Ab Initio* Molecular Dynamics Study, *J. Phys. Chem. C* **2018**, *122*, 15494–15504.
- [65] Wales, D. J.; Walsh, T. R. Theoretical Study of the Water Tetramer, *J. Chem. Phys.* **1997**, *106*, 7193–7207.

Erklärung

Hiermit versichere ich, dass die vorliegende Arbeit an keiner anderen Hochschule eingereicht sowie selbständig und ausschließlich mit den angegebenen Mitteln angefertigt worden ist.

Potsdam, **TODO: xx** 2018